Cosmogenic ^{10}Be and stable ^{9}Be at the land-ocean interface

Dissertation

zur Erlangung des Grades eines
Doktors der Naturwissenschaften (doctor rerum naturalium)

am Fachbereich Geowissenschaften
der Freien Universität Berlin

vorgelegt von
Chenyu Wang
Berlin 2023

Erstgutachter: Prof. Dr. Friedhelm von Blanckenburg
Zweitgutachter: Prof. Dr. Martin Frank

Tag der Disputation: 11.01.2024

Eidesstattliche Erklärung

Hiermit erkläre ich, dass ich die vorliegende Dissertation selbstständig und ohne unzulässige Hilfe verfasst habe. Bei der Verfassung dieser Dissertation wurden keine anderen als die im Text und Literaturverzeichnis aufgeführten Hilfsmittel und Quellen verwendet. Beiträge von Koautoren zu publizierten oder zur Publikation vorbereiteten Manuskripten sind im Vorwort ("Preface") dieser Arbeit dargelegt. Ich versichere, dass die vorgelegte elektronische mit der schriftlichen Version der Dissertation übereinstimmt. Ein Promotionsverfahren zu einem früheren Zeitpunkt an einer anderen Hochschule oder einem anderen Fachbereich wurde nicht beantragt.

Berlin, 09.11.2023

_____

Chenyu Wang

Acknowledgements

The past four years have been a remarkable chapter in my life, and I am sincerely thankful to everyone who has been a part of this journey.

First and foremost, I would like to express my deepest and heartfelt gratitude to my co-supervisor and supervisor: Dr. Hella Wittmann and Prof. Dr. Friedhelm von Blanckenburg. Thanks for providing me with this opportunity to become a part of Section 3.3, and guiding me into the fascinating world of beryllium. Friedhelm, I will never forget that afternoon we sat together for hours trying to set up a few mass balance equations. Your enthusiasm and dedication to research has always inspired me. Hella, there is no word can express my gratitude to you. You are always being there to provide me with any support I need, from the smallest detail of an experiment to the writing of a manuscript. Without you, this doctoral thesis wouldn't have been completed so smoothly. I have always felt so fortunate to be a student of both of you.

I also extend my sincere appreciation to all of my co-authors: Daniel A. Frick, Martin Frank, Ergang Lian, Shouye Yang, Jeffrey Paulo Perez, Ed Hathorne and Florian Scholz. Your collective efforts in sample collection, insightful discussions, and valuable feedback greatly contributed to the quality of this thesis. A special thanks to Daniel, who introduced me to the most important instrument of my doctoral career, the HR-ICP-MS, and always patiently answered my questions.

Furthermore, I would also like to express my great gratitude to all other colleagues (including our former colleagues) in Section 3.3 Earth Surface Geochemistry at GFZ. I am so proud to have worked alongside such a creative, brilliant group of people. Many thanks to Cathrin Schulz for the assistance in the Cosmo Lab, which allowed my experiment to proceed smoothly. Thanks to Coni Dettlaff for always being so kind and helpful with all the administrative stuff. I would also like to thank Patrick Frings, who helped me polish my English writing, and Kai Deng, Laura Vivien Krone, Nestor Gaviria Lugo, Simon Ring, and Ruchi for their friendship, discussions, encouragement, and continuous support. Special thanks also go to Yan, my old friend, former colleague and former roommate, thanks for your company both physically and mentally. I really cherish the memories of working together, sharing ideas, drinking beers on ‘Bier nach Vier’ with all of you.

I also want to thank the China Scholarship Council for providing financial support for my study and life in Germany.

Last but certainly not least, I have to express my deepest appreciation to my family and my boyfriend for their unwavering support, love, and encouragement. Thank you for being my rock and my inspiration.

Summary

The land-ocean interface is the most important source or sink for many trace elements in the ocean. Investigating the geochemical behaviour of beryllium (Be) isotopes, encompassing the cosmogenic radionuclide ^{10}Be and the stable nuclide ^{9}Be, and the transfer pathways of Be at this interface is imperative. First, knowing the mechanisms of Be transfer is a prerequisite for the application of the oceanic ^{10}Be/^{9}Be ratio as a sensitive proxy for past continental weathering. Second, understanding the transfer of Be will contribute to our current knowledge of marine biogeochemical cycles of particle-reactive trace metals in general. Third, it helps to expand the potential applications of the ^{10}Be/^{9}Be ratio in coastal marine environments. However, research in this field, particularly on the distribution of ^{10}Be/^{9}Be in coastal seawater, is still lacking due to the analytical challenges in accurately determining ultra-low concentrations of ^{9}Be (at the level of pg/g) and ^{10}Be (at the level of single atoms) in seawater.

In this thesis, I propose a new, time-efficient procedure for the simultaneous preconcentration of the exceedingly low levels of ^{9}Be and ^{10}Be from (coastal) seawater based on the iron co-precipitation method. This new procedure contributes towards more time-efficient handling of samples, less risk of sample cross-contamination, and a more accurate ^{10}Be/^{9}Be ratio. I also evaluated the iron co-precipitation method with respect to: i) the impact of major matrix elements on the accuracy of obtained Be concentrations, ii) its extraction efficiency for pg/g-levels Be in the presence and absence of organic matter, and iii) the comparison with existing preconcentration methods. For the determination of ^{9}Be and ^{10}Be in open ocean seawater samples, a precision on the ^{10}Be/^{9}Be ratio of <5% can be attained using less than 3 L of seawater, whereas previously more than 20 L were used to obtain this precision. Even for coastal seawater with extremely low ^{10}Be concentration of only 100 atoms/g, a maximum seawater amount of 10 L is sufficient.

I applied this new procedure to measure dissolved ^{9}Be and ^{10}Be along the entire salinity gradient in two of the largest estuaries on Earth: The Changjiang and the Amazon River estuary. In addition, I determined the ^{10}Be and ^{9}Be concentrations in different chemically extractable fractions of the corresponding suspended and bottom sediments. The main objectives were i) to investigate terrigenous ^{9}Be pathways into the ocean under a variety of hydro-chemical estuarine conditions; and ii) to fill the current knowledge gap of the distribution of ^{10}Be/^{9}Be at the land-ocean interface and explore its applications in reconstructing past continental denudation rates of the adjacent river catchments.

In both estuaries, dissolved ^{9}Be and ^{10}Be display similar, non-conservative behaviour during estuarine mixing. The removal and release of dissolved ^{9}Be in the Changjiang Estuary and its relationship with corresponding particulate ^{9}Be distribution and hydrochemical data (e.g., dissolved oxygen) suggest three land-to-ocean pathways of ^{9}Be through estuaries. These are: i) riverine dissolved input after coastal scavenging, ii) ^{9}Be desorption from the suspended

particulate matter (SPM), and iii) coastal benthic inputs which involve porewater diffusion and/or submarine groundwater discharge. Among these pathways, benthic input potentially presents the most important contributor to the marine ^{9}Be budget and thus likely dominates the paleo-marine $^{10}Be/^{9}Be$ record. The concentration of dissolved oxygen in coastal bottom seawater may play a role in controlling the benthic ^{9}Be flux through time.

Despite the non-conservative behaviour of both dissolved ^{9}Be and ^{10}Be, the $^{10}Be/^{9}Be$ ratios of dissolved Be exhibit exponential increases along the salinity gradient, generally following the conservative water mixing lines, except where hypoxic bottom waters are affected by submarine groundwater discharge. In contrast, for sediment within the inner-shelf regions (approximately 150 km from the coast), a change in $^{10}Be/^{9}Be$ ratios of only within a factor of 2 is observed in authigenic (reactive) suspended and bottom sediment phases, indicating that a continent-derived $^{10}Be/^{9}Be$ signal is largely preserved in this zone. Beyond this zone where boundary currents prevail, reactive $^{10}Be/^{9}Be$ of outer-shelf/slope sediments markedly increase by a factor of 3 to 30. This increase is likely a result of water-sediment interactions through "boundary exchange" processes. Using the $^{10}Be/^{9}Be$ ratios of reactive phases of inner-shelf sediments, I calculated the denudation rates for the entire Changjiang and Amazon catchment and compared them with denudation rates derived from *in situ* cosmogenic beryllium isotopes. The good agreement (within a factor of 2) suggests that in large river-dominated shelves characterized by high sedimentation rates and weakened shoreward diffusion of seawater, the reactive $^{10}Be/^{9}Be$ ratio of coast-proximal sediments can be a direct recorder of terrigenous denudation of the adjacent river catchments.

In summary, with this thesis I demonstrate that the $^{10}Be/^{9}Be$ ratio in the authigenic phase of open ocean sediments is mainly sensitive to the benthic ^{9}Be flux, while the $^{10}Be/^{9}Be$ ratio in detrital continental inner-shelf sediments, less affected by "boundary exchange", can faithfully record the denudation rate of the adjacent river catchments. Thus, both systems are suited to explore past changes of these processes.

Zusammenfassung

Die Schnittstelle zwischen Land und Ozean ist die wichtigste Quelle oder Senke für viele Spurenelemente im Ozean. Die Untersuchung des geochemischen Verhaltens von Beryllium (Be)-Isotopen, einschließlich des kosmogenen Radionuklids ^{10}Be und des stabilen Nuklids ^{9}Be, und der Übertragungswege von Be an dieser Schnittstelle ist von entscheidender Bedeutung. Erstens ist die Kenntnis der Mechanismen des Be-Transfers eine Voraussetzung für die Anwendung des ozeanischen ^{10}Be/^{9}Be-Verhältnisses als empfindlicher Indikator für die frühere kontinentale Verwitterung. Zweitens wird das Verständnis des Be-Transfers zu unserem derzeitigen Wissen über marine biogeochemische Zyklen partikelreaktiver Spurenmetalle im Allgemeinen beitragen. Drittens trägt es dazu bei, die Anwendungsmöglichkeiten des ^{10}Be/^{9}Be-Verhältnisses in küstennahen Meeresumgebungen zu erweitern. Die Forschung auf diesem Gebiet, insbesondere zur Verteilung von ^{10}Be/^{9}Be in küstennahem Meerwasser, steht jedoch noch aus, da es schwierig ist, extrem niedrige Konzentrationen von ^{9}Be (auf der Ebene von pg/g) und ^{10}Be (auf der Ebene von einzelnen Atomen) im Meerwasser genau zu bestimmen.

In dieser Dissertation stelle ich ein neues, zeiteffizientes Verfahren für die gleichzeitige Anreicherung der äußerst niedrigen ^{9}Be- und ^{10}Be-Gehalte in (Küsten-)Meerwasser vor, basierend auf der Methode der Eisen-Kopräzipitation. Dieses neue Verfahren trägt zu einer zeiteffizienteren Handhabung der Proben, einem geringeren Risiko von Kreuzkontamination und einem genaueren ^{10}Be/^{9}Be-Verhältnis bei. Zudem habe ich die Eisen-Kopräzipitationsmethode im Hinblick auf folgende Aspekte bewertet: i) Einfluss der wichtigsten Matrixelemente auf die Genauigkeit der erhaltenen Be-Konzentrationen, ii) ihre Extraktionseffizienz für pg/g-Konzentrationen von Be in Gegenwart und Abwesenheit von organischem Material, und iii) Vergleich mit bestehenden Anreicherungsmethoden. Für die Bestimmung von ^{9}Be und ^{10}Be in Meerwasserproben aus dem offenen Ozean kann eine Präzision des ^{10}Be/^{9}Be-Verhältnisses von <5% mit weniger als 3 Litern Meerwasser erreicht werden, während vorher mehr als 20 Liter benötigt wurden, um diese Präzision zu erreichen. Selbst für küstennahes Meerwasser mit einer extrem niedrigen ^{10}Be-Konzentration von nur 100 Atomen/g ist eine maximale Meerwassermenge von 10 Litern ausreichend.

Ich habe dieses neue Verfahren zur Messung von gelöstem ^{9}Be und ^{10}Be entlang des gesamten Salzgehaltsgradienten in zwei der größten Ästuare der Erde angewandt: dem Changjiang- und dem Amazonas-Ästuar. Darüber hinaus habe ich die ^{10}Be- und ^{9}Be-Konzentrationen in verschiedenen chemisch extrahierbaren Fraktionen der entsprechenden Schwebstoffe und Bodensedimente bestimmt. Die Hauptziele waren i) die Untersuchung der Wege von terrigenem ^{9}Be in den Ozean unter verschiedenen hydrochemischen Bedingungen im Ästuar; und ii) die Schließung der derzeitigen Wissenslücke über die Verteilung von ^{10}Be/^{9}Be an der Land-Ozean-Grenzfläche und die Erkundung ihrer Anwendungsmöglichkeiten bei der Rekonstruktion früherer kontinentaler Denudationsraten der angrenzenden Flusseinzugsgebiete.

In beiden Ästuaren zeigen gelöstes ^{9}Be und ^{10}Be während der Vermischung ein ähnliches, nicht konservatives Verhalten. Der Abbau und die Freisetzung von gelöstem ^{9}Be im Changjiang-Ästuar und seine Beziehung zu den entsprechenden partikulären ^{9}Be-Verteilungen und hydrochemischen Wasserdaten (z. B. gelöster Sauerstoff) deuten auf drei Land-Ozean-Wege von ^{9}Be durch Ästuare hin. Diese sind: i) gelöster Eintrag aus Flüssen nach küstennaher Spülung, ii) Desorption von ^{9}Be aus Schwebstoffen (SPM, suspended particulate matter) und iii) benthische Einträge von der Küste, die Porenwasserdiffusion und/oder submarine Grundwasserabflüsse umfassen. Von diesen Wegen ist der benthische Eintrag möglicherweise der wichtigste Beitrag zum marinen ^{9}Be-Budget und damit entscheidend für die Interpretation der paläo-marinen ^{10}Be/^{9}Be-Aufzeichnungen. Die Konzentration von gelöstem Sauerstoff im Meeresbodenwasser der Küstengebiete könnte eine Rolle bei der Kontrolle des benthischen ^{9}Be-Flusses im Laufe der Zeit spielen.

Trotz des nicht konservativen Verhaltens von sowohl gelöstem ^{9}Be als auch ^{10}Be zeigen die ^{10}Be/^{9}Be-Verhältnisse einen exponentiellen Anstieg entlang des Salzgradienten. Grundsätzlich folgt dieser Anstieg den konservativen Wassermischungslinien, außer in Bereichen, wo hypoxisches Bodenwasser durch submarine Grundwassereinleitungen beeinflusst wird. Im Gegensatz dazu wird bei Sedimenten der inneren Schelfregionen (ca. 150 km von der Küste entfernt) eine Änderung des ^{10}Be/^{9}Be-Verhältnisses nur von einem Faktor 2 in authigenen (reaktiven) Schwebe- und Bodensedimentphasen beobachtet. Das deutet darauf hin, dass in dieser Zone ein vom Kontinent stammendes ^{10}Be/^{9}Be Signal weitgehend erhalten bleibt. Außerhalb dieser Zone, in der Grenzströmungen vorherrschen, steigt das reaktive ^{10}Be/^{9}Be in den Sedimenten des äußeren Schelfs und des Hangs deutlich um einen Faktor von 3 bis 30 an. Dieser Anstieg ist wahrscheinlich zurückzuführen auf Wasser-Sediment-Wechselwirkungen durch "Grenzaustausch"-Prozesse. Anhand der ^{10}Be/^{9}Be-Verhältnisse reaktiver Phasen an Sedimenten der inneren Schelfregion habe ich die Denudationsraten für das gesamte Einzugsgebiet des Changjiang und des Amazonas berechnet und sie mit Denudationsraten verglichen, die aus *in situ*-produzierten kosmogenen Berylliumisotopen abgeleitet wurden. Die gute Übereinstimmung (innerhalb eines Faktors 2) deutet darauf hin, dass das reaktive ^{10}Be/^{9}Be-Verhältnis küstennaher Sedimente in großen flussdominierten Schelfgebieten, gekennzeichnet durch hohe Sedimentationsraten und eine schwache küstenwärts gerichtete Diffusion von Meerwasser gekennzeichnet sind, ein direkter Indikator für die terrigene Denudation der angrenzenden Flusseinzugsgebiete sein kann.

Zusammenfassend zeige ich in dieser Dissertation, dass das ^{10}Be/^{9}Be-Verhältnis in der authigenen Phase von Sedimenten des offenen Ozeans hauptsächlich auf den benthischen ^{9}Be-Fluss anspricht. Hingegen kann das ^{10}Be/^{9}Be-Verhältnis in detritischen kontinentalen Innenschelfsedimenten, die weniger vom "Grenzaustausch" betroffen sind, die Denudationsrate der angrenzenden Flusseinzugsgebiete genau erfassen. Somit sind beide Systeme geeignet, um frühere Veränderungen dieser Prozesse zu erforschen.

Preface

This dissertation encompasses five chapters and is a cumulative collection of an introduction chapter, three main scientific chapters and a summary and outlook chapter.

Chapter 1 introduces the motivation and objectives of this dissertation. It also provides the necessary theoretical background of meteoric ^{10}Be and its stable counterpart ^{9}Be, a review of previous researches on the application of marine ^{10}Be/^{9}Be ratios and an overview of the study areas, materials and analytical methods employed in this dissertation.

Chapter 2 provides an improved procedure to preconcentrate ^{10}Be and ^{9}Be from seawater simultaneously based on the iron co-precipitation method. The development of this new procedure is supplemented with several validations of the iron co-precipitation method that have not been conducted previously. The work in this chapter has been published as:
Wang, C., Frick, D.A., von Blanckenburg, F., Frank, M., Lian, E., Yang, S. and Wittmann, H. (2023), Simultaneous preconcentration of ^{9}Be and cosmogenic ^{10}Be for determination of the ^{10}Be/^{9}Be ratio in (coastal) seawater. Limnology and Oceanography: Methods. https://doi.org/10.1002/lom3.10587. *This is an open access article under the terms of the* Creative Commons Attribution License*, which permits use, distribution and reproduction in any medium, provided the original work is properly cited.*

Author contribution statement: Hella Wittmann, Daniel A. Frick, and I designed the study. Martin Frank, Ergang Lian and Shouye Yang provided the natural seawater samples. Myself and Daniel A. Frick performed the laboratory analyses. I analysed the data, with substantial guidance and input from Daniel A. Frick, Hella Wittmann and Friedhelm von Blanckenburg. I wrote the original manuscript and all authors contributed to editing.

Chapter 3 is oriented towards understanding different pathways of terrigenous ^{9}Be into the ocean and their relative contributions to the marine ^{9}Be budget. The dissolved ^{9}Be in surface and bottom waters, as well as particulate ^{9}Be concentrations in different chemically extractable fractions of the corresponding suspended sediments are reported along the salinity gradient in the Changjiang Estuary. The geochemical behaviour of ^{9}Be in estuaries is also investigated in combination with hydro-physicochemical data (e.g., dissolved oxygen and dissolved inorganic phosphorus). The work in this chapter has been submitted to *Geochimica et Cosmochimica Acta.* and is under review (second round, major revisions for the first round) as:

Wang, C., von Blanckenburg, F., Lian, E., Yang, S., Perez, J., Wittmann, H.,. River-to-ocean pathways of beryllium-9 through estuaries.

Author contribution statement: Hella Wittmann, Friedhelm von Blanckenburg, and I proposed the study. Ergang Lian, Shouye Yang and I collected the samples. I prepared all the samples and performed the laboratory analyses for ^{9}Be and major elements concentrations.

Jeffrey Paulo Perez performed the analyses for specific surface area and X-ray diffraction. I wrote the original manuscript. All co-authors contributed to the discussions and improved the text of the manuscript.

Chapter 4 presents the first systematic data for ($^{10}Be/^{9}Be$) in paired coastal seawater and suspended particulate matter (SPM), as well as in the bottom sediments along the Changjiang-estuary-shelf and Amazon-estuary-shelf transects. This study accesses the "boundary exchange" processes and their potential effects on the $^{10}Be/^{9}Be$ signatures recorded in coastal seawater and authigenic phases of coastal sediments. In addition, it tests for the first time the applicability of using authigenic ($^{10}Be/^{9}Be$) in coast-proximal sites sediments to trace present and past denudation rates of the adjacent river catchments. The work in this chapter is in preparation for the submission to a peer-reviewed journal.

Author contribution statement: Hella Wittmann, Friedhelm von Blanckenburg, and I proposed the study. Martin Frank, Ed Hathorne, Florian Scholz, Ergang Lian, Shouye Yang and I collected the samples. I carried out all the laboratory analyses and wrote this original manuscript.

Chapter 5 summarizes concluding remarks of this dissertation and proposes future perspectives to address gaps in current knowledge and limitation.

Contents

Chapter 1 Introduction

1.1 Motivation and objectives

The land-ocean interface is considered to be a key interface in controlling the biogeochemical dynamics and cycling of trace elements and their isotopes (TEIs) in the ocean (Anderson, 2020; Charette et al., 2016; Jeandel, 2016). In general, this transition zone includes the 'proximal' estuaries, bays, lagoons, and banks, as well as the 'distal' continental and island shelves, oceanic slopes, and adjacent marginal seas (Mackenzie et al., 2011). Rivers transport trace elements in both dissolved and particulate forms into the ocean. Through estuaries where fresh water mixes with brackish water, particle-reactive elements such as Fe and rare earth elements (REEs) are typically removed from waters due to colloidal flocculation (Boyle et al., 1977; Hunter and Leonard, 1988; Sholkovitz and Szymczak, 2000; Sholkovitz et al., 1978; Xu et al., 2023), while other elements like Ba and Ra are desorbed from riverine particles into waters (Carroll et al., 1993; Coffey et al., 1997; Colbert and McManus, 2005; Hancock and Murray, 1996; Li et al., 2021a). On the other hand, sediments deposited on continental shelves may release trace elements into porewaters during early sediment diagenesis and act as another important source of trace elements through biological and diffusive processes (Aller et al., 1985; Elrod et al., 2004; Froelich et al., 1979; Lacan and Jeandel, 2005). Advective transport of fresh and brackish water through sediment pores, a process named "submarine groundwater discharge" (SGD) also contributes substantially to marine trace element budgets (Burnett et al., 2001; Moore, 1996; Moore, 2010).

Identifying and quantifying all the pathways described above is critical to our understanding of marine trace element cycles and to employing them as proxies for past environments (SCOR Group, 2007), which is also one of the major goals of the GEOTRACES program (www.geotraces.org). Over the past few decades, extensive research has been conducted on the behaviour of TEIs at this key interface. The primary TEIs of interest encompass: (1) micronutrients such as Fe, Si and Co, which control the structure of ocean ecosystems and their biological productivity, thus regulating the ocean carbon cycle (e.g., Elrod et al., 2004; Petit et al., 2015; Zhang et al., 2020); (2) contaminants (e.g., Cd, Pb, and As) that can be used to trace anthropogenic emissions (e.g., Martin et al., 1993; Zhao et al., 2013), and (3) other tracers such as isotopes of Nd, U, Th that are exploited to reconstruct past marine conditions (e.g., patterns and rates of ocean circulation, ocean anoxia) (Hayes et al., 2013; Jeandel et al., 2007; Pogge von Strandmann et al., 2011; Xu et al., 2023). However, an important, but still much overlooked member of these trace elements is beryllium (Be).

In comparison to other marine isotope tracers, beryllium isotopes offer unique advantages in identifying and quantifying different sources and sinks occurring at the land-ocean interface (Brown et al., 1992b). This is because the meteoric cosmogenic radionuclide ^{10}Be is produced

in the atmosphere and deposited into the ocean at a known rate (Field et al., 2006; Heikkilä et al., 2013; Heikkilä and Smith, 2013), while the stable isotope ^{9}Be primarily enters the ocean via riverine input (see details in section 1.3.1), and its flux can thus be estimated from the ^{10}Be/^{9}Be ratio in marine authigenic sediments (von Blanckenburg and Bouchez, 2014). Given the well-constrained and the particle-reactive nature of Be in seawater, understanding pathways of ^{9}Be at the land-ocean interface will significantly contribute to our current knowledge of marine biogeochemical cycles of other particle reactive trace metals, such as Fe and REEs.

In addition, knowledge of the behaviour and distributions of ^{10}Be and ^{9}Be at this transition setting is also a prerequisite for applying oceanic ^{10}Be/^{9}Be ratio as proxies for past environmental changes, such as continental weathering flux (Caves Rugenstein et al., 2019; von Blanckenburg and Bouchez, 2014; von Blanckenburg et al., 2015; Willenbring and von Blanckenburg, 2010a) and ^{10}Be production changes resulting from variations of Earth's magnetic field (Carcaillet et al., 2004; Christl et al., 2003; Knudsen et al., 2008; Masarik and Beer, 2009; Simon et al., 2018; Simon et al., 2020). In particular, the application of the marine authigenic ^{10}Be/^{9}Be ratio as a past continental weathering tracer has been questioned recently (Deng et al., 2023; Li et al., 2021b; Li et al., 2022; von Blanckenburg et al., 2022) due to the incomplete understanding of ^{9}Be pathways at the land-ocean interface (see details in section 1.3.2). On the other hand, the divergent pathways of ^{10}Be and ^{9}Be into the ocean and the relatively short residence time of Be in oceans (ca. 500-1200 years) lead to distinguishable ^{10}Be/^{9}Be ratios across coastal and open ocean settings, as well as among different ocean basins (Bourlès et al., 1989a; Brown et al., 1992b; Frank et al., 2009; Kong et al., 2021b; Ku et al., 1990; Kusakabe et al., 1987; Measures et al., 1996; Sarathi Jena et al., 2022; von Blanckenburg and Igel, 1999). This enables the ^{10}Be/^{9}Be ratio to be a tracer for a variety of oceanic processes, such as water mass mixing (Frank et al., 2009; Frank et al., 2002; Kong et al., 2021b), deep marine circulation (von Blanckenburg et al., 1996), boundary exchange/scavenging (Anderson et al., 1990; Wittmann et al., 2017), and reverse weathering (Bernhardt et al., 2020). Nevertheless, our understanding of the distribution of ^{10}Be/^{9}Be at the land-ocean interface and its controlling factors is still poor due to the limited available ^{10}Be/^{9}Be data in coastal seawater and sediments, which leaves the potential of this tracer underutilized.

An important reason for the scarcity of ^{10}Be/^{9}Be data in costal seawater is analytical challenges that arise from the extremely low concentrations of beryllium and its isotopes in seawater (typically at the pg/g level for ^{9}Be and ca. 100-2000 atoms/g for ^{10}Be) (Frank et al., 2009; Frank et al., 2002; Kong et al., 2021b; Ku et al., 1990; Kusakabe et al., 1987; Measures and Edmond, 1982; Measures and Edmond, 1983; Measures et al., 1996) relative to extremely high concentrations of the seawater matrix (e.g., Na, Mg, K, and Ca ranging from hundreds to tens of thousands of μg/g). Precise measurements of such low Be concentrations thus require methods that enable the preconcentration of Be, that is, the separation of Be from the seawater matrix and its concentration into a small volume (i.e., a few mL). Over the past few decades,

preconcentration and determination of ^{9}Be and ^{10}Be in seawater have routinely been carried out separately. For ^{10}Be preconcentration, the most routinely used method is the iron co-precipitation method (Frank et al., 2009; Frank et al., 2002; Kong et al., 2021b; Ku et al., 1990; Kusakabe et al., 1987), whereas for ^{9}Be, a variety of methods have been employed, including hydroxide co-precipitation (Hiraide et al., 1994), liquid-liquid extraction (Measures and Edmond, 1986; Bashir and Paull, 2001), micelle-mediated extraction (Afkhami et al., 2007; Beiraghi and Babaee, 2008), and solid-phase extraction (SPE) (Amin, 2001; Yousefi et al., 2010; Tazoe et al., 2014). While ^{10}Be in seawater is measured routinely by accelerator mass spectrometry (AMS) (Müller et al., 2008; Suter, 1990; Vogel et al., 1995), numerous techniques have been employed for the determination of ^{9}Be. These encompass electron capture detection gas chromatography (ECD-GC) (Measures and Edmond, 1986), graphite furnace atomic absorption spectrometry (GFAAS) (Hiraide et al., 1994), inductively coupled plasma atomic emission spectroscopy (ICP-AES) (Beiraghi and Babaee, 2008), and inductively coupled plasma mass spectrometry (ICP-MS) (Tazoe et al., 2014). The existing protocols for seawater ^{10}Be/^{9}Be ratio determination using the above mentioned preconcentration and analytical techniques are time-consuming, and different preconcentration methods employed for ^{9}Be and ^{10}Be may result in different recoveries for ^{9}Be and ^{10}Be in the same sample, leading to inaccurate ^{10}Be/^{9}Be ratios.

In this thesis, I first develop a new procedure based on the iron co-precipitation method that enables simultaneous preconcentration of ^{9}Be and ^{10}Be from seawater, with the aim to enable more efficient preconcentration of Be isotopes from seawater and to derive more accurate seawater ^{10}Be/^{9}Be ratios (Chapter 2). Building upon on this, I systematically measured ^{10}Be and ^{9}Be in coastal seawater, suspended sediments and bottom sediments from two representative, large estuaries worldwide: the Changjiang and the Amazon estuary. The objectives are 1) to investigate terrigenous ^{9}Be pathways into the ocean under a variety of hydro-chemical estuarine conditions and its implication for the oceanic ^{10}Be/^{9}Be ratio as a continental weathering input tracer (Chapter 3), and 2) to fill the current knowledge gap of the distribution of ^{10}Be/^{9}Be at the land-ocean interface along salinity gradients and explore potential applications of ^{10}Be/^{9}Be ratios in coastal oceans (Chapter 4).

1.2 Basic principles of ^{9}Be and meteoric ^{10}Be

Beryllium is a rare but widely distributed alkaline earth metal. It chemically differs from other alkaline earth elements, because it has the smallest radius (0.31 Å) of the group, and the bonds formed by beryllium are stronger and covalent in nature than the typical ionic bonds formed by the other alkaline earth elements (Everest, 1964). The covalent nature of the beryllium bonding is reflected in its preference for hydrolysis to mono- and polynuclear species (Baes Jr and Mesmer, 1981). In aqueous solutions, its speciation is highly dependent on pH (Fig. 1.1), but also affected by other ligands (Alderighi et al., 2000; Takahashi et al., 1999).

In the absence of humic acid, most Be exists as hydrolyzed species at pH greater than 5 (Fig. 1.1a). When humic acid is present, Be is found to be present as humate complex within the pH range of 3 to 11 (Takahashi et al., 1999) (Fig. 1.1b). Given the reactive nature of Be-hydroxides and Be-humate complex, they tend to be absorbed readily onto particle surfaces, and preferably onto particles with high specific surface area, such as Fe-oxyhydroxides, Al-hydroxides, and clay minerals (Willenbring and von Blanckenburg, 2010b). Therefore, the solubility of beryllium is very low in neutral to weakly alkaline aqueous solutions, like seawater.

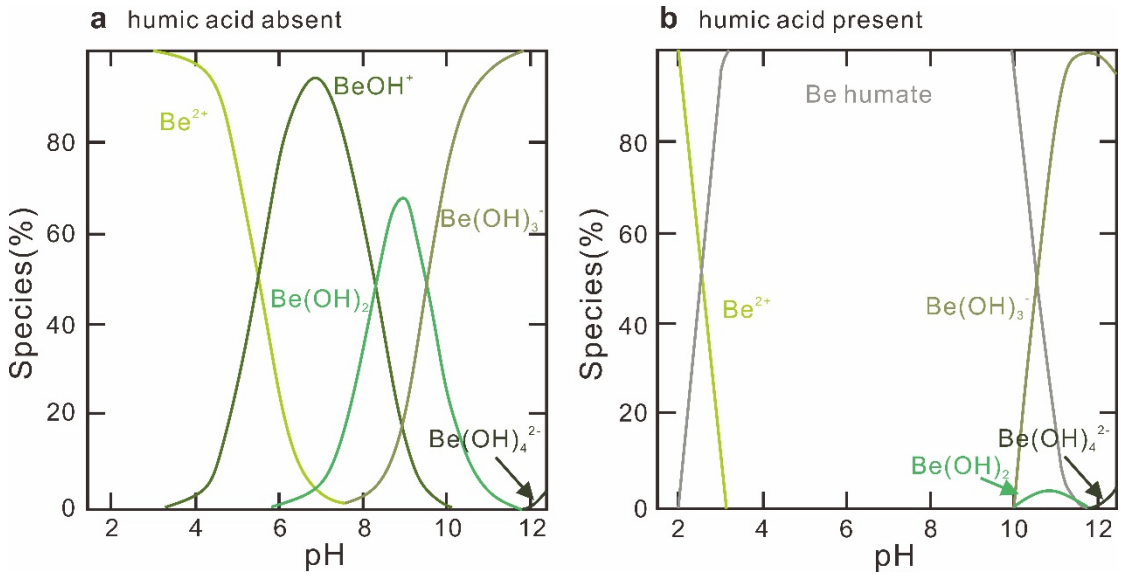

Figure 1.1 Beryllium species in aqueous solutions in the absence and presence of humic acid (30 mg/L). The concentration of solutes is assumed to be 0.02 M. Figure is modified from Takahashi et al. (1999).

Among the twelve isotopes of beryllium, ^{9}Be is the only stable isotope. The ^{9}Be occurs in continental crust with an average concentration of a few μg/g (Armiento et al., 2013). During weathering, a fraction of ^{9}Be is released from primary minerals and partitioned into the dissolved and "reactive" (adsorbed or co-precipitated) phases. The distribution of ^{9}Be between dissolved and "reactive" phases depends on the partition coefficient (K_d), which typically varies between 10^3 and 10^6 in natural systems (Willenbring and von Blanckenburg, 2010b). In contrast to the stable ^{9}Be, the radioactive meteoric ^{10}Be (half-life 1.39 Ma) is produced primarily by spallation of nitrogen and oxygen by high-energy cosmic rays in the upper atmosphere (Lal and Peters, 1967). The production rate of ^{10}Be depends on the primary cosmic ray flux, which is influenced by solar activity and the geomagnetic field intensity (Masarik and Beer, 2009). After production, ^{10}Be gets well-mixed in the stratosphere (~1 yr) and is hydrolysed mainly to $^{10}Be(OH)_2$. The reactive $^{10}Be(OH)_2$ is rapidly adsorbed onto aerosols and delivered into ocean/continent reservoirs by wet (rain or snow) and dry (dust) deposition. The depositional flux of ^{10}Be thus largely depends on aerosol loading and climatic factors, and exhibits distinct temporal and spatial variability (Field et al., 2006; Graly et al., 2011; Heikkilä et al., 2013;

Heikkilä and Smith, 2013). The depositional rate of ^{10}Be can be estimated from General Circulation Models (GCM) (Field et al., 2006; Heikkilä et al., 2013; Heikkilä and Smith, 2013) combined with ^{10}Be production functions (Masarik and Beer, 2009) and aerosol dynamics (Stier et al., 2005), or site-specifically by ^{10}Be inventories in dated soil profiles (Deng et al., 2021; Dixon et al., 2018; Graly et al., 2011) and in precipitation collections (Graham et al., 2003; Heikkilä et al., 2008; Monaghan et al., 1986). Current knowledge suggests that ^{10}Be deposition fluxes can vary spatially between 0.06 and 3.8×10^6 atoms/cm^2/year (Heikkilä and Smith, 2013; Heikkilä and von Blanckenburg, 2015), and that during geomagnetic excursions and reversal events the ^{10}Be deposition fluxes are almost twice the current values (Heikkilä et al., 2013; Ménabréaz et al., 2011; Simon et al., 2020).

1.3 Open-ocean ^{10}Be/^{9}Be ratio as a weathering flux tracer

1.3.1 Sources of ^{9}Be and ^{10}Be to the ocean

The ^{9}Be can enter the ocean via the following pathways: (1) river input, (2) aeolian input, (3) submarine groundwater discharge, and (4) hydrothermal input. Among these four pathways, the ^{9}Be flux sourced from submarine groundwater discharge remains unexplored, and has not been included into current oceanic ^{9}Be budget calculation. The hydrothermal input is considered to be negligible, because ^{9}Be from hydrothermal sources is removed within the plume or its near field due to the high particle concentration around the hydrothermal vents (Bourlès et al., 1994). In the early 1990s, aeolian input was widely assumed to be the primary source of ^{9}Be in the deep oceans based on limited marine ^{10}Be/^{9}Be data and simple mass balance calculations (Brown et al., 1992b; Kusakabe et al., 1991). The riverine input was assumed to be insignificant, because most of the dissolved riverine ^{9}Be was removed in the estuaries possibly by high particulate load (Brown et al., 1992b; Kusakabe et al., 1991; Measures and Edmond, 1983). With a more comprehensive global distribution of ^{10}Be/^{9}Be in deep seawater as derived from Fe-Mn crusts, von Blanckenburg et al., (1996) demonstrate that the aeolian input maybe a less important source than river input. One line of evidence is that under equal ^{10}Be flux, the ^{10}Be/^{9}Be ratios in deep seawaters in areas with high dust influx are not always low (von Blanckenburg et al., 1996). On the other hand, if assuming the aeolian input to be the principal source of ^{9}Be, unrealistically high degrees of dissolution of >50% would be required to balance the marine ^{9}Be budget. Therefore, river input is likely the most important source of oceanic ^{9}Be. Rivers transport ^{9}Be to the ocean not only in dissolved phase, but also in particulate phase (Fig. 1.2). After entry into the coastal ocean, the dissolved ^{9}Be can be further delivered to the open ocean after estuarine removal, while the particulate ^{9}Be sinks with settling particles to coastal sediments (von Blanckenburg and Bouchez, 2014). During early diagenesis, ^{9}Be in the “reactive” phase of coastal sediments can be released into seawater via porewater diffusion/expulsion (Bourlès et al., 1989b; von Blanckenburg et al., 1996; von Blanckenburg and Bouchez, 2014; von Blanckenburg et al., 2015; von Blanckenburg et al., 2022). The ocean

receives ^{10}Be primarily from atmospheric precipitation, while the contribution from riverine and aeolian inputs are recognized as negligible (Kusakabe et al., 1990; McHargue and Damon, 1991; von Blanckenburg and Bouchez, 2014; Willenbring and von Blanckenburg, 2010b).

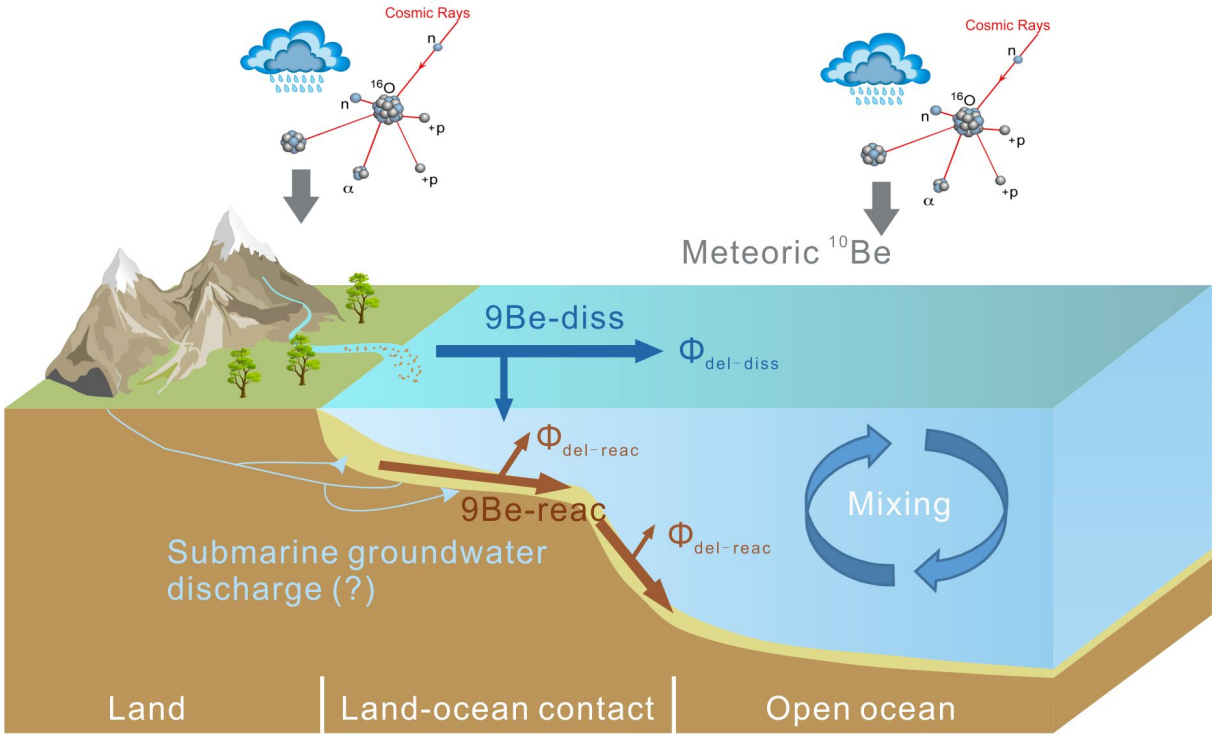

Figure 1.2 The main entry pathways of ^{9}Be and ^{10}Be into the open ocean, modified from von Blanckenburg et al. (2015). $\Phi_{del-diss}$ represents the fraction of dissolved riverine ^{9}Be that escapes the coastal trap. $\Phi_{del-reac}$ describes the fraction of reactive particulate-bound ^{9}Be that is dissolved into seawater.

1.3.2 Framework of oceanic ^{10}Be/^{9}Be ratio as a weathering flux tracer

The open ocean serves as a binary mixing "bowl" where ^{9}Be, mostly derived from riverine input, mixes with the direct input of meteoric ^{10}Be to the surface ocean. The oceanic ^{10}Be/^{9}Be ratio is thus set as (von Blanckenburg and Bouchez, 2014; von Blanckenburg et al., 2015) :

$$\left(\frac{^{10}Be}{^{9}Be}\right)_{ocean} = \frac{J_{ocean}^{10Be}}{J_{riv-diss}^{9Be} + J_{riv-reac}^{9Be}} \quad (1.1)$$

where J_{ocean}^{10Be} is the total meteoric input of ^{10}Be deposited onto the ocean (in mass/time). $J_{riv-diss}^{9Be}$ and $J_{riv-reac}^{9Be}$ are the net inputs of riverine dissolved and reactive ^{9}Be into the ocean, representing dissolved riverine ^{9}Be fluxes that escape coastal trap and the reactive ^{9}Be flux that is released from ocean bottom sediments. The net dissolved input $J_{riv-diss}^{9Be}$ is the product of river discharge (Q, in volume/time), dissolved ^{9}Be concentration in river water ($[^{9}Be]_{diss}$, in mass/volume) and the fraction of dissolved riverine ^{9}Be that escapes the coastal trap ($\Phi_{del-diss}$).

The net reactive input $J_{riv-reac}^{9Be}$ depends on riverine sediment load, which can be calculated from basin area (A, in area) and erosion rate (E, in mass/area/time), reactive ^{9}Be concentration in river sediments ($[^{9}Be]_{reac}$, in mass/mass) and fraction of reactive particulate-bound ^{9}Be that is released into seawater ($\Phi_{del-reac}$). Thus, equation 1.1 can be rewritten as (von Blanckenburg et al., 2015):

$$(\frac{^{10}Be}{^{9}Be})_{ocean} = \frac{J_{ocean}^{10Be}}{Q * [\,^{9}Be]_{diss} * \Phi_{del-diss} + A * E * [\,^{9}Be]_{reac} * \Phi_{del-reac}} \quad (1.2)$$

Given that J_{ocean}^{10Be} can be calculated directly from known variations in the ^{10}Be depositional flux and the surface area of the oceans, the $(^{10}Be/\,^{9}Be)_{ocean}$ is mainly set by the riverine ^{9}Be flux through the above two pathways (as illustrated in Fig. 1.2).

Over glacial-interglacial time scales (10^4 yr-time scale), assuming the contribution from reactive ^{9}Be flux to $(^{10}Be/\,^{9}Be)_{ocean}$ is negligible (i.e., $\Phi_{del-reac}$ is small enough), the $(^{10}Be/\,^{9}Be)_{ocean}$ will be sensitive only to variations in the net dissolved Be flux, which is considered as an undamped proxy for weathering flux if $\Phi_{del-diss}$ remain unchanged (von Blanckenburg et al., 2015). The sharp variations observed for other radiogenic isotopes (e.g., Nd and Pb) in marine records over glacial-interglacial time scales indicate that the weathering flux is not damped at this time scale (von Blanckenburg et al., 2015).

Over the 10^5 to 10^6 yr-time scale, the riverine ^{9}Be flux including both dissolved and reactive fluxes is ultimately controlled by supply of dissolved or reactive ^{9}Be to the weathering zone through mineral dissolution and hence by denudation rate (von Blanckenburg and Bouchez, 2014). Since ^{9}Be present in the reactive phase is initially released through primary mineral dissolution, the total flux of reactive and dissolved ^{9}Be is ultimately also the weathering flux that is a fraction of the denudation rate (von Blanckenburg and Bouchez, 2014). If $\Phi_{del-diss}$ and $\Phi_{del-reac}$ remain constant through time, the $(^{10}Be/\,^{9}Be)_{ocean}$ variations can thus track the variations of past weathering flux over this time scale (von Blanckenburg et al., 2015).

In summary, the sensitivity of the $(^{10}Be/\,^{9}Be)_{ocean}$ as a tracer for past continental weathering flux primarily depends on the faction of dissolved riverine ^{9}Be escaping the coastal trap and the fraction of reactive ^{9}Be releasing into the ocean. I will next give an overview of the recent research progress on this topic.

1.3.3 Efficiency of ^{9}Be transmission through the land-ocean interface

The fraction of dissolved riverine ^{9}Be escaping the coastal trap can be estimated from the dissolved ^{9}Be behaviour during estuarine mixing. So far, studies on dissolved ^{9}Be behaviour have been conducted in seven specific estuaries (Brown et al., 1992b; Kong et al., 2021a; Kusakabe et al., 1991; Measures and Edmond, 1983; Suhrhoff et al., 2019). Among these

estuaries, only the Amazon and Congo River estuaries exhibit ^{9}Be removal (Brown et al., 1992b; Measures and Edmond, 1983). In contrast, the Ganges, Changjiang (Yangtze River), Pearl River and Zrmanja estuaries are characterized by ^{9}Be addition to varying degrees (Brown et al., 1992b; Kusakabe et al., 1991; Measures and Edmond, 1983; Suhrhoff et al., 2019) A small estuary in Scotland, Loch Etive, however displays nearly conservative mixing behaviour (Suhrhoff et al., 2019), meaning no removal or addition of dissolved ^{9}Be during estuarine mixing. By weighting the removal/release of dissolved ^{9}Be by the respective riverine ^{9}Be fluxes from each river, Suhrhoff et al. (2019) provided the first estimation for the coastal removal for dissolved ^{9}Be flux to be 56%. This suggests that about 44% of riverine dissolved ^{9}Be can be eventually delivered to the open ocean after the coastal trap. The controlling factors accounting for ^{9}Be removal and their changes over time still remain largely unexplored. A mixing experiment conducted by Suhrhoff et al. (2019) suggested that the colloidal composition in river water may play a role: the ^{9}Be complexation with organic colloids facilitates its transport across estuaries, whereas the presence of inorganic complexants results in removal.

The reactive ^{9}Be flux released from ocean bottom sediments to the ocean can be quantified using porewater ^{9}Be profile. Based on porewater ^{9}Be data from four continental margins, Deng et al. (2023) provided the first comprehensive estimation for ^{9}Be flux through porewater diffusion. This diffusion flux is estimated to be about 1.1×10^{7} mol/year, equivalent to ~60% of the net riverine dissolved input (i.e., the dissolved ^{9}Be flux after coastal trap) (Deng et al., 2023). However, when taking advection on shelves into account, the released ^{9}Be flux can be up to $4.5 \pm 2.9 \times 10^{7}$ mol/year, which is comparable to, or even higher than the net dissolved ^{9}Be flux (Deng et al., 2023). The release of ^{9}Be from bottom sediments has the potential to change with time in response to sedimentary processes, such as organic carbon delivery and sedimentary delivery. However, key factors have yet to be explored (Deng et al., 2023).

1.4 Applications of ^{10}Be/^{9}Be ratio at land-ocean interface

Due to the divergent pathways by which ^{10}Be and ^{9}Be are introduced into the ocean, seawater generally has higher ^{10}Be concentrations and lower ^{9}Be concentrations than river water, resulting in higher ^{10}Be/^{9}Be ratios in seawater (typically between 10^{-8} and 10^{-7}) (Frank et al., 2009; Ku et al., 1990; Kusakabe et al., 1987; Measures et al., 1996) than in river water (typically between 10^{-10} and 10^{-9}) (Brown et al., 1992a; Dannhaus et al., 2018; Kusakabe et al., 1991; Wittmann et al., 2015). This nearly two orders of magnitude difference allows the ^{10}Be/^{9}Be ratio at the land-ocean interface to be a sensitive tracer of changes in the composition of terrestrial particles as a result of exchange with seawater (Wittmann et al., 2017). By comparing ^{10}Be/^{9}Be ratios in authigenic surface sediments offshore Chile with their riverine source, Wittmann et al. (2017) deciphered that for continental margin sediments, a marine authigenic rim recording seawater signal is formed through co-precipitation onto the pre-existing riverine authigenic phase. This alteration occurs only 30 km from the coast. Therefore, in such settings,

the $^{10}Be/^{9}Be$ ratio in authigenic surface sediments is not applicable for tracing river-basin or ocean-basin denudation rates (Wittmann et al., 2017).

At the same sites, Bernhardt et al. (2020) also observed a nearly fourfold increase in $^{10}Be/^{9}Be$ ratios from riverine to marine clay-sized fraction of sediments. This increase indicates the formation of a new silicate phase in marine surface sediment, which likely occur through the dissolution of marine biogenic opaline silica (inheriting the high $^{10}Be/^{9}Be$ ratio of seawater) during reverse weathering. Thus, the $^{10}Be/^{9}Be$ ratio in clay-sized marine sediment bears potential as a high-sensitivity proxy for the formation of marine authigenic clays (Bernhardt et al., 2020).

1.5 Study area, materials and methods

1.5.1 Study areas

The Changjiang River is the third longest river in the world, flowing 6300 km eastwards from the Tibetan Plateau into the East China Sea. It historically delivered ~900 km^3/yr of water and ~470 Mt/yr of sediment into the Changjiang Estuary and the adjacent sea (Milliman and Farnsworth, 2011). The Changjiang Estuary is a mesotidal, partially mixed estuary, with a tide of regular semidiurnal type. Circulation in the Changjiang Estuary and the adjacent region is mainly governed by the Changjiang Diluted Water (CDW), Zhe-Min Coastal Current (ZMCC), and Taiwan Warm Current (TWC) (Su, 2001) (Fig. 1.3a). The southward ZMCC is most active during winter, carrying water and sediments from the Changjiang River southward along the inner shelf (Beardsley et al., 1985; Lee and Chao, 2003). In summer, the northward TWC intensifies due to the prevailing southeast monsoon and largely weakens the southward transport of sediments along the coast (Beardsley et al., 1985; Lee and Chao, 2003). It is estimated that ~40% of the fluvial sediment is trapped in the estuary, and the remaining 60% is transported to the neighbouring continental shelf of the ECS by coastal currents (Liu et al., 2006; Milliman et al., 1985). From the complex and dynamic interactions between runoff, stratification and tides (Li and Zhang, 1998; Wu et al., 2012), a turbidity maximum zone develops in the river mouth zone of the Changjiang Estuary where the bottom SPM concentration can be >10 g/L (Lin et al., 2020). Hypoxic conditions usually occur below the pycnocline in summer, reaching a maximum in August, then weaken in autumn, and finally disappear in winter (Zhu et al., 2016).

The Amazon River is the world's largest fluvial system in terms of annual water discharge (~6600 km^3/yr, Callède et al. (2010)) and drainage area (~6.1×10^6 km^2). It presently exports a total sediment load of ~400-1500 Mt/yr to the Atlantic Ocean (Armijos et al., 2016; Dunne et al., 1998; Martinez et al., 2009; Meade et al., 1985). The Amazon estuary is classified as macrotidal (Gallo and Vinzon, 2017) and semidiurnal (Kosuth et al., 2009) with a tidal range between 4 and 6 m at the mouth. The continental shelf is more than 300 km wide off the river

mouth. Circulation on the Amazon shelf is influenced by the interaction of the freshwater plume (Amazon Outflow, AO) with strong tidal currents and the north-westward flowing North Brazilian Current (NBC) (Kineke et al., 1996; Rockwell Geyer et al., 1996) (Fig. 1.3b). The NBC flows along the Amazon outer shelf and slope as a western boundary current 100-200 km wide and 500 m deep (Flagg et al., 1986). The highly dynamic current system on the Amazon shelf results in strong turbulence on the shelf sediments and frequent resuspension, which continuously rework up to 150 cm of the upper sediment package (Kuehl et al., 1986).

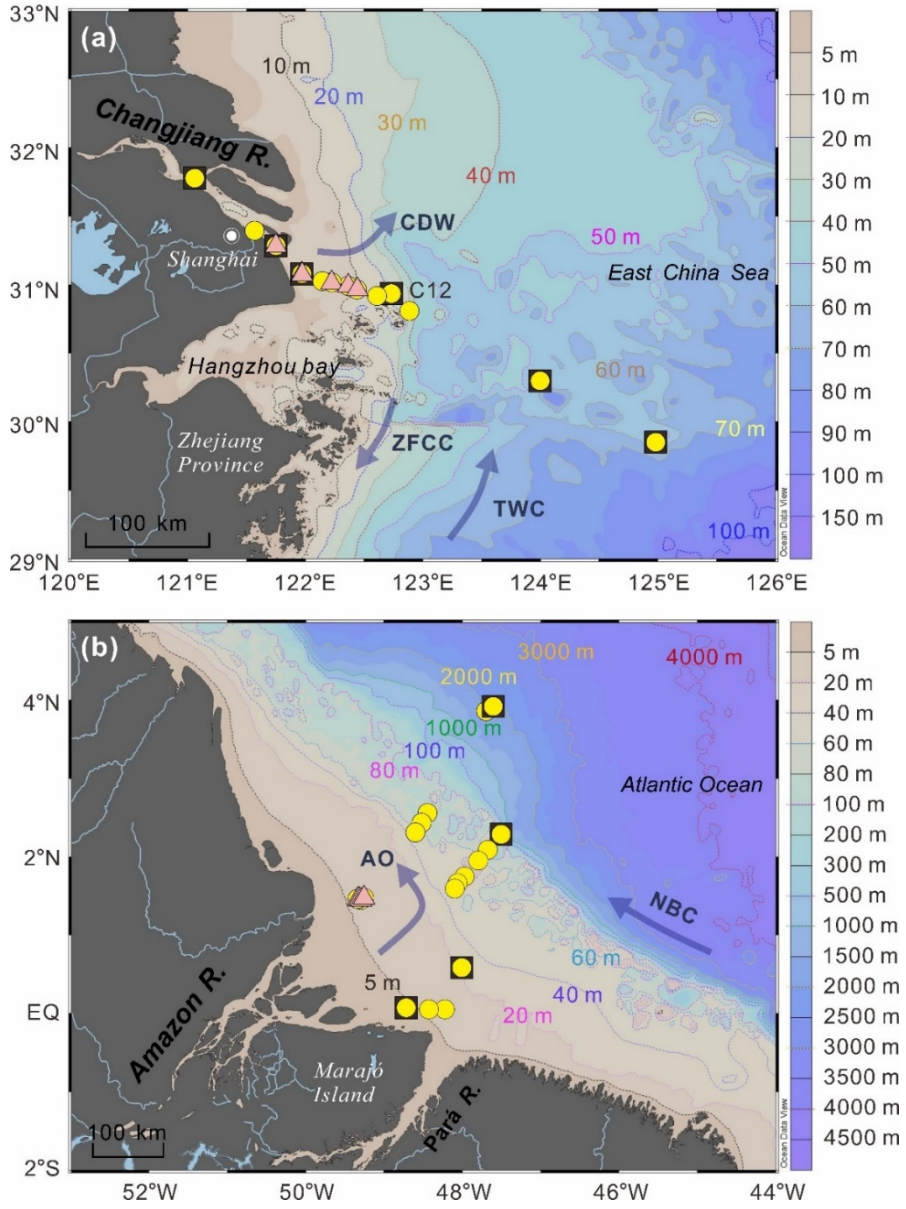

Figure 1.3 Bathymetric maps of the study area showing the locations of water samples (yellow circles), suspended particulate matter (pink triangles) and bottom sediments (black squares) along the Changjiang-estuary-shelf (a) and the Amazon-estuary-shelf (b) transects. Major water masses are indicated: CDW, Changjiang Diluted Water; TWC, Taiwan Warm Current; ZFCC, Zhe-Min Coastal Current; AO, Amazon Outflow; NBC, North Brazil Current.

1.5.2 Sampling, sample preparation, and measurements

Sampling along the Changjiang-estuary-shelf transect was conducted between 27 August and 4 September 2019 during the cruise of the *Key Elements Cycling in the Changjiang-Estuary-Shelf Transect* (KECES 2019) organized by the State Key Laboratory of Marine Geology, Tongji University, and the Amazon-estuary-shelf transect between 29 April and 20 May 2018 during research cruise M147 RV Meteor (Koschinsky et al., 2018), respectively. Samples collected include seawater, suspended particulate matter (SPM) and ocean bottom surface sediments (see locations in Fig. 1.3). Details of the sampling can be found in Chapter 4.

Prior to analysis, seawater samples were preconcentrated using the iron-coprecipitation method. Details for the preconcentration procedure can be found in Chapter 2. For SPM and ocean bottom sediments, I employed a sequential leaching procedure (Wittmann et al., 2012) to extract Be in different operationally defined fractions, including: the exchangeable fraction (ex), the reactive amorphous oxy-hydroxide fraction (am-ox), the crystalline oxides fraction (x-ox) and the organic (org) fraction. The exchangeable and organic fractions were only extracted and measured for specific SPM samples from the Changjiang Estuary, given the negligible Be concentrations in these two fractions. Detailed procedure for the sequential leaching can be found in Chapter 3 and Wittmann et al., (2012). Prior to chemical extraction, bottom sediments were dry-sieved into a fraction of <63 μm.

The ^{9}Be concentrations for water samples and sediment exchangeable fractions were measured on a sector-field high-resolution inductively coupled plasma-mass spectrometer (HR-ICP-MS, Element2, Thermo Fisher Scientific) operated in low-resolution mode. Except for the exchangeable fraction, the ^{9}Be and other elemental analyses for other fractions of SPM and bottom sediments were performed using ICP-OES. All the measurements above were carried out in the Helmholtz Laboratory for the Geochemistry of the Earth Surface at GFZ Potsdam, Germany (von Blanckenburg et al., 2016). The ^{10}Be concentrations for both water and sediments samples were obtained from AMS measurements of $(^{10}Be/^{9}Be)_{carrier}$ ratios at University of Cologne. Further details concerning instrumental operational conditions and specific analytical methods are extensively discussed and presented in the following chapters.

Chapter 2 Simultaneous preconcentration of ^{9}Be and cosmogenic ^{10}Be for determination of the ^{10}Be/^{9}Be ratio in (coastal) seawater

Abstract

Beryllium isotopes have emerged as a quantitative tracer of continental weathering, but accurate and precise determination of the cosmogenic ^{10}Be and stable ^{9}Be in seawater is challenging, because seawater contains high concentrations of matrix elements but extremely low concentrations of ^{9}Be and ^{10}Be. In this study, we develop a new, time-efficient procedure for the simultaneous preconcentration of ^{9}Be and ^{10}Be from (coastal) seawater based on the iron co-precipitation method. The concentrations of ^{9}Be, ^{10}Be, and the resulting ^{10}Be/^{9}Be ratio for Changjiang Estuary water derived from the new procedure agree well with those obtained from the conventional procedure requiring separate preconcentration for ^{9}Be and ^{10}Be determinations. By avoiding the separate preconcentration, our newly developed procedure contributes toward more time-efficient handling of samples, less sample cross-contamination, and a more reliable ^{10}Be/^{9}Be ratio. Prior to this, we validated the iron co-precipitation method using artificial seawater and natural water samples from the Amazon Estuary regarding: i) the "matrix effect" for Be analysis, ii) its extraction efficiency for pg/g-levels Be in the presence and absence of organic matter, and (iii) the data comparability with another preconcentration method. We calculated that for the determination of ^{9}Be and ^{10}Be in most open ocean seawater with typical ^{10}Be concentrations of > 500 atoms/g, good precisions (<5%) can be achieved using less than 3 L of seawater compared to more than 20 L routinely used previously. Even for coastal seawater with extremely low ^{10}Be concentration (e.g., 100 atoms/g), we estimate a maximum amount of 10 L to be adequate.

2.1 Introduction

Cosmogenic beryllium-10 (^{10}Be, $T_{1/2}$ = 1.39 Myr) is produced in the atmosphere at a known rate and reaches Earth's surface and oceans by wet and dry deposition (Willenbring and von Blanckenburg, 2010b), while its stable counterpart ^{9}Be is released from rocks by chemical weathering and is transferred to the oceans mainly by rivers (von Blanckenburg and Bouchez, 2014). Due to the particle-reactive nature of Be, more than 90% of Be (^{9}Be and ^{10}Be) are trapped in the coastal area when transported to the oceans via rivers (von Blanckenburg and Bouchez, 2014). In the oceans, riverine input is the dominant source for ^{9}Be, while the river-derived ^{10}Be is negligible compared to its direct deposition from the atmosphere. The average residence time of Be in seawater is found to be ca. 600 – 1000 yrs, and the distinctly different sources of these two isotopes lead to distinct ^{10}Be/^{9}Be ratios between coastal seawater and open ocean, and between ocean basins (Bourlès et al., 1989a; Brown et al., 1992b; Frank et al., 2009; Kong et al., 2021b; Ku et al., 1990; Kusakabe et al., 1987; Measures et al., 1996; von Blanckenburg and Igel, 1999). This makes the ^{10}Be /^{9}Be ratio in seawater a sensitive tracer for intra-oceanic processes, such as water mass mixing (Frank et al., 2009; Frank et al., 2002) and ocean circulation (Ku et al., 1990; Kusakabe et al., 1987; von Blanckenburg et al., 1996).

Nevertheless, applications of the ^{10}Be /^{9}Be ratio in seawater are still very limited due to analytical difficulties. These arise from the extremely low concentrations of beryllium in seawater relative to extremely high concentrations of the seawater matrix that mainly comprises Na, Mg, K, and Ca in >10,000 µg/g concentration ranges. Concentrations of ^{9}Be ([^{9}Be], square brackets denote concentrations), however are typically only 0.03 – 0.54 pg/g (3 – 60 pmol/kg) in the open ocean (Ku et al., 1990; Kusakabe et al., 1987; Measures and Edmond, 1982; Measures and Edmond, 1983; Measures et al., 1996). Lowest ^{9}Be concentrations (ca. 0.03 pg/g) are found in surface waters from the western equatorial Pacific region (Xu, 1994). In estuaries, [^{9}Be] can reach values of ~9 pg/g (1 nmol/kg), due to the high riverine contribution (Brown et al., 1992b; Measures and Edmond, 1983). For the rare cosmogenic isotope ^{10}Be, a typical concentration range in open ocean water is 300 to 2000 atoms/g (Frank et al., 2009; Ku et al., 1990; Kusakabe et al., 1987; Measures et al., 1996). For coastal seawater, published [^{10}Be] data are limited to four sites: the San Francisco Bay (Kusakabe et al., 1991), the East China Sea (Yang et al., 2003), the northern South China Sea (Kong et al., 2021b), and the Pearl River Estuary (Kong et al., 2021a) where ^{10}Be concentration ranges are 60 to 1000 atoms/g. Precise measurements of such low Be concentrations thus require methods that enable the preconcentration of Be, that is, the separation of Be from the seawater matrix and its concentration into a small volume (i.e., a few mL), from easily collectible volumes of a few L.

Over the past few decades, preconcentration procedures have been routinely carried out separately for ^{9}Be and ^{10}Be for water samples (Frank et al., 2009; Kong et al., 2021b; Kusakabe et al., 1987; Measures and Edmond, 1982), i.e., by splitting the original water sample into ^{9}Be

and ^{10}Be aliquots prior to sample preconcentration (hereafter called the "conventional" procedure). A ^{9}Be carrier is then added to the ^{10}Be split before preconcentration, which is required for accelerator mass spectrometry (AMS) measurements of a ^{10}Be/^{9}Be$_{carrier}$ ratio. From the known amount of ^{9}Be$_{carrier}$, the unknown amount of ^{10}Be in the sample can be calculated, because the amount of ^{9}Be added by the carrier is much larger than the natural ^{9}Be present in the water sample. In this way, the recovery of ^{10}Be along the preconcentration steps can be accurately monitored. The most routinely used method for ^{10}Be preconcentration is the iron co-precipitation method, for which a large volume of seawater of approximately 20 L is typically required (Frank et al., 2009; Kong et al., 2021a; Kong et al., 2021b; Kusakabe et al., 1987). For ^{9}Be, a variety of methods have been employed, including hydroxide co-precipitation (Hiraide et al., 1994), liquid-liquid extraction (Bashir and Paull, 2001; Measures and Edmond, 1986), micelle-mediated extraction (Afkhami et al., 2007; Beiraghi and Babaee, 2008), and solid-phase extraction (SPE) (Amin, 2001; Tazoe et al., 2014; Yousefi et al., 2010). Employed ^{9}Be sample volumes vary from 0.1 to 1 L. Although preconcentrating ^{9}Be and ^{10}Be separately yields a more reliable ^{10}Be concentration, it is time-consuming, and may introduce uncertainty in the natural ^{10}Be/^{9}Be ratio if Be recovery differs in each split, especially when different preconcentration methods are applied for ^{9}Be and ^{10}Be, respectively.

In this study, we developed a new, time-efficient procedure (hereafter called the "simplified" procedure) to preconcentrate ^{9}Be and ^{10}Be simultaneously using the iron co-precipitation method. We tested this new procedure on a set of natural samples from the Changjiang Estuary that were also analysed following the conventional procedure. We supplement this new development with several validations of the iron co-precipitation method for Be extraction from seawater that have not been conducted previously: We tested i) the potential "matrix effect" on Be analysis using a sector-field high-resolution inductively coupled plasma-mass spectrometer (HR-ICP-MS), and ii) its extraction efficiency of different pg/g-levels Be in the presence and absence of organic matter, both using artificial seawater, and iii) the data comparability with another entirely different preconcentration method using natural Amazon Estuary water samples. Finally, we estimated the minimum water volume required for precise ^{9}Be and ^{10}Be determination based on the current techniques and methods employed, with the aim to provide references for future studies.

2.2 Materials and procedures

2.2.1 Reagents

All reagents were used as supplied and checked for possible ^{9}Be contamination. Concentrated HNO_3 and HCl used in this study were purified by sub-boiling analytical grade acids (Merck, Germany) and then diluted to the required molarity using ultrapure water (18.2 MΩ·cm, Milli-Q, Merck Millipore, Germany). The ammonia (25% w/w, Merck, Germany) used is analytical

grade. The $FeCl_3$ solution was prepared by dissolving iron(III)chloride hexahydrate (VMR chemicals, Germany) in 1M HCl. A 0.4M oxalic acid solution was prepared by dissolving solids (BioUltra, Sigma-Aldrich, Germany) in Milli-Q water. Beryllium-9 concentrations in all reagents were checked to be under the detection limit. A ^{9}Be carrier solution with a concentration of 780 μg/g, prepared from a phenakite mineral obtained from a deep mine (von Blanckenburg et al., 2016), was used to prepare standards for external calibration for the determination of [^{9}Be].

2.2.2 Preparation of artificial seawater

For artificial seawater preparation, we added roughly 33.33 g synthetic salt (Dupla Marin Premium Reef Salt Natural Balance, product code DM81432_MA) into 1 L Milli-Q water. This mixture mimics the natural composition of seawater and was used as the mother solution in the matrix effect test as well as for the recovery and DOC (dissolved organic carbon) tests.

2.2.3 Sampling of natural seawater

In the Changjiang (Yangtze) Estuary, five natural coastal seawater samples were taken along a salinity transect from 0 to 32.0 practical salinity units (PSU) during the KECES (Key Elements Cycling in the Changjiang-Estuary-Shelf Transect, August to September 2019) cruise. All samples were collected approximately 3-4 m upstream from the ship's bow via a pre-cleaned Masterflex I/P® Precision Pump tubing (C-Flex®) attached to the front end of a carbon fibre pole sampler, and water was pumped by a peristaltic pump. After collection, samples were immediately filtered through an acid-cleaned 0.45 μm filter (Supor® PES, Pall). The filtrates were stored in pre-cleaned LDPE bottles (Nalgene), acidified to pH < 2 with trace metal grade HCl, and stored at 4 °C until analysis.

Nine natural coastal seawater samples were collected from the Amazon Estuary during R/V Meteor Cruise M147 (Amazon-GEOTRACES, May 2018). The samples were collected along a salinity transect from 0 to 35.5 PSU using Niskin bottles attached to a rosette equipped with a CTD sensor (conductivity-temperature-depth). After collection, samples were filtered within a few hours through 0.45 μm filters (Nucleopore) and acidified to pH ~2 with concentrated ultrapure HCl. Samples were stored at room temperature prior to analysis. One sample at station M147_55-F (salinity of 35.5 PSU) was taken with a towed fish but otherwise treated the same way.

2.2.4 Preconcentration of ^{9}Be and ^{10}Be

2.2.4.1 Simplified procedure

The iron co-precipitation method was employed for the simultaneous preconcentration of ^{9}Be and ^{10}Be (as illustrated in Fig. 2.1a) for water samples. The volume of water required to measure

^{9}Be and ^{10}Be will depend on each isotope´s concentration (see discussion later), which varies in the (coastal) oceans. In this study, only around 600 g water were used due to limited available sample volume. In a first step, about 6 mL $FeCl_3$ solution (2 mg Fe/mL) was added to the sample (i.e., 20 mg Fe/L seawater). In step 2, after equilibration for >12 h, the pH was adjusted to 7.5-8.2 (measured by pH indicator paper PEHANON® with a measuring range of 7.2–8.8) using diluted (~12.5%) aqueous ammonia. To allow the homogenisation and precipitation of Fe-hydroxide, the sample was shaken several times and then left standing overnight. In a third step, the precipitate containing Be was separated from the liquid by centrifugation at 4000 rpm for 15 min and rinsed 3 times with pH 8-adjusted water. Note that for large volume samples (i.e., >2 L), we suggest to let the formed precipitate settle by gravity for 2-3 days. The upper supernatant can be gently decanted and the remaining lower supernatant is centrifuged to separate the precipitates. In a fourth step, the precipitate was oxidized overnight in 4 mL of aqua regia at 160 ℃. After evaporation and re-dissolving in 4 mL 6M HCl, step 5 of the procedure employs the separation of Fe from Be using a 20 mL column filled with 5 mL Bio-Rad AG® 1-X8 (100-200 mesh) anion exchange resin following established anion column chemistry routines (detailed steps can be found in the supplement). The Be was collected in 10 mL 6M HCl, evaporated to dryness and re-dissolved in 6 mL 3M HNO_3. Step 6 employs the splitting of this solution, where a 1 mL aliquot of the solution (1/6 of the solution) was gravimetrically separated and evaporated, then re-dissolved in 1 mL 3% HNO_3, and spiked with 1 ng/g Rhodium (Rh) as internal standard for ^{9}Be analysis. The concentration factor (i.e., the ratio of the sample's initial volume to the volume of analyte for measurement) was approximately 100 times. In step 7, the remaining 5 mL (5/6 of the solution) were spiked with 0.15 mg ^{9}Be carrier and prepared for ^{10}Be determination on the AMS. This entails evaporation and re-dissolving in 10 mL 1M HNO_3, followed by alkaline precipitation, that is, another pH adjustment to 9-10 by adding around 2.5 mL diluted aqueous ammonia (roughly 0.22-0.25 mL ammonia to each mL 1M HNO_3). After shaking, the centrifuge tube was placed in a warming bath at 65℃ for 1 hour to allow the precipitation of $Be(OH)_2$. The Be hydroxide precipitate was separated by centrifugation at 4000 rpm for 5 min. After discarding the supernatant, the precipitate was re-dissolved in 5 mL 1M HNO_3 and the alkaline precipitation was repeated once. The final collected Be precipitate was rinsed two times by pH 9-adjusted water and re-dissolved in 0.4 mL $AgNO_3$ solution containing 3.64 mg Ag. The solution was transferred into a quartz crucible and dried down on the hotplate at ~110°C, followed by oxidation to BeO and AMS target preparation, for ^{10}Be determination.

2.2.4.2 Conventional procedure

In the conventional procedure (Fig. 2.1b), the seawater samples were first gravimetrically separated into splits of ca. 180 g and 600 g each for ^{9}Be and ^{10}Be preconcentration. Note that the total sample volume employed in this procedure is slightly larger than in the simplified procedure, with the aim to derive more precise values as a benchmark for assessing the reliability of the new, simplified procedure. After adding the ^{9}Be carrier to the ^{10}Be split, both

splits were processed individually as described above, i.e., addition of $FeCl_3$, pH-dependent Fe-hydroxide precipitation, centrifugation of the precipitate, and anion column chemistry, followed by ^{9}Be and ^{10}Be determination using HR-ICP-MS and AMS, respectively.

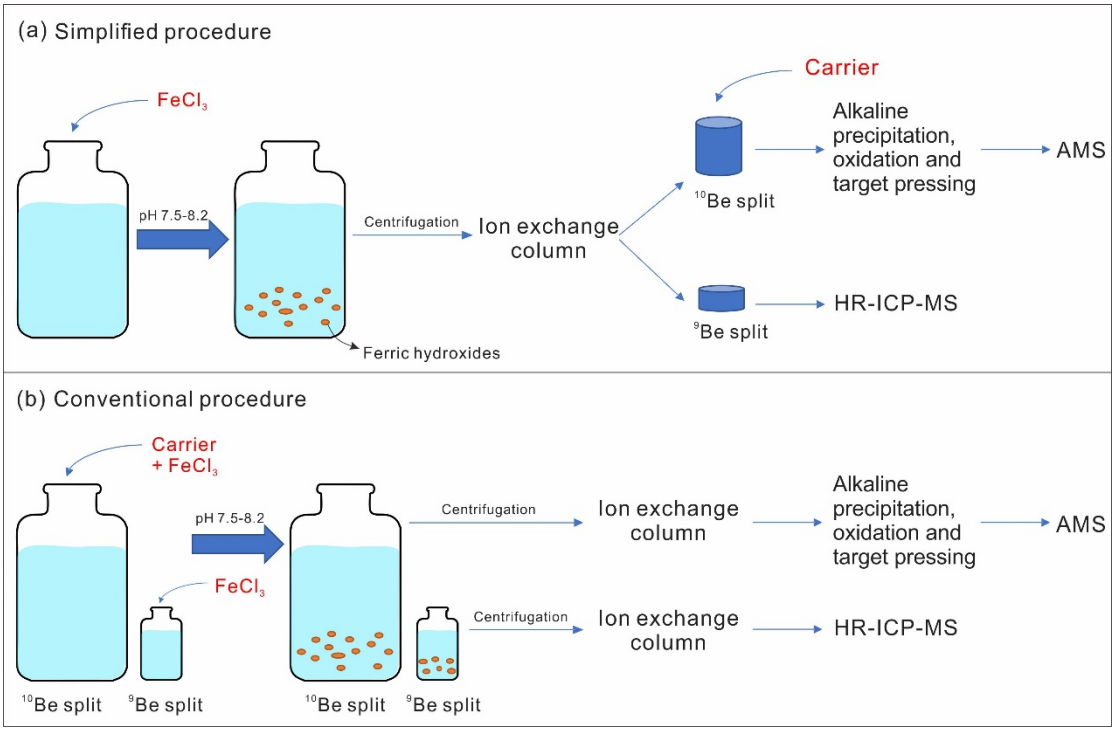

Figure 2.1 Simplified scheme for the "simplified" (a) and the "conventional" (b) procedures for preconcentrating ^{9}Be and ^{10}Be from seawater using the iron co-precipitation method. The "ion exchange column" is a Biorad AG 1-X8 anion exchange column used for separating Fe from Be.

2.2.5 Instrumentation

The ^{9}Be was determined on HR-ICP-MS (Element2, Thermo Fisher Scientific) operated in low-resolution mode. Typical instrument operating conditions are shown in Table S2.1. Under these conditions, the doubly charged ion rate was less than 3% and the oxide rate was less than 5%. Rh was used as an internal standard and Be was quantified by an external calibration with standards prepared gravimetrically from our in-house carrier solution.

Beryllium-10 concentrations were obtained from AMS measurements of $^{10}Be/^{9}Be_{carrier}$ ratios at University of Cologne, relative to the standards KN01-6-2 and KN01-5-3 with a $^{10}Be/^{9}Be$ ratio of 5.35×10^{-13} and 6.32×10^{-12}, respectively (Dewald et al., 2013).

The Na, Mg, K and Ca concentrations remaining in solutions after preconcentration were determined by an optical emission inductively-coupled plasma spectrometer (ICP-OES, Varian 720-ES with axial optics) using the 589.592, 280.270, 766.491 and 422.673 nm wavelengths, respectively, and quantified by an external calibration prepared from single element standards.

2.2.6 Experimental setup for iron co-precipitation method validation

2.2.6.1 Matrix effect test

To test the potential matrix effects on HR-ICP-MS analysis from the cations remaining in the precipitate after iron co-precipitation, we first checked the major cation composition of the precipitate obtained after the iron co-precipitation. Four artificial seawater samples (~100 g each) were split from the same mother solution and treated according to the preconcentration procedure steps 1 to 6 described above. An aliquot of around 50 µL was gravimetrically pipetted out of the HR-ICP-MS split (step 6) and diluted to 4 mL using 0.3 M HNO_3 doped with 1000 µg/g Cs for the measurement of the remaining major cations using ICP-OES and an external calibration. In a second approach, we employed the standard addition method (see supplement) to check if remaining cations affect the accuracy of the HR-ICP-MS measurements. Two artificial seawater samples (~100 g each) were separated from the same artificial seawater mother solution. After step 6 of the iron co-precipitation procedure, [^{9}Be] was determined from one sample directly (using an external calibration), whereas the other sample was further separated equally into 4 aliquots, spiked with ~0, 50, 100, and 150 pg/g of Be, respectively, and quantified by standard addition.

2.2.6.2 Recovery in the presence and absence of DOC

Since no certified water standard is available for ^{10}Be and AMS analysis is costly and time-consuming, we carried out a recovery test in the presence and absence of DOC using ^{9}Be-spiked artificial seawater, with the aim to evaluate the effect of DOC on Be recovery during the iron co-precipitation method. We assume that our test results are equally valid for ^{10}Be, given the identical geochemical behaviour of ^{9}Be and ^{10}Be and their negligible isotope fractionation during co-precipitation. Although additional procedures are required for ^{10}Be determination after the iron co-precipitation, any potential loss of the ^{10}Be thereafter can be controlled by the addition of a ^{9}Be carrier.

A set of artificial seawater samples (each ~100 g) were split from the mother solution of artificial seawater and spiked with ascending Be concentrations, i.e., 0, 5, 10, 20 pg/g. The unspiked sample was used to monitor Be background levels in the mother solution (see supplement). Procedural blanks using ~100 g Milli-Q water were also processed. Additionally, a set of duplicate Be-spiked samples were supplied with 0.2 g of 0.4 M oxalic acid, resulting in a DOC concentration of 160 µM to mimic the maximum value for open ocean and most coastal seawater (Barrón and Duarte, 2015; Hansell et al., 2009).

The Be recovery (%) was calculated by subtracting the Be concentration of the unspiked sample from the measured concentrations of spiked samples and compared them with the added Be concentration (data are shown in Table S2.2). Subtraction of the unspiked sample resulted from

finding non-negligible amounts of ^{9}Be already present in the salt used to prepare the mother solution (see supplement).

2.2.6.3 Data comparability test

To further benchmark the iron co-precipitation method against previously employed methods, we applied the iron co-precipitation method to natural coastal seawater samples collected along a salinity gradient in the Amazon Estuary and compared our data to previously published data determined by electron capture detection gas chromatography after the liquid-liquid extraction.

2.3 Assessment and discussion

2.3.1 Matrix effect

An essential purpose of the preconcentration process is to remove the high seawater matrix prior to analysis. The HR-ICP-MS measurement for ^{9}Be has been considered highly sensitive to matrix effects (Horlick, 1987; Kawaguchi et al., 1987). First, Be is particularly sensitive to space-charge effects as low-mass elements are more affected than heavier mass elements, causing a loss of sensitivity (Archuleta and Duran, 2009). Second, the matrix may affect the sample transport and ionisation efficiency into the plasma and thus suppress the signal of the analyte (Archuleta and Duran, 2009).

The composition of the remaining matrix (mainly Na, Mg, K and Ca) in the analytes (1 mL 3% HNO_3 spiked with 1 ng/g Rh, step 6 in the iron co-precipitation procedure) is shown in Table 2.1. Mean concentration values found for Na, Mg and Ca were around 6, 31 and 38 µg/g, respectively, while the K concentration is below detection limit. Considering a concentration factor of about 100, this indicates that more than 99% of the initial seawater matrix was removed during the iron co-precipitation procedure.

By means of standard addition, we examined whether these µg/g-levels of matrix remaining in solution after preconcentration will affect the analysis of ^{9}Be by HR-ICP-MS. The ^{9}Be concentration in an artificial seawater sample obtained using standard addition is 2.72 ± 0.18 pg/g (see details in the supplement), which is in good agreement with the directly measured value of 2.93 ± 0.08 pg/g using an external calibration. This indicates that the remaining matrix in solution after iron co-precipitation does not affect the ^{9}Be determination via HR-ICP-MS.

Table 2.1 Concentrations of Na, Mg, K and Ca in artificial seawater samples before and after the iron co-precipitation

		Na (µg/g)	Mg (µg/g)	K (µg/g)	Ca (µg/g)
Initial concentration		11000	1300	390	420
Sample ID	Initial seawater weight (g)				
AFSW _1	100.4	n.d.	36	n.d.	33
AFSW _2	100.1	2	35	n.d.	43
AFSW _3	100.1	1	27	n.d.	38
AFSW _4	100.3	21	27	0.3	39

The initial concentrations of Na, Mg, K and Ca are theoretical concentrations derived from the ingredients of the synthetic salt mixture.
The concentrations of Na, Mg, K and Ca in artificial seawater (AFSW) samples are measured concentrations in analytes after preconcentration, the concentration factors are about 100 times. For ICP-OES measurements, a 5% uncertainty is given that represents the long-term repeatability.
n.d. = Measured value is lower than the detection limit.

2.3.2 Be recovery and effects of DOC

Across a pH range of 6 to 9, the majority of Be exists as hydrolysed species when humic acid is absent. However, in the presence of humic acid, Be is instead found to be speciated as Be-humate (Takahashi et al., 1999; Willenbring and von Blanckenburg, 2010). Based on mixing experiments, Suhrhoff et al. (2019) proposed that DOC may stabilize Be in the dissolved phase, thus the Be-humate complexes are more resistant to colloidal flocculation during estuarine mixing. Therefore, it is likely that the alteration of aqueous Be species may influence the behaviour of Be during the co-precipitation process, resulting in reduced recovery efficiency. Reduced Be recovery (~ 30%) has been reported after adding 1600 µM (ca. 20 mg/L) DOC to river water (Wittmann et al., 2015). However, a typical DOC concentration range is 34 - ~80 µM (0.4 - ~1 mg/L) for open ocean seawater (Hansell et al., 2009) and 40 - >700 µM (0.5 - >8 mg/L) in coastal water (Barrón and Duarte, 2015). In our experiment we thus added 160 µM (ca. 2 mg/L) DOC, which comprises a maximum value for open ocean and most coastal seawater.

Resulting mean recovery for the Be concentration range between 5 to 20 pg/g in the absence of DOC is 100.8 ± 5.7 % (1SD, N = 8) (Fig. 2.2). This recovery does not depend on the spiked Be concentration and is comparable to previously reported values (Suhrhoff et al., 2019; Tazoe et

al., 2014). Note, however, that Suhrhoff et al. (2019) used a single spiked Be concentration (i.e. 9 pg/g) and did not evaluate a Be concentration range. In the presence of DOC, the mean Be recovery is with 95.2 ± 3.9 % (1SD, N = 6) (Fig. 2.2) slightly lower, but nearly identical to that obtained in the absence of organics. We regard this somewhat lower recovery to be unproblematic, because i) this narrow range of ±5% is well within the range of commonly encountered uncertainties of such low-level analytics, and ii) a lower recovery will not affect the ratio of ^{10}Be to ^{9}Be, as both isotopes will be equally affected.

Overall, this assessment demonstrates that the Be recovery will not be affected by the presence of up to 160 µM of organic matter. This implies that for open ocean seawater and the majority of coastal seawater where DOC concentrations are below 160 µM, the iron co-precipitation method can be applied directly without a previous decomposition of organic matter. However, for water with much higher DOC concentrations, a lower Be recovery may be expected, and obtained single [^{10}Be] or [^{9}Be] may be treated with caution.

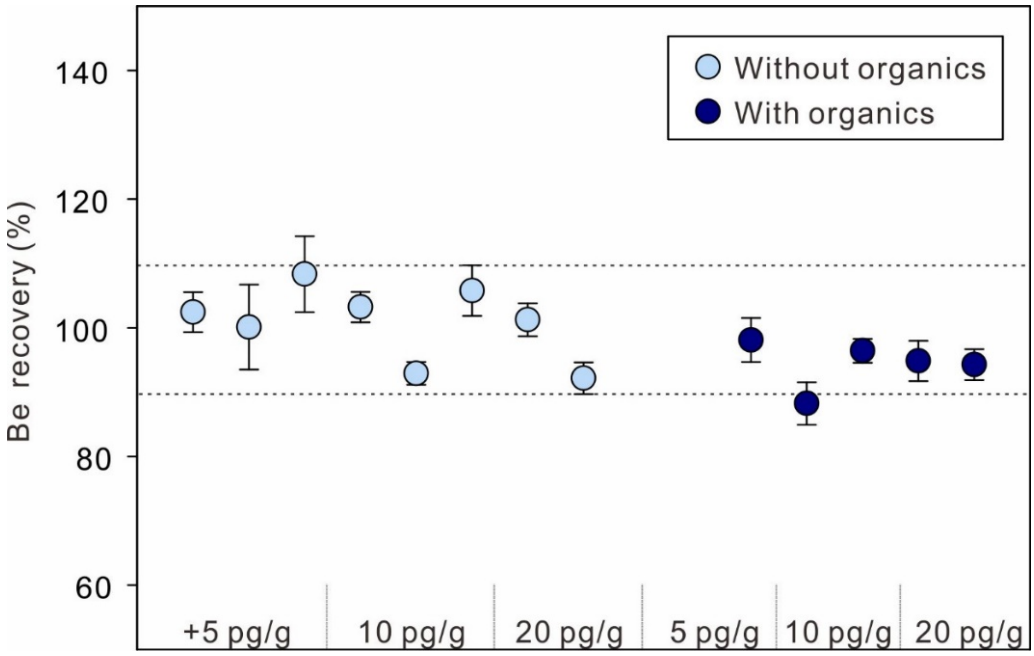

Figure 2.2 Long-term recovery of ^{9}Be from artificial seawater spiked with different ^{9}Be concentrations in the absence and presence of organic matter (simulating a seawater DOC concentration of 160 µM by addition of oxalic acid); Dashed lines represent recovery within 100 ± 10%.

2.3.3 Data comparability between the iron co-precipitation method and the liquid-liquid extraction method

Various preconcentration methods have been employed for ^{9}Be determination in seawater in previous studies, but the comparability of data derived from these methods still remains unclear. Dissolved ^{9}Be concentrations in the Amazon Estuary seawater (Fig. 2.3) obtained using the iron

co-precipitation method, show good agreement with previously published data (Fig. 2.3), both displaying an exponential decrease with salinity. The previous data obtained by Measures and Edmond (1983) and Brown et al. (1992) were both determined by electron capture detection gas chromatography after liquid-liquid extraction. This good agreement confirms the data comparability between the iron co-precipitation method (commonly employed to obtain ^{10}Be concentrations) and the liquid-liquid extraction method that is widely used to obtain ^{9}Be concentrations. This demonstrates that the iron co-precipitation method is suitable to generate comparable and oceanographically consistent Be data.

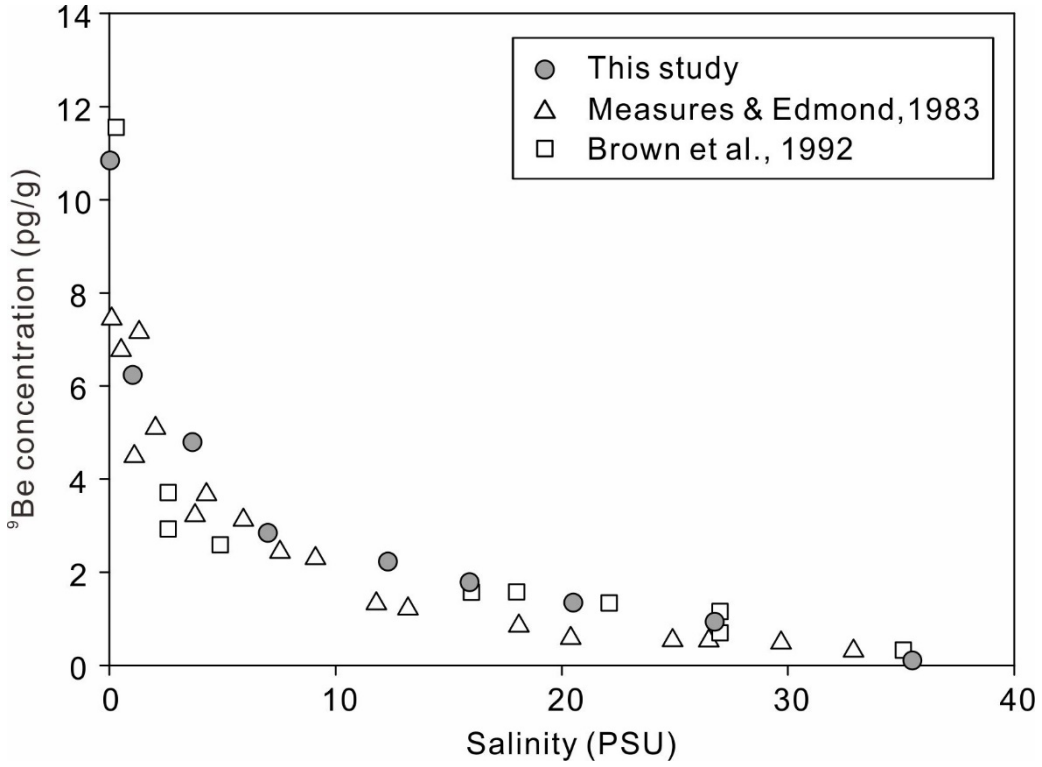

Figure 2.3 Dissolved ^{9}Be concentrations (in pg/g) in the Amazon Estuary along a salinity transect from 0 to 35.5 PSU. Error bars for this study are smaller than the symbol size, and not available for published studies. Samples from Brown et al. (1992) were collected during the AMASEDS Expedition in August 1989.

2.3.4 Application of the simplified procedure to natural coastal seawater

After validation of the ion co-precipitation method, we next employ it to determine the ^{10}Be/^{9}Be ratio in 5 coastal seawaters collected from the Changjiang Estuary, following the new simplified procedure (Fig. 2.1a). To provide a benchmark, we also measured the same samples following the conventional procedure (Fig. 2.1b). Compared to the conventional procedure, the simplified procedure has the following advantages: i) *Improved time-efficiency*. The co-precipitation and the subsequent column chemistry routines only need to be performed once, as compared to twice in the conventional procedure. ii) *Reduced cross-contamination.* In the conventional procedure, the ^{9}Be carrier that has a much higher ^{9}Be concentration than natural seawater is

added to the ^{10}Be split before the preconcentration (Fig. 2.1b) and hence may contaminate the ^{9}Be split by any accidental or mixed-use of the laboratory consumables (e.g., beakers, columns) that are employed for ^{9}Be and ^{10}Be preconcentration, respectively. This risk can be reduced by employing the simplified procedure. iii) *Improved reliability of the ^{10}Be/^{9}Be ratio*. Preconcentrating ^{9}Be and ^{10}Be simultaneously can avoid any potential unproportionate loss of ^{9}Be and ^{10}Be during co-precipitation and the chromatographic steps, thus resulting in more reliable ^{10}Be/^{9}Be ratio. The only disadvantage of the simplified procedure is that the absolute value of [^{10}Be] can be potentially biased, given that the potential loss during the co-precipitation and the chromatographic steps cannot be controlled without having added the ^{9}Be carrier before. However, the results for [^{9}Be], [^{10}Be] and the resulting ^{10}Be/^{9}Be ratio of 5 coastal Changjiang seawater samples obtained from these two procedures (Fig. 2.1) agree well with each other (Table 2.2, Fig. 2.4). Except for one sample at close-to-zero salinity where the difference in [^{9}Be] amounts to 18% (Fig. 2.4a), nearly all variations are within the uncertainties (albeit in some cases large). The relatively large uncertainties in the ^{10}Be concentrations result from the extremely low concentrations in the samples and minimized sample volumes of only 500-600 g (see next section). The good agreement between data obtained by the two procedures indicates nevertheless high accuracy results from both procedures. It can be inferred that our simplified procedure is equally feasible for obtaining accurate concentrations of ^{9}Be and ^{10}Be and ^{10}Be/^{9}Be ratios, in comparison with the time-consuming conventional procedure. We therefore recommend this simplified procedure for future studies on Be isotopes in seawater, especially when only the ^{10}Be/^{9}Be ratio is of interest.

Table 2.2 Dissolved (diss) ^{9}Be and ^{10}Be concentrations and resulting ^{10}Be/^{9}Be ratios for 5 coastal seawater samples from the Changjiang Estuary following the conventional and the simplified preconcentration procedures.

		Conventional Procedure					Simplified procedure			
Sample ID	Salinity (PSU)	Initial seawater mass for ^{9}Be (g)	Initial seawater mass for ^{10}Be (g)	$[^{9}Be]_{diss}$ * (pg/g)	$[^{10}Be]_{diss}$ † (atoms/g)	$(^{10}Be/^{9}Be)_{diss}$‡ ($\times10^{-9}$)	Initial seawater mass for ^{9}Be and ^{10}Be (g)	$[^{9}Be]_{diss}$ * (pg/g)	$[^{10}Be]_{diss}$ † (atoms/g)	$(^{10}Be/^{9}Be)_{diss}$‡ ($\times10^{-9}$)
C1	0.1	182	610	1.30 ± 0.06 (4.2%)	195 ± 32 (16.4%)	2.24 ± 0.38	664	1.06 ± 0.04 (3.4%)	188 ± 36 (19.1%)	2.65 ± 0.51
C6-2	4.1	181	611	0.88 ± 0.03 (3.7%)	177 ± 35 (19.8%)	3.00 ± 0.61	600	0.83 ± 0.03 (3.6%)	227 ± 37 (16.3%)	4.10 ± 0.68
C6-3	9.3	179	620	0.96 ± 0.03 (3.4%)	235 ± 35 (14.9%)	3.66 ± 0.56	600	0.89 ± 0.04 (4.5%)	276 ± 38 (13.8%)	4.66 ± 0.67
C9	16.8	185	627	0.88 ± 0.09 (10.0%)	205 ± 35 (17.1%)	3.50 ± 0.61	601	0.85 ± 0.02 (2.4%)	196 ± 33 (16.8%)	3.45 ± 0.59
C18	32.0	194	599	0.27 ± 0.02 (5.2%)	149 ± 33 (22.1%)	8.28 ± 3.20	600	0.31 ± 0.04 (12.9%)	132 ± 32 (24.2%)	6.47 ± 1.79

* Uncertainty is the analytical uncertainty (1 SD) from HR-ICP-MS analysis in absolute and relative (%) numbers.

† Uncertainty contains analytical uncertainty (1 SD) from AMS measurement, and sample ratios were corrected using a mean long-term blank $(^{10}Be/^{9}Be)_{blk}$ ratio of 1.62 (± 1.07, 1 SD)$\times10^{-15}$ (N = 4).

‡ Uncertainty was propagated from the given [^{9}Be] and [^{10}Be] uncertainties.

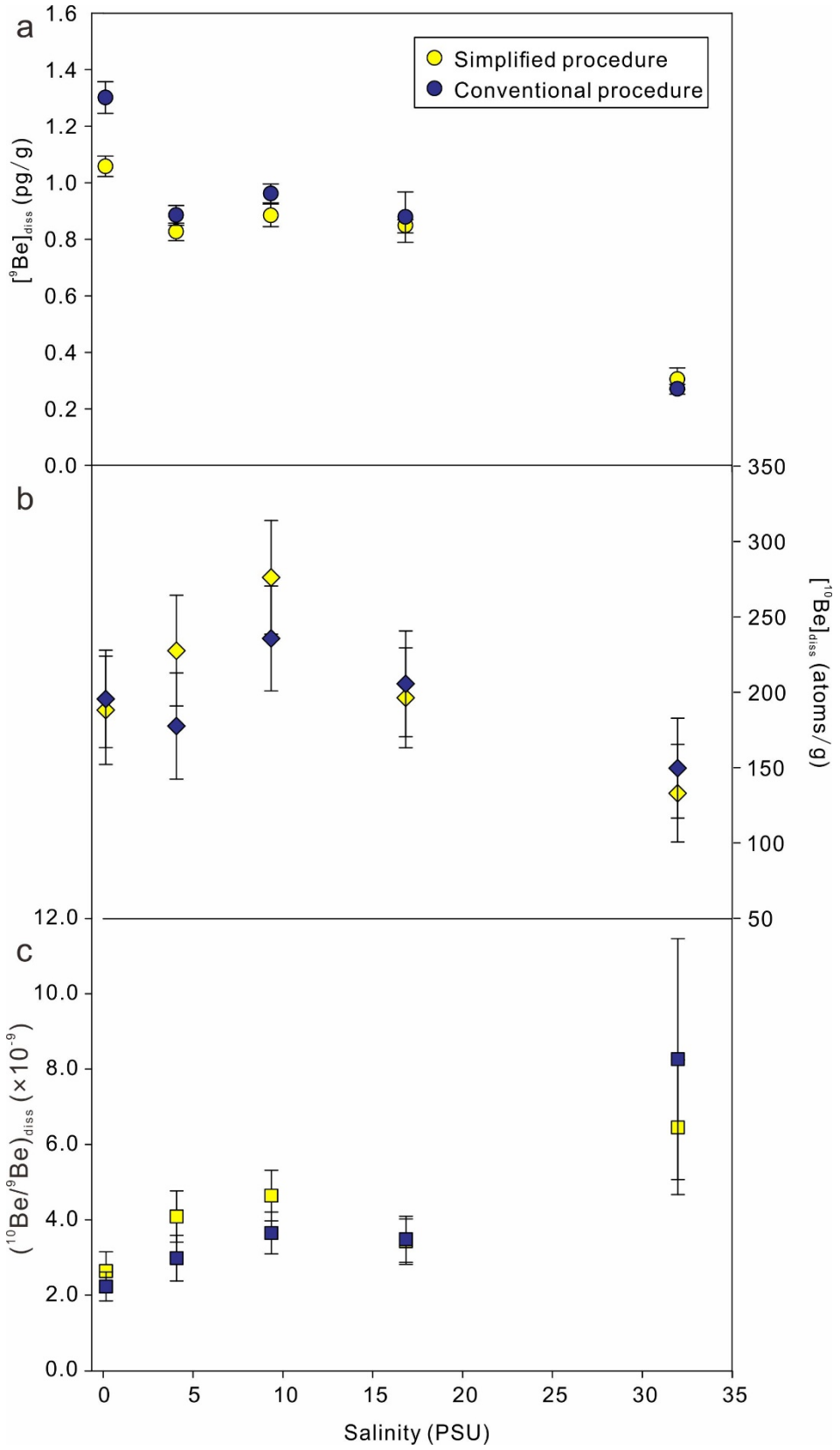

Figure 2.4 Comparison of dissolved [^{9}Be] (a), [^{10}Be] (b) and (^{10}Be/^{9}Be) (c) for 5 coastal seawater samples from the Changjiang Estuary along a salinity transect where ^{9}Be and ^{10}Be were preconcentrated following the conventional and the simplified procedures, respectively. Data are shown in Table 2.2.

2.3.5 Water sample volume required for ^{9}Be and ^{10}Be determination

Due to the extremely low concentrations of ^{9}Be and ^{10}Be in seawater as observed in the Changjiang Estuary, a large volume of sample is required for more accurate determination. Note that >20 L was routinely employed in former studies. However, sampling and processing of large volumes of seawater is time-consuming and labour-intensive. Hence, it is worthwhile to estimate a minimum volume for accurate determination before sampling or planning an experiment.

In this study, the detection limit (LOD) for ^{9}Be is 29.7 pg/g, calculated using the average procedural blank signal plus three times the standard deviation (N=14). Combining this LOD with the lowest ^{9}Be concentration of 0.027 pg/g so far reported for open ocean seawater (Xu, 1994), a sample volume of 1.1 L would allow to detect even lowest ^{9}Be concentrations in nearly all types of seawater samples. However, in order to achieve good precision and accuracy (i.e., relative standard deviation (RSD) <5%) of ^{9}Be determination, using a LOQ (Limit of Quantification, calculated using the average instrumental blank signal plus ten times the standard deviation, N=14) of 50.2 pg/g in this study would necessitate a sample volume of 1.8 L. When measured on estuarine water with a typical ^{9}Be concentration of > 0.13 pg/g) (Brown et al., 1992b; Kong et al., 2021a; Kusakabe et al., 1991; Measures and Edmond, 1983), a sample volume of <0.4 L would be sufficient for accurate ^{9}Be determination. The higher uncertainties (>5%) observed for sample C18 from the Changjiang Estuary (Table 2.2) are examples for failing to reach the LOQ due to the inadequate sample volume employed (0.19 L and 0.1 L used for the conventional and the simplified procedures, respectively). It is worth noting that the LOD and LOQ for ^{9}Be determination may vary greatly between different laboratories even if the same technique is employed, depending on the laboratory environment and instrument status. Therefore, measuring a series of blanks to define the LOD and LOQ should precede planning a sampling campaign.

For ^{10}Be, typical lower limits of the (^{10}Be/^{9}Be) ratio are 10^{-15} to 10^{-16} at most AMS facilities (Klein et al., 2011; Müller et al., 2008). However, the detection limit that matters is set by the laboratory procedural blanks which account for ^{10}Be contained in the carrier and possibly introduced during sample processing. To our best of knowledge this type of detection limit data has to date not been reported for the analysis of ^{10}Be in seawater samples. In this study we derived an average $(^{10}Be/^{9}Be)_{blk}$ value from 4 procedural blanks corresponding to 4 sample batches processed between May 2020 to October 2020. From this average $(^{10}Be/^{9}Be)_{blk}$ value of 1.62 (± 1.07, 1 SD)×10^{-15}, we calculated a "^{10}Be-LOD" of 4.83×10^{-15} and a "^{10}Be-LOQ" of 1.23×10^{-14}. The minimum seawater sample volume ($M_{seawater}$, in g) used for preconcentration required for AMS determination can be roughly calculated based on the following equation:

$$M_{seawater} = \frac{M_{carrier} \times \frac{N_A}{M_{^9Be}} \times ((\frac{^{10}Be}{^9Be})_{meas} - (\frac{^{10}Be}{^9Be})_{blk})}{[^{10}Be]} \quad (2.1)$$

where [^{10}Be] is the ^{10}Be concentration (atoms/g) in the sample, $M_{carrier}$ is the weight of added ^{9}Be carrier (g), N_A is Avogadro's number (1/mol), $M_{^9Be}$ is the molar weight of ^{9}Be (mol/g), $(^{10}Be/^9Be)_{meas}$ is the measured AMS (carrier) ratio of the sample and $(^{10}Be/^9Be)_{blk}$ is the mean AMS-derived blank ratio. A correction for natural ^{9}Be concentration is not necessary since the concentration of ^{9}Be in seawater is negligible compared to that of the ^{9}Be carrier.

Employing equation (2.1) and using our long-term mean $(^{10}Be/^9Be)_{blk}$ value of 1.62×10^{-15} and a $M_{carrier}$ of 0.16 mg (in accordance with the laboratory protocol), for seawater with a [^{10}Be] of 100 atoms/g (which denotes nearly the minimum concentration present in seawater), a minimum of 0.4 L of sample will be needed to achieve $(^{10}Be/^9Be)_{meas}$ to be higher than the ^{10}Be-LOD, but around 1L to meet the ^{10}Be-LOQ (Fig. 2.5). However, even if the ^{10}Be-LOQ is reached, the uncertainty calculated for the final [^{10}Be] is still significant (i.e., >10%), because it is not only derived from the analytical uncertainty of AMS-derived $(^{10}Be/^9Be)_{meas}$ (typically >10% when ^{10}Be counts are less than 100), but also propagated from the non-negligible uncertainty of the mean blank ratio. Our [^{10}Be] data obtained from the Changjiang Estuary exemplify such "minimum volume" conditions, resulting in high uncertainties (Table 2.2, and yellow and blue bars in Fig. 2.5). Means to reduce the uncertainty would be to either lower the procedural blank value to 10^{-16}, or to increase the sample volume. For example, to reduce the uncertainty of the Changjiang samples to <5%, a sample volume of around 4 to 10 L would be required (Fig. 2.5). For open ocean seawater with a typical ^{10}Be concentration of > 500 atoms/g, only around 2 L of sample would be sufficient to achieve a final uncertainty of <5%.

These calculations demonstrate that there is no need to collect more than 20 L of seawater for [^{9}Be] and [^{10}Be] determinations as done by previous studies, but that around 3 L (2 L for ^{10}Be and 1 L for ^{9}Be when following the conventional preconcentration procedure) of open ocean seawater and a maximum of 10 L (9.5 L for ^{10}Be and 0.5 L for ^{9}Be) for coastal seawater would be sufficient.

When following the simplified procedure, i.e., preconcentrating ^{9}Be and ^{10}Be from a single volume of water, the splitting strategy (step 6) after the iron co-precipitation should be based on the relative estimated sample volumes required for accurate ^{9}Be and ^{10}Be determinations. For example, if 3 L (2 L for ^{10}Be and 1 L for ^{9}Be) of open ocean seawater would be needed, splitting the solution after anion exchange column should be in proportion of 2:1 (2/3 for ^{10}Be and 1/3 for ^{9}Be determination, respectively).

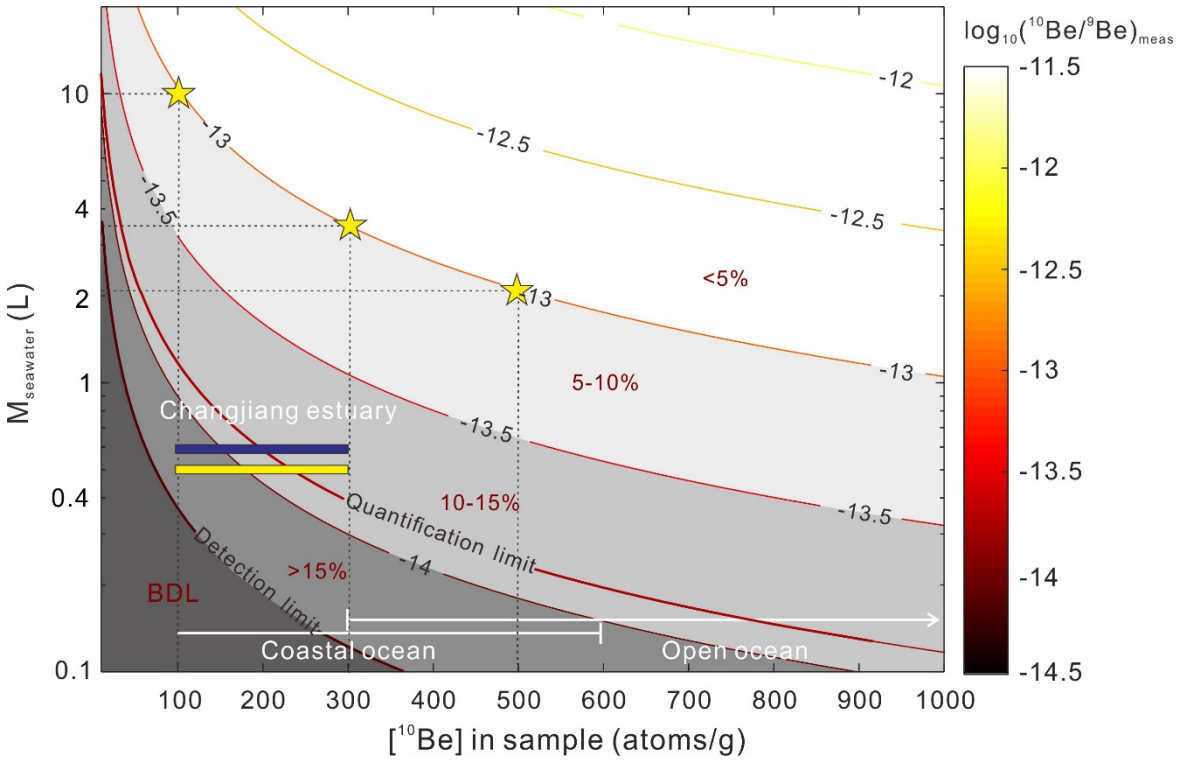

Figure 2.5 Visualization of equation (2.1) calculated using the long-term mean blank ratio ($^{10}Be/^{9}Be)_{blk}$ = 1.62 (± 1.1, 1 SD)×10^{-15} atoms/atoms and $M_{carrier}$ = 0.16 mg (see text). Towards the lower left side, uncertainties (%) of calculated [^{10}Be] propagated from the blank ratio- and empirical analytical AMS-related uncertainties increase, as indicated by the red numbers. The quantification limit (LOQ) in this case is 1.2×10^{-14} atoms/atoms, and the detection limit (LOD) is 4.8×10^{-15} atoms/atoms, with "BDL" (below detection limit) indicating ranges not detectable. The blue and yellow bars indicate the data range we obtained from the Changjiang Estuary when around 0.6 L (blue) and 0.5 L (yellow) of seawater were processed following the conventional and simplified procedures, respectively. The yellow stars indicate the water volumes required to yield accurate ^{10}Be concentrations for the Changjiang Estuary seawater and open ocean seawater with a [^{10}Be] of 500 atoms/g. The white segments below represent the typical range of [^{10}Be] in coastal and open ocean seawater.

2.4 Comments and recommendations

The iron co-precipitation method is a robust preconcentration procedure capable of quantitatively recovering ultra low-level Be from open ocean and most coastal seawater (dissolved organic carbon levels lower than 160 μM) in the range of a few pg/g. We show that 1) the matrix effect for HR-ICP-MS determination from remaining cations after the iron co-precipitation is negligible; and 2) data derived from the iron co-precipitation method is comparable with those derived from the liquid-liquid extraction method. Our new procedure based on the iron co-precipitation method to preconcentrate ^{9}Be and ^{10}Be simultaneously from seawater is found to be equally feasible for obtaining accurate concentrations of ^{9}Be and ^{10}Be

and $^{10}Be/^{9}Be$ ratios in comparison with the conventional procedure where ^{9}Be and ^{10}Be require separate preconcentration. We recommend this simplified procedure for future analysis on $^{10}Be/^{9}Be$ ratios in the ocean, as it saves time and avoids potential sample cross-contamination and unproportionate loss of ^{9}Be and ^{10}Be during separate preconcentration. We also provide means to estimate the required minimum sample volume for precise ^{9}Be and ^{10}Be determinations before sampling or planning an experiment. If an approximate concentration range of ^{9}Be and ^{10}Be in the sample is unknown, we recommend to use about 3 L and 10 L of water volume for open ocean seawater and coastal seawater, respectively.

2.5 Supplementary material

2.5.1 Chromatography

After obtaining the iron precipitates, the Fe is separated from Be using a 20 mL column filled with 5 mL Bio-Rad AG® 1-X8 (100-200 mesh) anion exchange resin according to the following procedure.

Open column and let Milli-Q water drop out		
5 + 5 mL	0.3M HCl	clean resin
3 + 3 mL	6M HCl	condition resin
Load sample (in 4 mL 6M HCl)		collect Be in pre-cleaned beaker
3 + 3 mL	6M HCl	collect Be in pre-cleaned beaker
5 + 5 mL	0.3M HCl	clean resin
5 mL	Milli-Q water	wash HCl from column
Seal and store column in Milli-Q water		

2.5.2 HR-ICP-MS instrumentation

The operating conditions for the sector-field high-resolution inductively coupled plasma-mass spectrometer (HR-ICP-MS, Element2, Thermo Fisher Scientific) for ^{9}Be analysis are shown in Table S2.1.

Table S2.1 HR-ICP-MS instrumentation and operating conditions

Instrumentation	Setting
Element 2 ™ (HR-ICP-MS)	
RF power	1350W
Cool gas	15.5 L min^{-1}
Auxiliary gas	0.74 L min^{-1}
Sample gas	1.104 L min^{-1}
Peristaltic pump speed	5.00 rpm
Nebulizer	PFA-ST 100 uL/min
Spray chamber	Cyclonic
Sampler cone	Ni N
Skimmer cone	Ni H

2.5.3 [^{9}Be] in artificial seawater calculated by standard addition

Based on the standard addition curve (Fig S2.1), the [^{9}Be] in the analyte is calculated to be 2.72 ± 0.18 pg/g, i.e., the intercept of the x-axis.

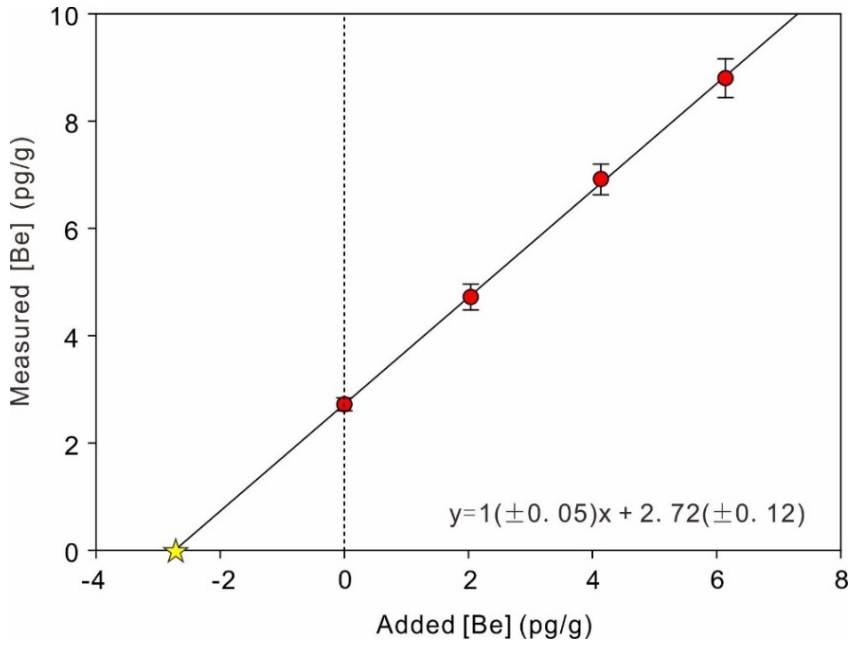

Figure S2.1 Standard addition curves for an artificial seawater sample preconcentrated by the iron co-precipitation method. The uncertainties of slope and y-intercept were calculated by propagating analytical (2% -5%) and balance-related weighting errors (0.6% - 2%) using IsoplotR.

2.5.4 Be recovery calculation

We used the respective "0 pg/g-Be" value derived from each batch and subtracted this value from the measured value of spiked samples when calculating the recovery. This subtraction was conducted because the measured concentration of the unspiked (i.e, 0 pg/g Be-spiked) samples, that is, the background concentration of Be in the artificial seawater, varied between each batch, ranging from 2.95 to 3.75 pg/g (i.e. accounting for a concentration factor of ~100, Tables S2.2). These Be background concentrations exceed Be concentrations in natural seawater (e.g. ranging from 0.03 to 0.54 pg/g in the open ocean). As the procedural (Milli-Q) blanks were always below the instrumental detection limit, such high Be background concentrations can only stem from the seawater salt added. Importantly, when derived from the same mother solution, good reproducibility was observed for Be background concentrations in the unspiked samples (circled values in Fig. S2.2). For 5 unspiked samples preconcentrated using the iron co-precipitation method within a 2-month period, we obtained a long-term reproducibility of 4.8% (relative standard deviation, RSD), deriving a mean Be background value of 3.32 pg/g (Fig. S2.2). It is very likely that the salt used for producing the artificial seawater was heterogeneous with respect to Be, explaining the large variation in Be background concentrations obtained

from different mother solutions. To avoid such inter-batch background variations in future research, we suggest to prepare a volume of artificial seawater mother solution sufficient for all sets of experiments.

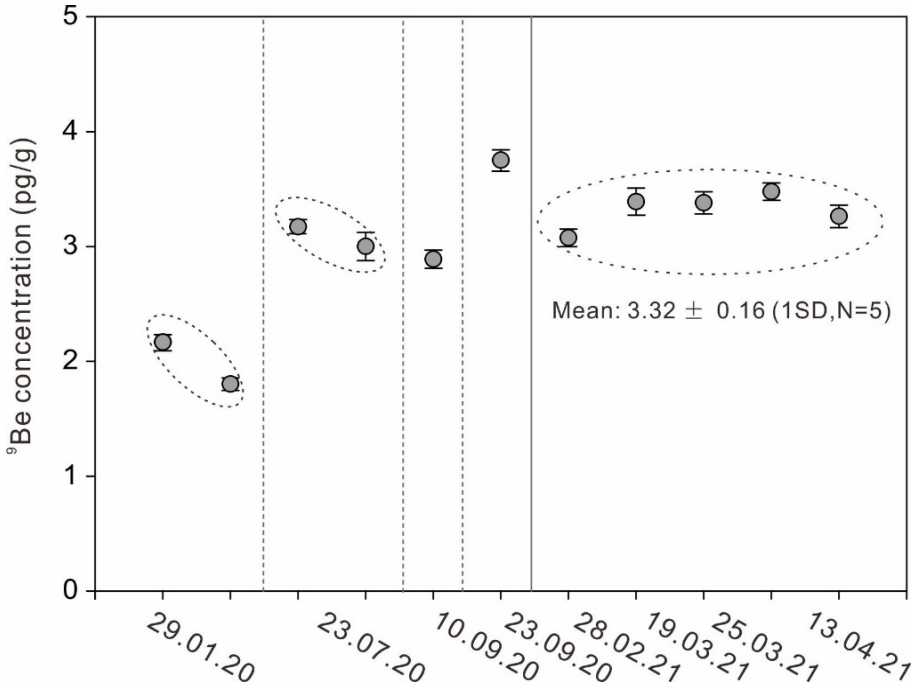

Figure S2.2 Long-term Be background values of artificial seawater in different batches. Data in each dashed circle are derived from the same mother solution.

Table S2.2 Artificial seawater samples employed for recovery test of the iron co-precipitation method

Preparation Date	Sample ID*	Initial seawater mass (g)	Be added (pg/g)	Be found (pg/g) †	Recovery (%)‡
Batch 1 29.01.2020	AFSW_0ppt	101.7	0.00	2.95 ± 0.09 (3.1%)	--
	AFSW_5ppt	100.3	4.99	7.98 ± 0.32 (3.9%)	100.2 ± 6.6
	AFSW_10ppt	103.5	9.73	12.02 ± 0.15 (1.2%)	93.0 ± 1.8
	AFSW_20ppt	101.0	19.96	21.38 ± 0.48 (2.2%)	92.2 ± 2.5
	AFSW_5ppt_org	102.4	4.90	7.79 ± 0.14 (1.7%)	98.1 ± 3.4
	AFSW_10ppt_ org	101.8	9.91	12.54 ± 0.15 (1.2%)	96.5 ± 1.9
	AFSW_20ppt_ org	103.3	19.50	21.37 ± 0.46 (2.1%)	94.3 ± 2.4
Batch 2 23.07.2020	AFSW _0ppt	104.8	0.00	3.20 ± 0.07 (2.0%)	--
	AFSW_5ppt	105.3	5.12	8.45 ± 0.19 (2.3%)	102.5 ± 3.1
	AFSW_10ppt	102.5	10.48	14.03 ± 0.15 (1.1%)	103.3 ± 2.4
	AFSW_20ppt	101.1	21.32	24.80 ± 0.37 (1.5%)	101.3± 2.6
	AFSW_5ppt_ org §	98.5	5.50	8.66 ± 5.72 (66%)	99.1 ± 65.5
	AFSW_10ppt_ org	101.7	10.60	12.57 ± 0.40 (3.1%)	88.3 ± 3.3
	AFSW _20ppt_ org	108.7	19.79	21.98 ± 0.58 (2.6%)	94.9 ± 3.1
Batch 3 23.09.2020	AFSW_0ppt	100.4	0.00	3.75 ± 0.09 (2.4%)	--
	AFSW_5ppt	100.1	5.44	9.65 ± 0.31 (3.2%)	108.4 ± 5.9
	AFSW_10ppt	100.3	10.93	15.31 ± 0.42 (2.7%)	105.8 ± 3.9

Note that within each batch, the same artificial seawater mother solution was used, but mother solutions differ between batches. "Be found" concentrations give values relative to the preconcentrated initial seawater mass.

* The suffix "org" in sample ID indicates "with organics added".

† Uncertainty is the analytical uncertainty (1 SD) from HR-ICP-MS analysis in absolute and relative (%) numbers.

‡ Analytical uncertainties (1SD) of the measured Be concentrations of spiked samples and the respective unspiked (0 pg/g Be-spiked) samples were propagated into the uncertainty calculation of recovery. The uncertainty of "Be added" from balance is negligible (< 2%).

§ Data was excluded in Fig. 2.2 due to the large uncertainty.

Chapter 3 River-to-ocean pathways of beryllium-9 through estuaries

Abstract

Estuarine processes are key in modulating the riverine input of particle-reactive trace elements to the ocean. An important, but still under-utilized member of these elements is beryllium-9 (^{9}Be) that together with cosmogenic ^{10}Be has been suggested to serve as a quantitative tracer of present and past continental weathering. This study investigates different pathways of terrigenous ^{9}Be through coastal areas into the ocean, based on dissolved ^{9}Be concentrations in surface and bottom waters together with corresponding particulate ^{9}Be concentrations along the salinity gradient in the Changjiang Estuary. Dissolved ^{9}Be in the Changjiang Estuary shows a non-conservative behaviour: At low to mid-salinity where water is well-mixed, ^{9}Be is removed from both surface and bottom waters at low salinity and then released back into the water column at mid-salinity. At high salinity where water is stratified, dissolved ^{9}Be is removed from surface waters, but is released back into bottom waters.

In combination with hydrochemical (e.g., dissolved oxygen) and particulate ^{9}Be data obtained from different extracted phases, we attribute the removal of dissolved ^{9}Be at low salinity to salt-induced colloidal flocculation, whereas in surface waters at high salinity, we ascribe the removal to biological scavenging facilitated by phytoplankton blooms. The release of ^{9}Be into mid- and high-salinity bottom waters is likely dominated by benthic processes, including porewater diffusion and/or submarine groundwater discharge. The contribution from desorption of ^{9}Be from suspended particulate matter is negligible throughout the entire estuary. We propose that the release of ^{9}Be through benthic processes potentially presents the most important contributor to the marine ^{9}Be budget, where this benthic flux of ^{9}Be is likely enhanced by hypoxic conditions in coastal bottom waters.

3.1 Introduction

Estuaries play an important role in modulating riverine fluxes of trace and major elements, nutrients, and organic matter transported to the oceans (Mallick et al., 2022; Mosley and Liss, 2020; Samanta and Dalai, 2016; Yang et al., 2021). As river water mixes with seawater, changes in ionic strength, pH, concentrations of suspended particulate matter (SPM) and redox conditions alter the distribution and composition of chemical materials in the dissolved and particulate phases. Particle-reactive elements are scavenged by SPM and settle to coastal bottom sediments, from which they can be released into coastal seawater during early diagenesis (Audry et al., 2006; Homoky et al., 2016). In addition, submarine groundwater discharge may also contribute a significant quantity of dissolved elements and nutrients to the coastal ocean (Burnett et al., 2001; Kim and Kim, 2014; Moore, 1996).

The marine authigenic $^{10}Be/^{9}Be$ ratio is used as a proxy for, for example, deep ocean circulation patterns (von Blanckenburg et al., 1996), sea ice dynamics (Rhee et al., 2022; Sproson et al., 2022; White et al., 2019), and past continental weathering fluxes (von Blanckenburg and Bouchez, 2014; von Blanckenburg et al., 2015; Willenbring and von Blanckenburg, 2010a; Wittmann et al., 2017). The $^{10}Be/^{9}Be$ ratio is a promising proxy for weathering flux because ^{9}Be is released from rocks by weathering. After release, ^{9}Be is partitioned into dissolved and particulate phases and transferred to coastal oceans mainly by rivers. In the open ocean, the dissolved ^{9}Be mixes with cosmogenic ^{10}Be that is primarily sourced from the atmosphere (von Blanckenburg and Bouchez, 2014; von Blanckenburg et al., 1996). The transport pathways of ^{9}Be through estuaries to the ocean set the efficiency of ^{9}Be delivery to the oceans and in turn determine the sensitivity of the marine $^{10}Be/^{9}Be$ ratio as an indicator of past continental weathering. In this regard, two major pathways have been proposed by von Blanckenburg and Bouchez, (2014) and (von Blanckenburg et al., 2015; von Blanckenburg et al., 2022): dissolved riverine ^{9}Be fluxes escape coastal scavenging (path 1) and reactive riverine particulate-bound ^{9}Be is released from bottom sediment into seawater (path 2). ^{9}Be input via path 1 was assumed to be proportional to the continental ^{9}Be weathering flux if the extent of coastal scavenging remains unchanged, whereas path 2 was suggested to depend primarily on sediment delivery flux and the rate of benthic release processes, but to be independent of coastal scavenging.

Recently, the validity of these assumptions was questioned. Li et al. (2021) contend that coastal scavenging could be enhanced when sediment influx, resulting from increased denudation rate, is high. This, in turn, may counterbalance the increased dissolved ^{9}Be flux through path 1, thus rendering marine $^{10}Be/^{9}Be$ ratio insensitive to weathering flux. However, their model does not take into account that river particle concentration and denudation rate are not linearly correlated (Milliman and Farnsworth, 2011), and further ignores the particulate ^{9}Be source (von Blanckenburg and Bouchez, 2014; von Blanckenburg et al., 2022). A recent study based on

porewater Be data suggested that diagenetic release of ^{9}Be from coastal sediments (path 2) could be the dominating oceanic ^{9}Be input flux (Deng et al., 2023). Given these debates, clarifying the pathways of terrigenous ^{9}Be into the ocean through estuaries and their relative significance are thus fundamental towards interpreting marine ^{10}Be/^{9}Be records.

So far, studies on ^{9}Be behaviour in estuaries have covered seven estuaries (Brown et al., 1992b; Kong et al., 2021a; Kusakabe et al., 1991; Measures and Edmond, 1983; Suhrhoff et al., 2019), and most of them focused on dissolved ^{9}Be in surface waters. The behaviour of dissolved ^{9}Be documented in these estuaries appears to be highly variable. While dissolved ^{9}Be in the Amazon and Congo river estuaries is removed from surface waters (Brown et al., 1992b; Measures and Edmond, 1983), the Ganges, Changjiang (Yangtze River), Pearl River and Zrmanja estuaries are characterized by the release of ^{9}Be from particulates (Brown et al., 1992b; Kusakabe et al., 1991; Measures and Edmond, 1983; Suhrhoff et al., 2019). A small estuary in Scotland, Loch Etive, however displays nearly conservative mixing behaviour (Suhrhoff et al., 2019), meaning the decrease of dissolved ^{9}Be concentrations along a predictable vector that results from river - ocean water mixing. The variable behaviour of dissolved ^{9}Be in different estuaries implies a high sensitivity of ^{9}Be to hydrochemistry (e.g., colloidal load and composition, Suhrhoff et al., 2019) and estuarine processes, which are thus important to resolve for interpretation of marine ^{10}Be/^{9}Be ratio.

In this study, we report dissolved ^{9}Be concentrations in both surface and bottom waters along the entire salinity gradient in the Changjiang Estuary, together with the particulate ^{9}Be concentrations in different chemically extractable fractions of the corresponding SPM. In a previous study low-resolution dissolved ^{9}Be data of Changjiang Estuary surface waters were reported (Measures and Edmond, 1983). The Changjiang River is historically the fourth largest rivers of the world in terms of sediment discharge (Milliman and Farnsworth, 2011). Its estuary represents a typical large, river-dominated estuary characterized by complex hydrodynamic processes that generate a seasonal turbidity-maximum zones (TMZ) and hypoxic conditions (Lin et al., 2020). Because these are globally common phenomena, the Changjiang Estuary serves as a natural laboratory where the different pathways of ^{9}Be into the ocean under a variety of hydro-physicochemical estuarine conditions can be explored.

3.2 Study area, materials and methods

3.2.1 The Changjiang River and its estuary

The Changjiang River is the third longest river in the world, flowing 6300 km eastwards from the Tibetan Plateau into the East China Sea. It historically delivered ~900 km^{3}/yr of water and ~470 Mt/yr of sediment into the Changjiang Estuary and the adjacent sea (Milliman and Farnsworth, 2011). The Changjiang watershed is mainly overlain by sedimentary rocks

composed of marine carbonates, evaporites and alluvium from Precambrian to Quaternary in age. The river water chemistry is dominated by limestone weathering, leading to neutral or slightly alkaline water pH (Chetelat et al., 2008).

The Changjiang Estuary is a mesotidal, partially mixed estuary, with a tide of regular semidiurnal type. The general circulation pattern in the Changjiang Estuary and the adjacent East China sea (ECS) in summer is shown in Fig. 3.1. The Changjiang River enters the East China Sea, forming the highly dynamic Changjiang Diluted Water (CDW) system. The Taiwan Warm Current (TWC) flows north-eastward parallel to the 50-m isobath and enters the submerged river valley off the Changjiang, which can be further divided into the Taiwan Warm Current Surface Water (TWCSW) and Taiwan Warm Current Deep Water (TWCDW) (Zhang et al., 2014). In summer, the TWCSW originates mostly from the Taiwan Strait Warm Current, while the Kuroshio Subsurface Water dominates the TWCDW (Lian et al., 2016; Zhang et al., 2014).

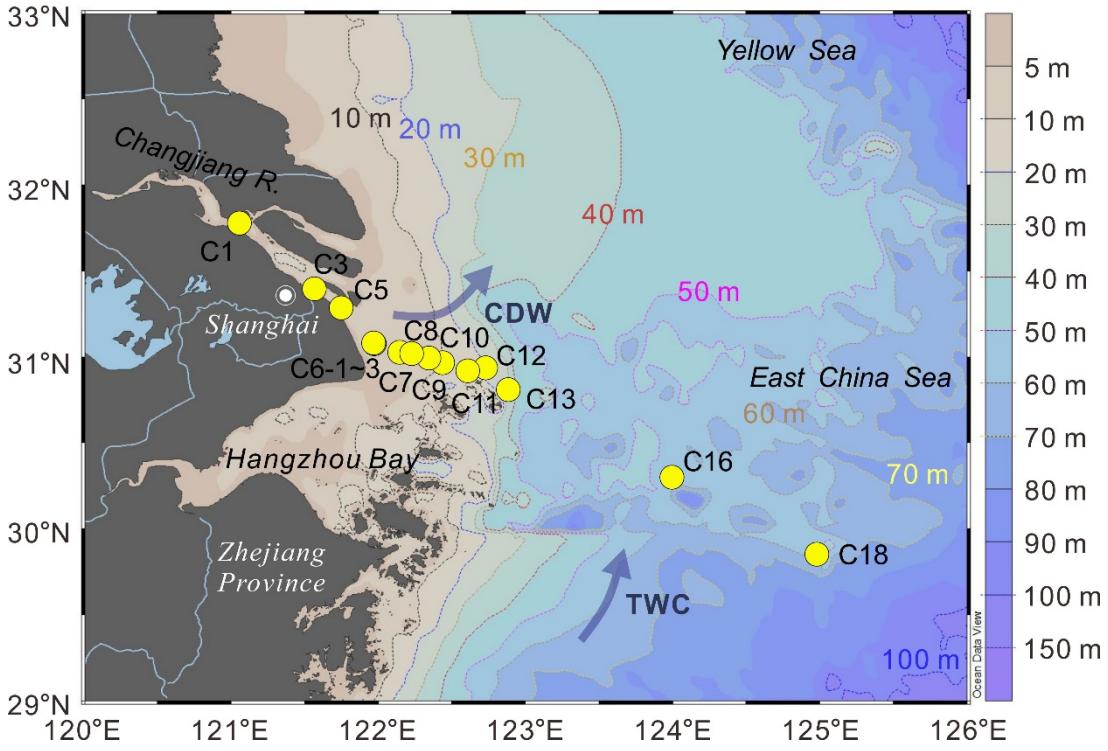

Figure 3.1 Map showing the locations of sampling stations along the Changjiang-Estuary-Shelf Transect. Major water masses in the study area in summer are indicated: CDW, Changjiang Diluted Water; TWC, Taiwan Warm Current. All maps in this article were created using "Ocean Data View" (https://odv.awi.de, 2022.)

From the complex and dynamic interactions between runoff, stratification and tides (Li and Zhang, 1998; Wu et al., 2012), a turbidity maximum zone develops in the river mouth zone of the Changjiang Estuary where the bottom SPM concentration can be >10 g/L (Lin et al., 2020). The deposition of abundant riverine SPM causes the upstream Changjiang Estuary to be very

shallow (6.5 m average) (Wang and Liu, 2003). The Changjiang Estuary water is dominated by oxic conditions, with occasional occurrence of seasonal hypoxia. Hypoxic conditions usually occur below the pycnocline in summer, reaching a maximum in August, then weaken in autumn, and finally disappear in winter (Zhu et al., 2016).

3.2.2 Sample collection

Field sampling was conducted between August and September 2019 during the cruise of the Key Elements Cycling in the Changjiang-Estuary-Shelf Transect (KECES 2019) organized by the State Key Laboratory of Marine Geology, Tongji University. A total of 15 stations (located between 120°-126°E and 29°-32°N, Fig. 3.1) were sampled along the Changjiang-Estuary-Shelf Transect from the river mouth of Changjiang (sampling station C1, 121.06°E, 31.78°N) to the East China Sea continental shelf (station C18, 124.99°E, 29.86°N). Surface seawater samples were collected approximately 3-4 m upstream from the ship's bow via a pre-cleaned Masterflex I/P® Precision Pump tubing (C-Flex®) attached to the front end of a carbon fibre pole sampler, and water was pumped by a peristaltic pump. Near-bottom (~2 m above the seafloor) water samples were collected using a 5 L Teflon-coated Niskin-X bottle attached to a nylon rope. After collection, samples were immediately filtered onboard through an acid-cleaned 0.45 μm filter (147 mm in diameter, Supor® PES, Pall) using a customized Teflon filter holder. The filtrates were stored in pre-cleaned LDPE bottles (Nalgene), acidified to pH < 2 with trace metal grade HCl, and stored at 4°C until ^{9}Be analysis. After filtering, the membranes (trapping SPM) were also stored refrigerated at 4°C. The SPM samples were dried to constant weight at 40°C in a hot-air convection oven over several days upon arrival in the laboratory.

3.2.3 Analytical methods

3.2.3.1 Auxiliary parameters

Salinity, temperature and dissolved oxygen (DO) were recorded with a SBE25 Conductivity-Temperature-Depth (CTD) recorder (Sea-Bird) equipped with a SBE43 DO sensor. The salinity was calibrated by the salinity of discrete samples measured by a Multi 340i multi-parameter meter (WTW), and the DO sensor was calibrated against water sample analyses conducted by the Winkler titration method (Carpenter, 1965). The pH was determined using a pH-meter (PHS-3C), with analytical uncertainty of 0.01 units. The SPM concentration was determined by weighting the difference of dried membranes (pre-cleaned in 0.1 M HCl) before and after water filtration of a given volume of water.

3.2.3.2 Dissolved ^{9}Be analysis

^{9}Be was preconcentrated from 100-200 mL of seawater using the iron co-precipitation method following established protocols (Chapter 2). After preconcentration, the samples were dissolved in 1 mL 3% HNO_3 doped with 1 ng/g rhodium (Rh) as internal standard to correct machine drift for ^{9}Be analysis on a sector-field high-resolution inductively coupled plasma-mass spectrometer (HR-ICP-MS, Element2, Thermo Fisher Scientific) in low-resolution mode. The doubly charged ion rate was less than 3% and the oxide formation rate was less than 5%. ^{9}Be was quantified by an external calibration with standards prepared gravimetrically from our in-house ^{9}Be carrier solution. All the measurements were carried out at the Helmholtz Laboratory for the Geochemistry of the Earth Surface at GFZ Potsdam, Germany (von Blanckenburg et al., 2016). Procedure blanks were always below the detection limit (average instrument blank plus 3 times standard deviation (SD); as low as 4.0 pg Be, at most 15.0 pg Be), which accounts for 3-21% of ^{9}Be in our samples. The long-term external repeatability was 5% (1SD, n=14), monitored by processing an in-house artificial seawater standard (prepared by synthetic salt, Dupla Marin Premium Reef Salt Natural Balance, product code DM81432_MA) from January 2021 to January 2022. Since no certified seawater standard is available for ^{9}Be, we spiked artificial seawater (100-200 mL) with known amounts of ^{9}Be (from 5 pg/g to 20 pg/g) to monitor accuracy. The ^{9}Be yields were within ±10%, with an average of 97.6 ± 5.6% (1SD, n=13). Hence, we propagated a relative uncertainty of 10% to all ^{9}Be measurements as a conservative estimate.

3.2.3.3 Particulate ^{9}Be and elemental concentration analyses from sequential extraction

We applied Be-extraction procedures to SPM samples to analyse ^{9}Be and other element concentrations in the extracted and the remaining silicate residue fractions, with the aim to investigate the possible re-distribution of ^{9}Be between the dissolved phase and extractable phases of SPM. About 0.5 to 1 g of SPM was washed 3 times using pH 8-adjusted Milli-Q water in order to remove the remaining sea salt. After that, four fractions were sequentially extracted following the modified procedure from Wittmann et al. (2012), including: 1) the exchangeable fraction ("ex", 1M CH_3COONH_4) containing weakly adsorbed elements retained on the SPM surface by relatively weak electrostatic interactions, 2) the reactive oxy-hydroxide fraction ("reac", 0.5M HCl, 1M $NH_4OH{\cdot}HCl$) containing amorphous and crystalline (hydr)oxides, note that this treatment would also dissolve carbonate phases present in the sample, 3) the organic fraction ("org", 0.01M HNO_3, 10M H_2O_2) containing the organic matter, and 4) the remaining silicate residue fraction ("min", 28M HF, 14M HNO_3) containing the lithogenic crystalline minerals.

To extract the exchangeable fraction, 12 mL of 1M ammonium acetate (pH = 7) (Óvári et al., 2001) was added to each sample in pre-cleaned centrifuge tubes. The tube was placed on a

reciprocating shaker for 24 h to achieve equilibrium with respect to Be sorption. After equilibration, the slurry was centrifuged at 4000 rpm and the supernatant was decanted. The residue was washed twice with Milli-Q water and the wash solutions were collected along with the supernatant. Except for the exchangeable fraction, reagents used for the other fractions and the detailed procedures can be found in Wittmann et al. (2012). The exchangeable fraction leachate was further purified using the iron co-precipitation method for ^{9}Be determination on the HR-ICP-MS, following the same protocol applied to seawater samples. ^{9}Be analyses for the other fractions as well as other elemental analyses were performed using an optical emission, inductively-coupled plasma spectrometer (ICP-OES, model Varian 720-ES with axial optics). The long-term external uncertainty for OES measurement is 5% (1SD) (Wittmann et al., 2012).

3.2.3.4 Specific surface area (SSA) and powder X-ray diffraction (XRD) analyses

The specific surface area (SSA) was calculated using the Brunauer–Emmett–Teller (BET) equation (Brunauer et al., 1938). Prior to N_2 sorption measurements, samples were vacuum-dried at room temperature for at least 16 h, followed by degassing under heating and vacuum, using a VacPrepTM 061 Sample Degas System (Micromeritics, Norcross, GA, USA) The accuracy and precision of the SSA measurement is ~ 1.1% and 0.29%, respectively, based on repeat analysis (n = 3) of Micromeritics certified reference material (Carbon Black, 044-16833-00, $SSA_{BET} = 21.52 \pm 0.75$ m^2 g^{-1}).

The mineralogical composition of the SPM samples was identified by powder X-ray diffraction (XRD) analysis. XRD measurements were performed using a STOE STADI P diffractometer with a Cu X-ray source fitted with a curved Ge (111) monochromator and a DECTRIS MYTHEN2 detector in a flat plate transmission geometry. Diffraction patterns were measured over the 2θ range of 0–84°, with the sample plate being rotated relative to 2θ at a ratio of 1:2 and a data collection time of about 7 min per data point with a resolution of 0.015° 2θ. All the measurements were carried out in the Mineral Synthesis and Characterization Laboratories at GFZ Potsdam.

3.3 Results

3.3.1 Water physicochemical properties

Water physicochemical properties of the studied 15 stations along the Changjiang-Estuary-Shelf Transect are shown in Fig. 3.2 and Table 3.1. In general, water was vertically well-mixed at salinities (S) below 20 PSU (practical salinity units, in permill), but stratified when S > 20 PSU, as indicated by the vertical distribution of salinity and temperature (Fig. 3.2a and b). We thus divided the transect into a well-mixed zone (low-mid salinity, S ≤ 20 PSU, stations C1-C9) and a stratified zone (high salinity, S > 20 PSU, C10-C18). In the well-mixed zone, the water

was well-oxygenated (DO > 5 mg/L) with a nearly constant pH value ranging from 7.8-7.9 (Fig. 3.2c and d). A turbidity maximum zone occurred over a salinity range of 6-18 PSU where water depths are shallower (Fig. 3.2c and e, from station C6-2 to C9), and taking 0.7 g/L as the threshold value of the turbidity maximum zone (Jiang et al., 2013). The SPM concentrations were generally higher in bottom waters (average of 0.83 g/L) than in surface waters (average of 0.39 g/L) (Table 3.1). In the stratified zone, the pH value of surface waters (average of 8.14) is slightly higher than that of bottom water (average of 7.82). The DO progressively decreased from surface to bottom waters, reaching hypoxic levels (threshold of 2 mg O_2/L, Vaquer-Sunyer and Duarte (2008)) near the bottom of station C13. Although the SPM concentrations do not vary as significantly as in the well-mixed zone, they were still higher in the bottom (average of 0.11 g/L) than in surface waters (average of 0.02 g/L) (Table 3.1).

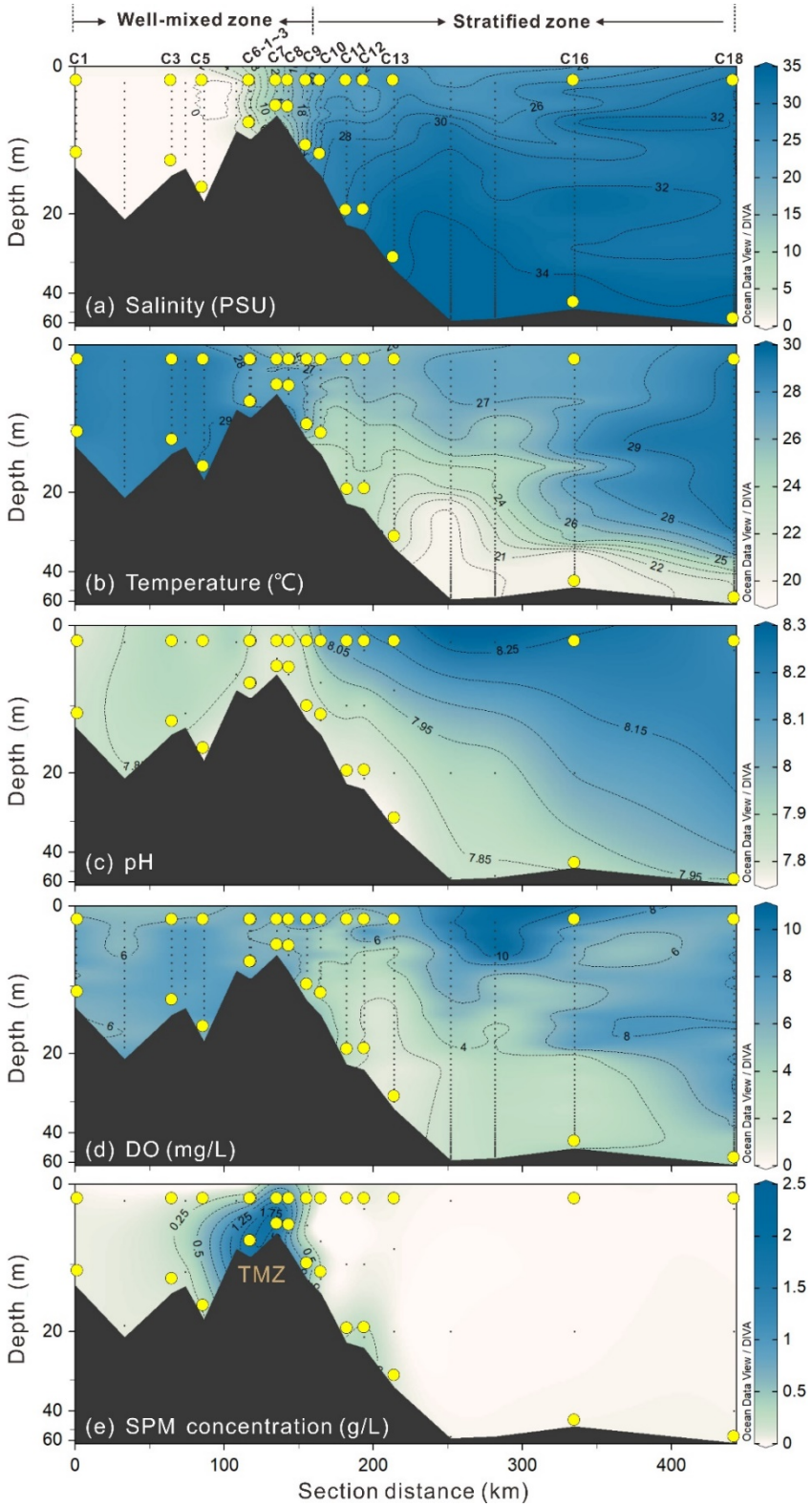

Figure 3.2 Physical and chemical properties of the water column along the Changjiang-Estuary-Shelf Transect from station C1 to C18: (a) practical salinity, (b) in-situ temperature, (c) pH, (d) dissolved oxygen concentration (DO), (e) suspended sediment concentration (SPM concentration). Blank vertical dots in the figures represent sampling sites of the KECES cruise, and yellow circles represent the sampling sites for dissolved ^{9}Be measurement in this study. The depth of the ocean floor shown is not on a linear scale. TMZ: turbidity maximum zone.

Table 3.1 Hydrological parameters and ^{9}Be concentrations in the surface and bottom waters along the Changjiang-Estuary-Shelf Transect.

Sample ID	Longitude (°E)	Latitude (°N)	Section distance (km)	Water depth (m)	Salinity (PSU)	Temperature (°C)	pH	Suspended Particulate Matter (SPM) concentration (g/L)	DO (mg/L)	Dissolved ^{9}Be (nM)	DIP (μM)
C1S	121.06	31.78	0	1	0.0	28.9	7.80	0.045	6.35	0.144	0.55
C1B	121.06	31.78	0	11	0.0	28.9	7.83	0.058	6.45	0.152	0.75
C3S	121.57	31.40	64.5	1	0.0	28.8	7.90	0.097	5.97	0.122	0.49
C3B	121.57	31.40	64.5	12	0.0	28.9	7.87	0.199	6.96	0.131	0.57
C5S	121.75	31.29	85.9	1	0.0	28.9	7.84	0.199	6.04	0.136	0.45
C5B	121.75	31.29	85.9	16	0.0	29.1	7.78	0.280	7.47	0.143	0.79
C6-1S	121.97	31.09	116.5	1	1.0	28.1	7.84	n.d.	6.21	0.126	1.18
C6-2S	121.98	31.09	117.2	1	4.1	27.8	7.83	0.384	5.86	0.098	1.62
C6-2B	121.98	31.09	117.2	7	6.2	27.4	7.79	2.078	6.68	0.113	1.81
C6-3S	121.99	31.08	118.0	1	9.4	26.9	7.83	0.479	6.62	0.107	1.55
C6-3B	121.99	31.08	118.0	7	9.1	26.9	7.84	1.541	6.28	0.112	1.49
C7S	122.15	31.03	135.2	1	12.5	27.3	7.81	1.141	5.80	0.118	1.11
C8S	122.24	31.02	142.9	1	14.4	27.5	7.84	n.d.	5.52	0.110	0.81
C8B	122.24	31.02	142.9	6	14.9	27.5	7.83	n.d.	5.95	0.118	1.23
C9S	122.36	31.00	155.5	1	16.9	22.2	7.84	n.d.	5.94	0.097	1.10
C9B	122.36	31.00	155.5	10	17.8	26.8	7.80	0.838	5.05	0.108	0.95
Boundary between well-mixed zone and stratified zone											

Continued

Sample ID	Longitude (°E)	Latitude (°N)	Section distance (km)	Water depth (m)	Salinity (PSU)	Temperature (°C)	pH	Suspended Particulate Matter (SPM) concentration (g/L)	DO (mg/L)	Dissolved ^{9}Be (nM)	DIP (μM)
C10S	122.45	30.97	164.6	1	21.9	26.9	8.08	0.016	6.39	0.048	0.23
C10B	122.45	30.97	164.6	12	26.7	25.1	7.82	0.035	3.74	0.098	0.69
C11S	122.62	30.92	188.9	1	24.2	24.3	8.06	0.017	4.62	0.087	0.21
C11B	122.62	30.92	188.9	20	30.0	23.6	7.78	0.200	3.65	0.096	0.73
C12S	122.74	30.94	200.9	1	22.3	26.6	8.11	0.048	8.11	0.032	0.15
C12B	122.74	30.94	200.9	21	31.0	24.0	7.78	0.366	2.08	0.094	0.79
C13S	122.89	30.81	221.4	1	26.0	26.4	8.16	0.024	6.04	0.039	0.22
C13B	122.89	30.81	221.4	30	33.6	22.1	7.76	0.016	1.62	0.082	0.80
C16S	124.00	30.30	342.1	1	25.5	27.4	8.24	0.008	8.32	0.021	0.08
C16B	124.00	30.30	342.1	46	34.6	20.1	7.87	0.024	3.38	0.046	0.71
C18S	124.99	29.87	449.2	1	32.0	29.4	8.17	0.005	6.63	0.030	0.03
C18B	124.99	29.87	449.2	62	34.4	24.0	7.93	0.026	4.61	0.039	0.58

The suffix “S” and “B” in sample ID indicate “surface water” and “bottom water”, respectively.

n.d. = not determined

PSU = practical salinity units, in permill; DO = dissolved oxygen; DIP = dissolved inorganic phosphorus. DIP taken from Xu et al. (2021).

3.3.2 Dissolved ^{9}Be

Dissolved ^{9}Be concentrations ($[^{9}Be]_{diss}$, square brackets denote concentrations) along the Changjiang-Estuary-Shelf Transect varied from 0.02 nM to 0.15 nM (Table 3.1, Fig. 3.3), comparable to previously published data (Measures and Edmond, 1983). The $[^{9}Be]_{diss}$ in surface and bottom waters are nearly identical at S ≤ 20 PSU, but diverge at >20 PSU. This characteristic corresponds to the stratification of water (section 3.3.1). In the well-mixed zone (S<20 PSU), $[^{9}Be]_{diss}$ in both surface and bottom waters decrease during the initial mixing between river water and seawater, reaching a minimum at about S = 4 PSU. After that, $[^{9}Be]_{diss}$ remain relatively constant at a value of about 0.11 nM at mid-salinity (5-20 PSU), despite increasing dilution by seawater. In the stratified zone, $[^{9}Be]_{diss}$ in the surface water decrease further, except for one sample collected at station C11. In contrast, in bottom water, no obvious decrease is observed in this zone until a salinity of 34 PSU is reached. $[^{9}Be]_{diss}$ in bottom waters are much higher than that in surface waters at the same salinities.

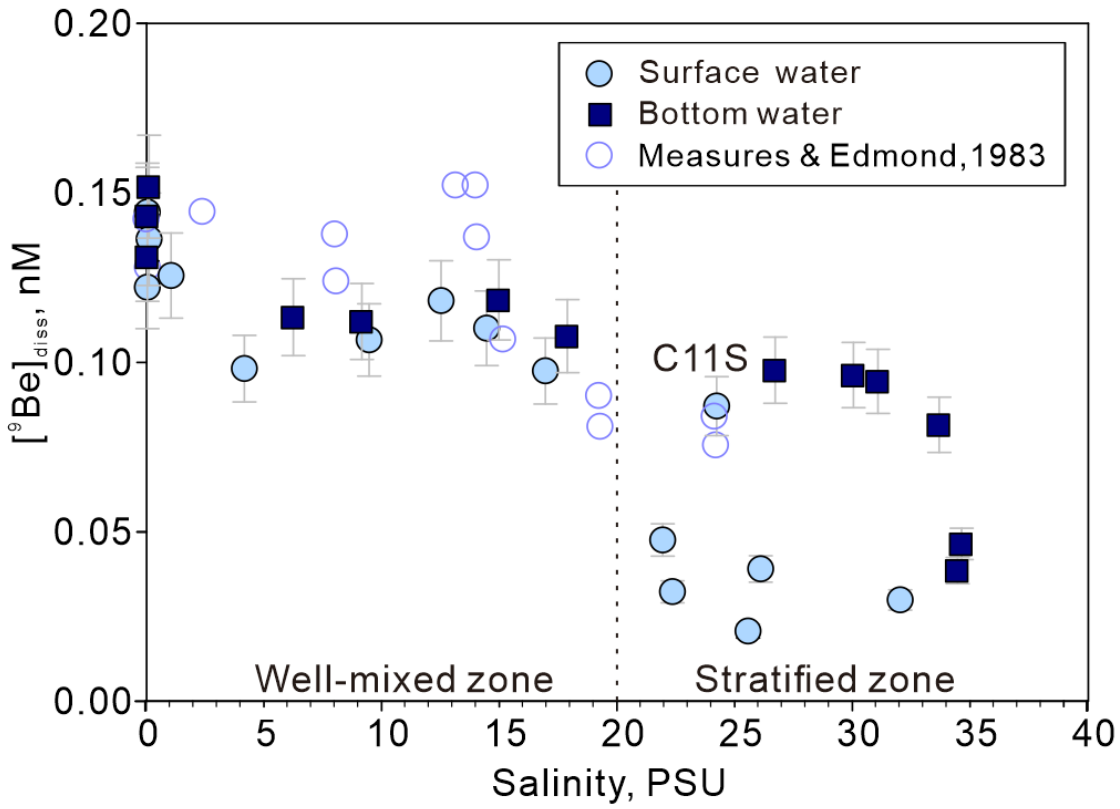

Figure 3.3 Dissolved ^{9}Be concentrations along the salinity gradient of the Changjiang-Estuary-Shelf Transect of this study compared to surface data from Measures and Edmond (1983) (for that study, no uncertainty estimates are available). A 10% uncertainty is given that represents the long-term recovery for iron co-precipitation method.

3.3.3 Particulate ^{9}Be

To detect changes in the ^{9}Be distribution in different chemically extractable fractions of the SPM during estuarine mixing, we calculated the [^{9}Be] in each fraction relative to the bulk particulate weight (i.e., initial mass of bulk particulates before leaching). Results are shown in Fig. 3.4 and Table S3.2. We found less than 1‰ of total ^{9}Be to be present in the "ex" fraction. Note that data for the "ex" fraction is not available for all samples due to sometimes insufficient sample size. Around 29% to 34% of ^{9}Be is bound with the "reac" fraction. The organic ^{9}Be only accounts for 1% to 2% of total particulate Be. Most ^{9}Be (64% to 69%) is retained in the "min" fraction.

Along the Changjiang-Estuary-Shelf Transect, the exchangeable [^{9}Be] ([^{9}Be]$_{ex}$) is somewhat higher in fresh water-SPM (C5S and C5B) than in saline water-SPM (Fig. 3.4). The [^{9}Be]$_{reac}$ displays a slight hump at C6-1 and C6-2 stations at around 1-6 PSU. The [^{9}Be]$_{org}$ remains generally constant within a range of 0.02 to 0.04 μg/g, whereas in the "min" fraction, [^{9}Be]$_{min}$ varies from 1.22 to 1.63 μg/g with no clear trend along the transect.

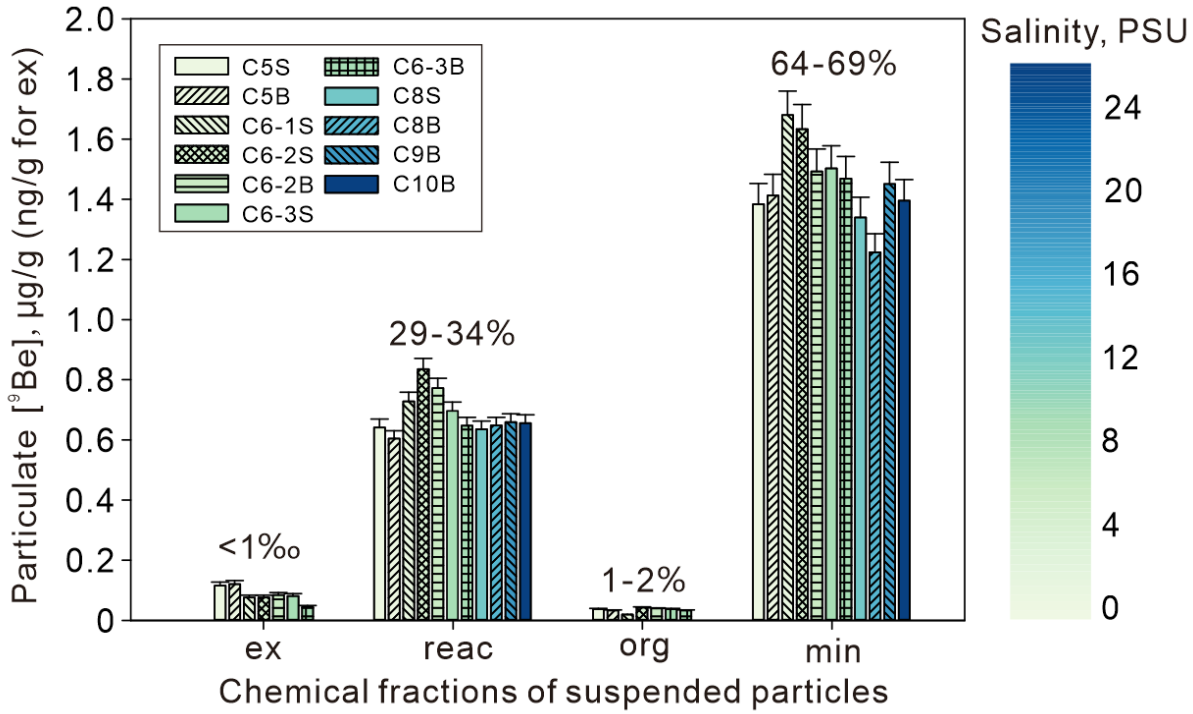

Figure 3.4 Particulate ^{9}Be concentrations in different chemical fractions along the Changjiang-Estuary-Shelf Transect. The percentages give the proportion of ^{9}Be in each fraction relative to the total (sum of all fractions).

3.3.4 Specific surface area, mineral and major elemental composition of SPM

The specific surface area of the Changjiang Estuary SPM ranges from 16.14 to 27.92 m^2/g along the salinity gradient (Table S3.3). Fresh water-SPM (C5S and C5B) shows lower specific surface area (17.04 m^2/g on average) than saline water-SPM (24.21 m^2/g on average). The mineral composition comprises mainly quartz, plagioclase (albite-rich), k-feldspar (microcline-rich), illite, chlorite, kaolinite and calcite (Fig. S3.1). No significant variation in mineral composition along the salinity gradient can be observed from the XRD pattern (Fig. S3.1).

Major elemental data of all chemically extractable fractions (expressed relative to the initial mass of bulk particles, in μg/g) are provided in Table S3.2. For all samples, the majority of the "ex" fraction is composed of Ca (15-27% of the total Ca amount in bulk samples) and Mn (6-9%). For SPM sampled from saline waters, the "ex" fraction also contains a non-negligible amount of Mg and Na (5-10%). Concentrations of the other major elements are generally depleted (<2%) in this fraction. The "reac" fraction contributes up to 60-80% of total Ca and Mn, indicating the dissolution of calcite and Mn-(oxy)hydroxides during leaching. Other elements are lower (Fe 27-33%, Mg 42-49%, Al 5-6%, K and Na < 4%) in this fraction. For the "org" fraction, all elemental concentrations analysed are negligible (<1%) compared to the bulk concentration. The "min" fraction comprises most of bulk for Na (89-99%), K (95-98%), Al (94-95%), and less for Fe (70-72%), Mg (51-53%), Mn (15-17%) and Ca (6-10%).

3.4 Discussion

We will now firstly discuss the changes in particulate and dissolved ^{9}Be concentrations along the salinity gradient, respectively, as well as the underlying control mechanisms. Building upon this, we then discuss their implications for ^{9}Be pathways into oceans.

3.4.1 Particulate ^{9}Be distribution

The distribution of ^{9}Be among various chemically-extracted phases represents distinct reservoirs capable of removing or releasing ^{9}Be from/into seawater during estuarine mixing or after deposition onto the seafloor. In the exchangeable phase where the adsorption-desorption process predominantly controls ^{9}Be behaviour, significant negative correlations are apparent between $[^{9}Be]_{ex}$ and $[K]_{ex}$, $[Mg]_{ex}$, $[Na]_{ex}$, respectively (Fig. 3.5), suggesting that Be^{2+} is competing with K^{+}, Mg^{2+} and Na^{+} via ion exchange during estuarine mixing. Within the "reac" fraction, $[^{9}Be]_{reac}$ shows a significant positive correlation with $[Al]_{reac}$, $[Mg]_{reac}$ and $[Fe]_{reac}$, but a negative correlation with $[Ca]_{reac}$ (Fig. 3.5), indicating the variation of $[^{9}Be]_{reac}$ is closely associated with the enrichment of Al, Mg and Fe-(oxy)hydroxides and dilution by carbonate. This implies that Al, Mg and Fe-(oxy)hydroxides serve as primary carrier of ^{9}Be, and thus the mobility of reactive ^{9}Be is probably influenced by redox conditions. While the $[^{9}Be]_{org}$ remains almost constant along the transect (see section 3.3.3), the $[^{9}Be]_{min}$ shows a significant positive linear correlation with $[Al]_{min}$, $[K]_{min}$, $[Mg]_{min}$ and $[Fe]_{min}$ (Fig. 3.5). Based on the mineral composition of SPM in the Changjiang Estuary (Fig. S3.1), we infer that the variation in $[^{9}Be]$ in the silicate residue is likely a consequence of the relative predominance of plagioclase feldspars, as carrier of primary ^{9}Be (Ryan, 2002).

Based on the distribution of ^{9}Be between chemically-extracted and dissolved phases, we infer that the variations of $[^{9}Be]$ in the "reac" and "min" fractions are the result of physical mineral sorting rather than chemical water-particle interactions, given that the dissolved ^{9}Be pool is two orders of magnitude smaller than the "reac" and "min" pools (Fig. 3.6). The fact that $[^{9}Be]$ in the "reac" and "min" fractions do not change drastically with distance from land (Table 3.1) demonstrates that mineral sorting in estuaries is not solely controlled by transportation distance, but also by other factors, such as sediment re-suspension due to e.g., tidal influence.

While water-particle interactions during estuarine mixing unlikely affect the "reac" and "min" pools, in turn, they may significantly impact the dissolved and exchangeable ^{9}Be pools (Fig. 3.6). Therefore, we will mainly focus on the changes in dissolved and exchangeable $[^{9}Be]$ and the underlying controlling mechanisms in the forthcoming discussion.

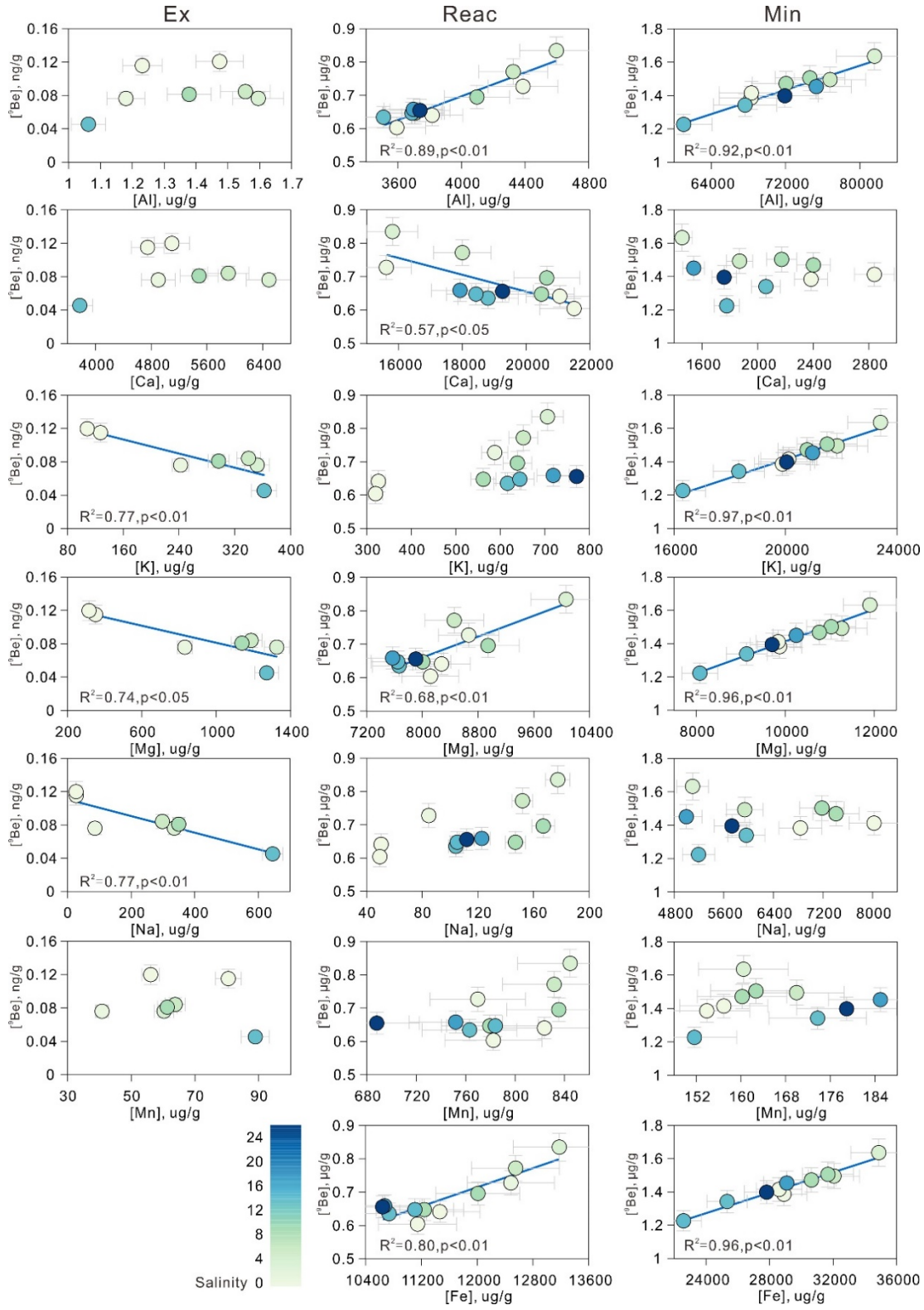

Figure 3.5 ^{9}Be concentrations (color-coded for salinity) vs. major elemental concentrations in exchangeable (ex), reactive (reac) and silicate residue (min) fractions of SPM. The linear regression line is only shown when R^2 (the coefficient of determination, i.e., the squared correlation coefficient) > 0.5. Fe concentrations were below the detection limit for the "ex" fraction.

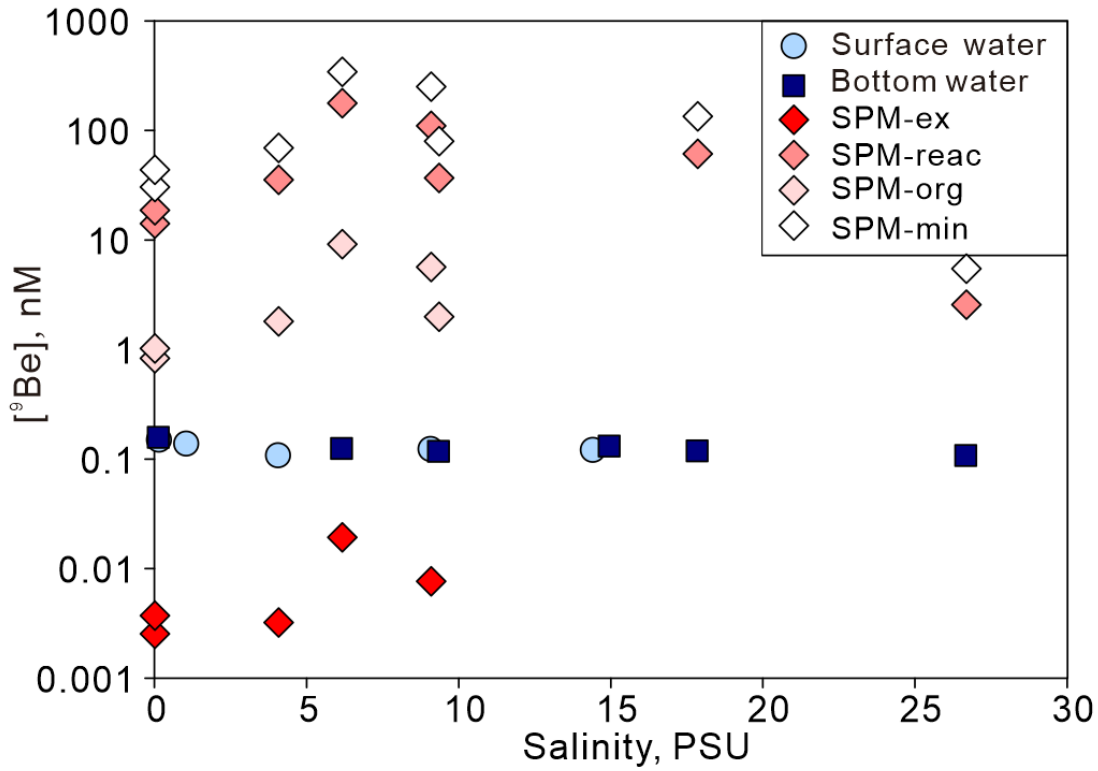

Figure 3.6 The ^{9}Be distribution in the different chemically-extracted phases of SPM (calculated by forming the product of [^{9}Be] in each fraction (µg/g) times the SPM concentration (in g/L, Table 3.1) in the dissolved phase. Error bars are smaller than symbol size.

3.4.2 Quantification of dissolved ^{9}Be behaviour with a three end-member mixing model

Dissolved ^{9}Be along the Changjiang-Estuary-Shelf Transect shows a non-conservative behaviour with complex removal and release patterns, depending on salinity and oceanographic setting (i.e., well-mixed vs. stratified zone, Fig. 3.3). To quantify the removal and release of dissolved ^{9}Be during estuarine mixing, we first calculate the theoretical conservative concentrations of dissolved ^{9}Be at each station that would result if changes in $[^{9}Be]_{diss}$ solely were a consequence of physical water-mass mixing. In a diagram of potential temperature versus salinity (Fig. 3.7), all the data from the Changjiang-Estuary-Shelf Transect fall into the interior of a triangular space (outlined in grey, Fig. 3.7), suggesting the mixing of three end-members (Renner, 1989; Tomczak, 1981). We define the three end-members as Changjiang Diluted Water (CDW), Taiwan Warm Current Surface Water (TWCSW), and Taiwan Warm Current Deep Water (TWCDW) according to their specific potential temperatures and salinities. This classification of end-members is consistent with previous studies (Wang et al., 2021; Zhang et al., 2014). The surface water collected at C11 station show a similar origin as bottom water (Fig. 3.7), indicating the development of upwelling in this area.

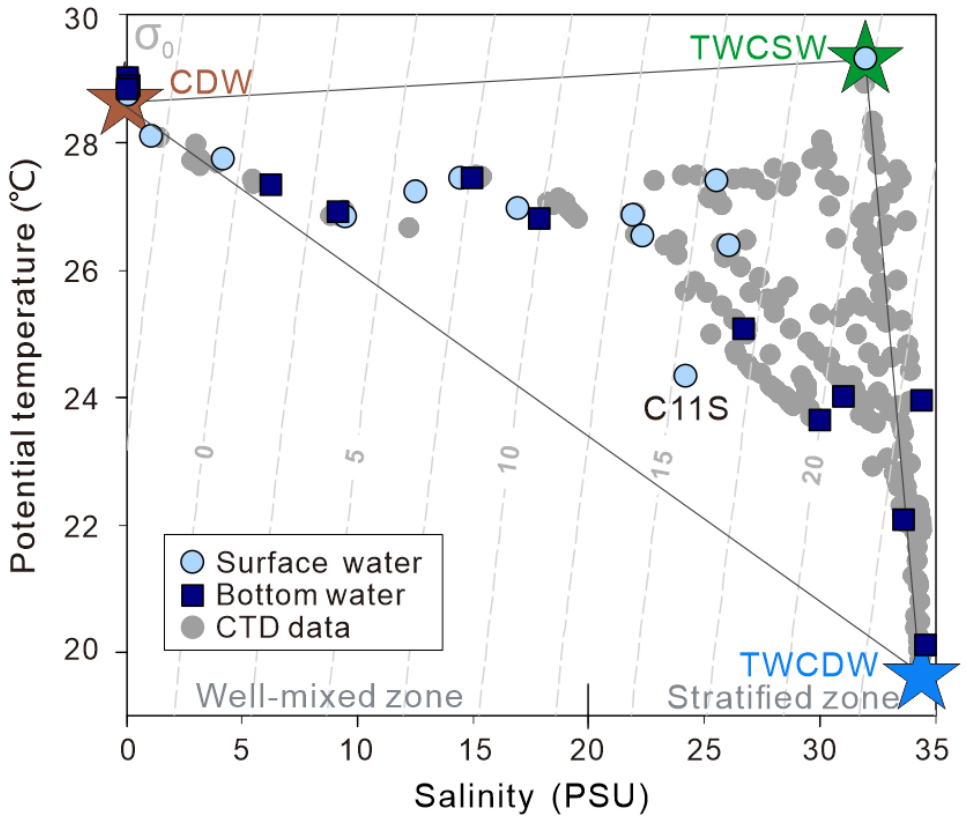

Figure 3.7 Potential temperature vs. salinity plot with potential density isopycnals (σ_0, dotted grey lines) along the Changjiang-Estuary-Shelf Transect. The gray dots are CTD profile data from all stations, whereas the light blue circles and dark blue squares represent samples measured for ^{9}Be in this study. The brown, green and blue stars indicate three water endmembers: Changjiang Diluted Water (CDW), Taiwan Warm Current Surface Water (TWCSW), and Taiwan Warm Current Deep Water (TWCDW), respectively.

We thus calculate the theoretical conservative concentrations of dissolved ^{9}Be using a three-endmember mixing model (see supplementary material). The extent of ^{9}Be removal/release compared to conservative mixing is described by $\Delta[^{9}Be]$, i.e., the difference between field values ($[^{9}Be]_{measured}$) and values predicted by the mixing model. We interpret negative values of $\Delta[^{9}Be]$ such that removal processes dominate over release processes, while positive values suggest the opposite.

Results of this mixing model (Fig. 3.8, Table S3.4) suggest that in the well-mixed zone, the dissolved ^{9}Be is first dominated by removal processes when salinity increases from 0 to 5 PSU (designated as low-salinity range thereafter to enhance clarity for subsequent discussions), but is gradually dominated by release processes from 5 to 20 PSU (designated as mid-salinity range thereafter). In the stratified zone (S > 20 PSU), we note that $\Delta[^{9}Be]$ shows removal from surface

waters, except one outlier for surface water C11S evidently affected by coastal upwelling, while ^{9}Be release is evident in bottom waters.

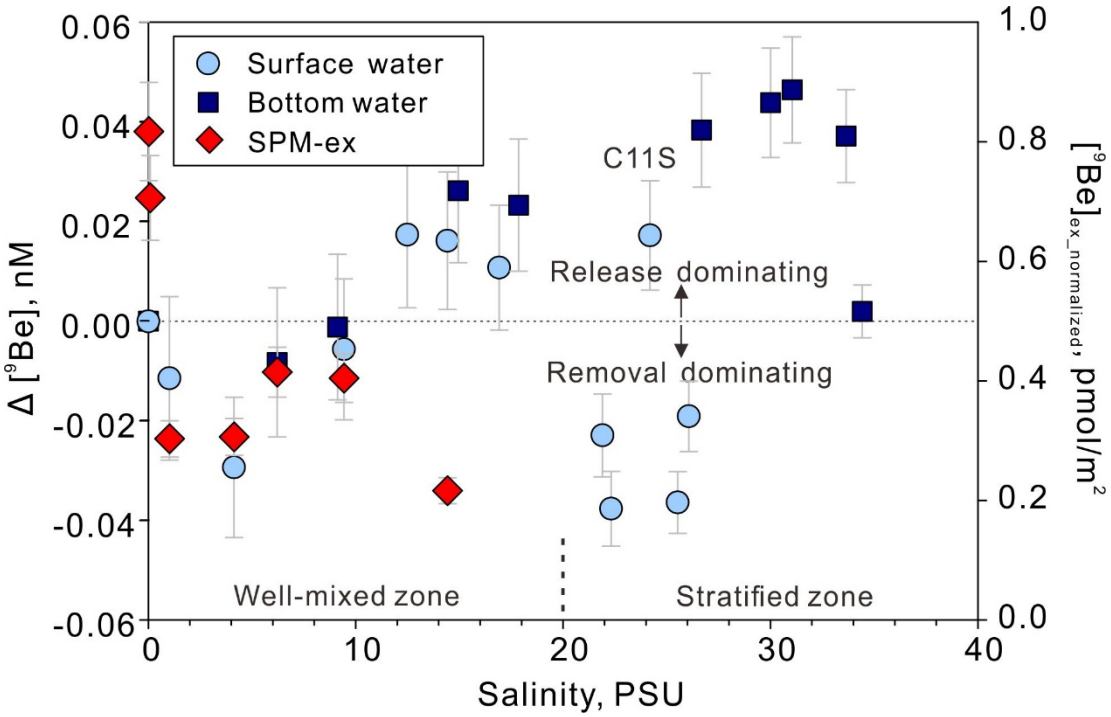

Figure 3.8 The difference of measured dissolved ^{9}Be concentration relative to conservative mixing (Δ[^{9}Be], calculated from supplemental eqs. 1-5), compared to the exchangeable ^{9}Be concentration in the corresponding SPM (normalized by surface area, in pmol/m^{2}) along the Changjiang-Estuary-Shelf Transect. The uncertainty of Δ[^{9}Be] is propagated from the analytical uncertainty of each sample and the three endmembers (see supplementary material). An analytical uncertainty of 10% for [^{9}Be]$_{ex}$ and of 1.1% for specific surface area is propagated to the uncertainty of [^{9}Be]$_{ex\_normalized}$.

3.4.3 Mechanisms controlling the removal or release of dissolved ^{9}Be

A number of potential mechanisms may contribute to the removal or release of dissolved ^{9}Be during estuary mixing. These include 1) adsorption and desorption onto/from particle surfaces (see section 3.4.3.1), 2) flocculation/deflocculation of colloids (section 3.4.3.2), and 3) porewater diffusion/expulsion and submarine groundwater discharge, which are part of the "benthic flux" pathway (section 3.4.3.3), and are hence conceptually lumped together in this study. Next, we will identify the potential controlling processes based on the relationships between dissolved Δ[^{9}Be] and the particulate [^{9}Be] in relation to the corresponding water physicochemical parameters.

3.4.3.1 Adsorption-desorption

Many studies have demonstrated the significance of sorption onto SPM in controlling the dissolved concentrations of trace metals in estuaries. As ionic strength increases at low to mid-salinity, desorption of metals from SPM is induced. Such desorption is thought to present an important source for trace elements such as Ba and Ra (Cao et al., 2021; Li et al., 2021a; Li et al., 1984b; Samanta and Dalai, 2016; Tipper et al., 2021). Given that most Be adsorption-desorption occurs within one day (Boschi and Willenbring, 2016; Li et al., 1984a; You et al., 1989), and if adsorption-desorption is the dominating process functioning at low to mid-salinity, we expect the $\Delta[^9Be]$ and the corresponding particulate $[^9Be]_{ex}$ to inversely correlate. However, previous studies have shown that sorbed Be concentrations tend to increase with increasing specific surface area (SSA) (Aldahan et al., 1999, Willenbring and von Blanckenburg, 2010, Shen et al., 2004), or even correlate with SSA (Boschi and Willenbring, 2021). Considering this, we normalize $[^9Be]_{ex}$ for specific surface area (termed $[^9Be]_{ex\_normalized}$, in pmol/m^2) as a first-order method to eliminate the effect of changing surface area, potentially induced by estuarine mineral grain sorting, on sorbed Be concentrations. The $[^9Be]_{ex\_normalized}$ and $\Delta[^9Be]$ both show a steep decline at low salinity followed by an increase at 4-10 PSU for all samples, except the $[^9Be]_{ex\_normalized}$ datapoint at ca. 12 PSU (Fig. 3.8). The drop of $[^9Be]_{ex\_normalized}$ at the onset of mixing indicates ^9Be desorption from SPM into the dissolved phase, which is likely caused by desorption of ^9Be via ion exchange with K^+, Mg^{2+} and Na^+ stemming from seawater as mentioned in section 3.4.1. Hence, the removal of dissolved ^9Be at low salinity cannot be explained with ^9Be adsorption onto SPM, implying 1) another mechanism is operating and 2) that the exchangeable pool of river-borne ^9Be available for desorption is too small (ca. 0.003 nM, Fig. 3.6) to counterbalance the initial removal of dissolved ^9Be. Although at mid-salinity the ^9Be exchangeable pool becomes larger due to higher SPM concentrations (Fig. 3.6), overall increasing $[^9Be]_{ex\_normalized}$ at 4-10 PSU (Fig. 3.8) suggest that ^9Be is not desorbed from, but instead, rather adsorbed onto SPM. As such, neither the ^9Be removal nor release observed in the well-mixed zone is likely a consequence of direct ^9Be adsorption-desorption, implying that other processes are at play.

The above analysis cannot be done in the stratified zone as we lack $[^9Be]_{ex}$ data. Previous studies have shown that in addition to the ionic strength of the liquid, the sorption behaviour of Be is also dependent on pH and the composition of solid and liquid (Aldahan et al., 1999; Boschi and Willenbring, 2016; You et al., 1989). Although pH ranges from 7.76 to 8.24 in our study area, numerous studies on the sorption behaviour of Be under different pH conditions have shown that no further adsorption-desorption occurs at pH values of approximately 7 to 9 (de Bruin et al., 1963; You et al., 1989; Zhao et al., 2022). This suggests that the pH-associated adsorption-desorption process is unlikely the dominate process regulating the dissolved ^9Be behaviour in the higher-salinity stratified zone.

3.4.3.2 Colloidal flocculation-deflocculation

Colloidal flocculation has been invoked to cause removal of particle-reactive elements at low salinity. When river water starts mixing with seawater, the seawater cations will reduce the negative surface-charge of riverine nanoparticles and colloids, inducing flocculation (Boyle et al., 1977). This phenomenon has been widely investigated in the laboratory and field (Andersson et al., 2001; Coffey et al., 1997; Merschel et al., 2017; Rousseau et al., 2015; Sholkovitz and Szymczak, 2000). Since adsorption of ^{9}Be onto SPM evidently does not control the removal of dissolved ^{9}Be in the Changjiang Estuary (section 3.4.3.1), we suggest that the salt-induced colloidal flocculation is likely the predominant driver of low-salinity removal of dissolved ^{9}Be, as shown for other particle-reactive elements such as Fe and REEs in the Changjiang Estuary (Wang and Liu, 2003; Wang and Liu, 2008).

In contrast, the colloidal deflocculation seems unlikely to account for the release of ^{9}Be at mid-salinity. Wang and Liu (2003) suggested that the release of Fe and REEs at mid-salinity in the Changjiang Estuary might result from intense sediment re-suspension, potentially leading to desorption and/or disruption of the coagulation process. However, we observe no correlation between $\Delta[^{9}Be]$ and SPM concentration, i.e., neither across the entire salinity range, nor within specific ranges, such as the mid-salinity range (Fig 3.9a). Note that this absent correlation between $\Delta[^{9}Be]$ and SPM concentration also implies that the Be scavenging rate is not a function of increased SPM concentrations as suggested by Li et al. (2021).

In summary, our results suggest that the removal of dissolved ^{9}Be at low salinity is likely caused by salt-induced colloidal flocculation, consistent with other particle-reactive elements. The release of dissolved ^{9}Be at mid-salinity however cannot be associated with colloidal deflocculation or ^{9}Be desorption (see section 3.4.3.1). We thus next inspect the role of benthic processes in controlling the release of ^{9}Be in this salinity range.

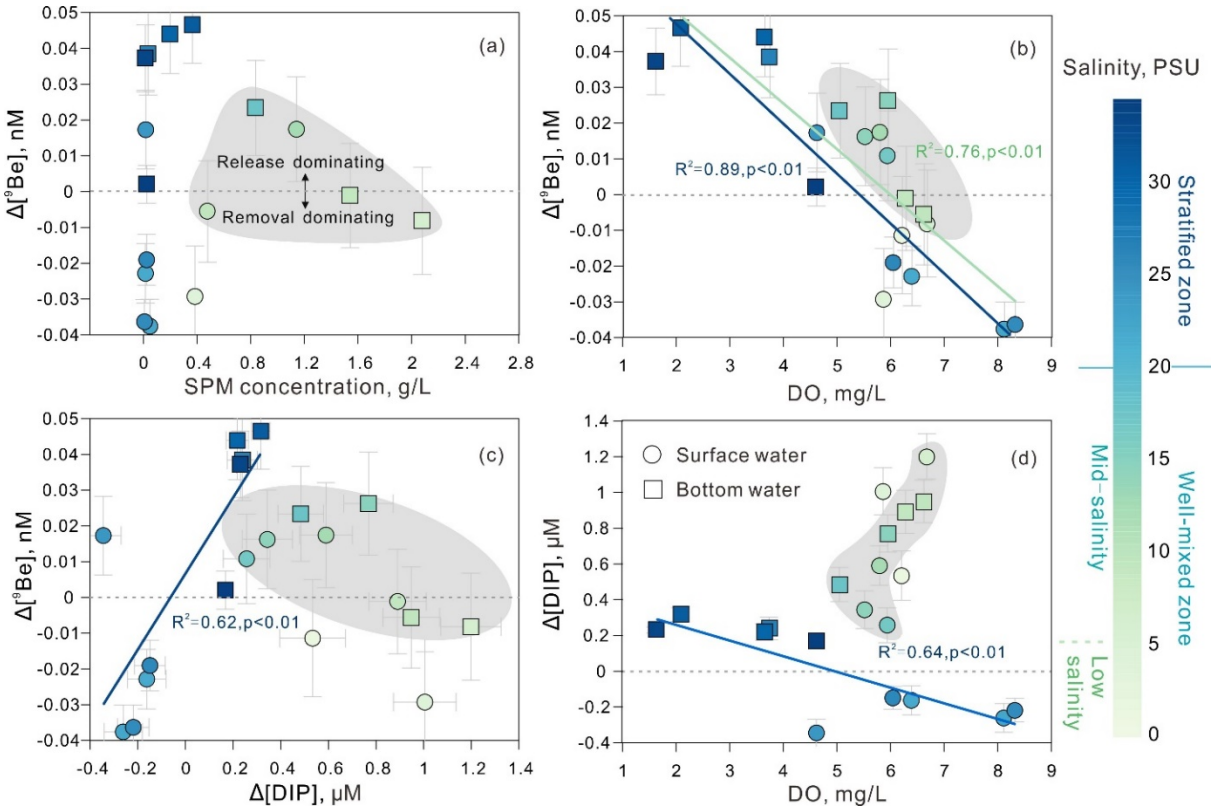

Figure 3.9 Δ[^{9}Be] color-coded for salinity vs. (a) SPM concentration, (b) DO (dissolved oxygen), (c) Δ[DIP] (bio-chemically altered fraction of dissolved inorganic phosphorus), and (d) Δ[DIP] vs. DO. SPM concentration data are not available for some stations. The DIP data are from Xu et al. (2021). The Δ[DIP] are calculated according to supplemental eqs. 1-5 with [DIP] substituted for [^{9}Be]. The grey shaded area indicates data from the mid-salinity range, the green line represents the regression results for all data points (excluding those from the low salinity zone, as there, [^{9}Be] are considered to be influenced by colloidal flocculation), and the dark blue line represents regressions only for data from the stratified zone (S>20 PSU).

3.4.3.3 Redox-related benthic Be flux at mid and high salinities

We observe a significant inverse correlation between Δ[^{9}Be] and dissolved oxygen (DO) at mid-high salinities (indicated by the green line in Fig. 3.9b), as well as in the high salinity region (i.e., the stratified zone, indicated by the dark blue line). Moreover, we also note a positive correlation between Δ[^{9}Be] and Δ[DIP] (bio-chemically altered fraction of dissolved inorganic phosphorus) (Fig. 3.9c), together with an inverse correlation between Δ[DIP] and DO (Fig. 3.9d) in the stratified (blue line) zone. Similar to Δ[^{9}Be], negative values of Δ[DIP] indicate the removal of DIP, potentially attributed to biological utilization, whereas positive values indicate release, possibly originating from organic matter decomposition or reduction of iron (oxy)hydroxides. Hence, the pronounced correlations between Δ[^{9}Be] and Δ[DIP], as well as Δ[DIP] and DO (Fig. 3.9c, d) suggest that in the stratified zone: 1) higher DO levels in the surface waters are associated with the removal of both ^{9}Be and DIP, while 2) lower DO levels

in bottom waters appear to facilitate the release of ^{9}Be and DIP to the dissolved phase. From this pattern, we invoke that the dissolved ^{9}Be behaviour in the stratified zone is regulated by similar mechanisms as DIP. The related mechanisms we discuss now for 1) surface waters and 2) bottom waters in the stratified zone, respectively.

1) The removal of DIP from oxygen-rich surface waters of the stratified zone is considered to be the result of extensive DIP consumption due to phytoplankton blooms (Liu et al., 2022). This is further evidenced by higher chlorophyll-a concentrations observed in the same set of samples in this region (Xu et al., 2021). Although Be is not an essential nutrient for phytoplankton growth (Sunda, 2012), high biological productivity may facilitate the scavenging of Be (Kusakabe et al., 1990; Xu, 1994), resulting in the observed negative values for $\Delta[^{9}Be]$.

2) The release of ^{9}Be and DIP into low-oxygen bottom waters is likely regulated by reduction of Fe-Mn(oxy)hydroxides during early diagenesis, as evidenced by porewater profiles of ^{9}Be (Deng et al., 2023) and DIP (Liu et al., 2020) in the Changjiang estuary. It has been observed that elevated benthic P flux in the Changjiang estuary is associated with hypoxic conditions (Liu et al., 2020). A similar relationship may also exist for Be, given the significant inverse correlation between $\Delta[^{9}Be]$ and DO (Fig. 3.9b). Intensified hypoxic conditions, as evident by decreased DO in bottom water, may favour the diagenetic release of ^{9}Be in two ways:

i) Hypoxic conditions tend to shift the oxygen penetration depth upwards in the sediment column, potentially allowing the elevated dissolved [^{9}Be] in reduced porewaters to be present close to the sediment-water interface (Fig. 3.10 column A and B). This would lead to a more efficient upward migration of dissolved ^{9}Be released from sediments to overlying water, as observed for other trace metals (Liu et al., 2022; Shi et al., 2019). Such behaviour is further supported by observations from dissolved [Fe], [Mn] and [Nd] in porewater profiles along the Changjiang-Estuary-Shelf Transect (Deng et al., 2022), where maximum concentrations were observed at shallower depths (~5 cm) for station C13 (in the centre of the hypoxia zone), whereas for the well-oxygenated C6-1 station, concentration maxima occurred at a much deeper depths of >20 cm (Deng et al., 2022).

ii) Low oxygen levels, together with low pH and low temperatures in the bottom seawater (Fig. 3.2), may markedly slow down the oxidation rate of released Fe(II) and Mn(II) in porewater during early diagenesis (Lohan and Bruland, 2008; Millero et al., 1987; Sunda and Huntsman, 1987). A consequence would be that less Fe-Mn (oxy)hydroxides are formed that are able to scavenge released dissolved ^{9}Be during its upward migration from porewater into the water column (Fig. 3.10 column A and B).

We suggest that the release of ^{9}Be at mid-salinity is dominated by the same benthic processes as observed in bottom waters of the stratified zone, since other processes including colloidal

deflocculation or ^{9}Be desorption have been ruled out. Unlike in the stratified zone where benthic sources only contribute to bottom waters due to the strong water stratification, the release of ^{9}Be at mid-salinity is impacting $[^{9}Be]_{diss}$ in both surface and bottom waters. This is likely a consequence of strong vertical water mixing at mid-salinity, as in this region the turbidity maximum zone developed (Fig. 3.10). The effect is similar to what we observed at C11 station where upwelling led to ^{9}Be in surface water that is identical to bottom water.

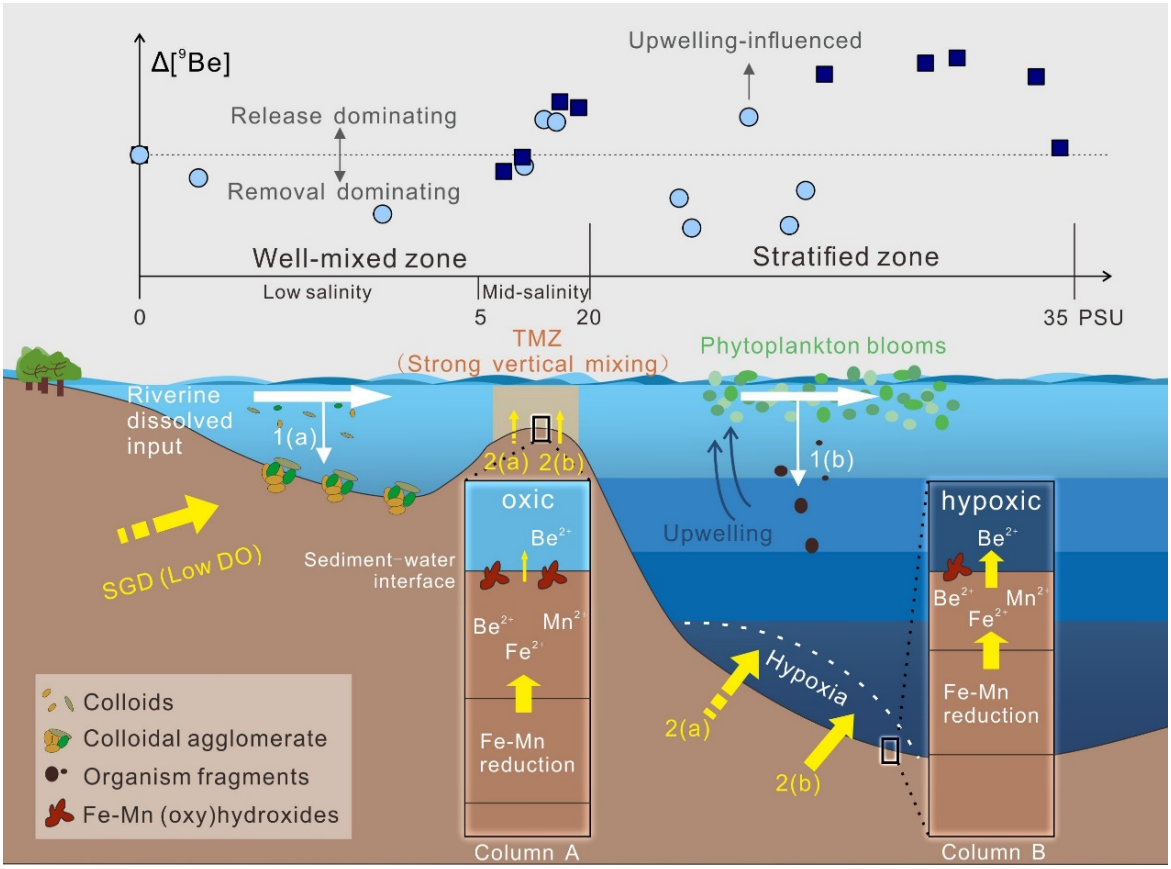

Figure 3.10 Schematic illustration of different pathways of dissolved ^{9}Be through the Changjiang Estuary into the ocean. TMZ: turbidity maximum zone; SGD: submarine groundwater discharge; DO: dissolved oxygen. The white arrow represents the riverine dissolved ^{9}Be input and two associated removal processes are indicated as: 1(a) colloidal flocculation, 1(b) biological scavenging. Yellow arrows represent potential benthic pathways supplying ^{9}Be into water: 2(a) SGD (dashed arrow) and 2(b) porewater diffusion/expulsion (solid arrow). The thickness of the yellow arrow scales with the magnitude of the flux. Column A- oxic conditions in TMZ; column B- hypoxic conditions at high salinities

In addition to the diagenetic release of ^{9}Be, another potential benthic contributor could be the submarine groundwater discharge (including fresh groundwater, re-circulating seawater and a composite of the two), which is considered an important source of nutrients (e.g., DIP) to the coastal ocean (Wang et al., 2018). On the other hand, submarine groundwater discharge may also contribute to the formation of hypoxic zones (Guo et al., 2020), as it is characterized by

lower DO levels resulting from substantial organic matter decomposition and oxygen isolation (Gagan et al., 2002). As a result, the elevated Δ[^{9}Be] under low DO conditions along the Changjiang-Estuary-Shelf Transect could potentially be attributed to an increase in submarine groundwater discharge. Although [^{9}Be] data are not available for the groundwater end-member in the study area, reported [^{9}Be] in groundwater tend to be higher than in river water (Dannhaus et al., 2018; Shravanraj et al., 2021; Vesely et al., 2002). Thus, it is possible that submarine groundwater discharge also plays a role in contributing excess dissolved ^{9}Be into the water column.

To summarize, in light of the strong correlations between Δ[^{9}Be] and DO, as well as Δ[DIP] in the stratified zone, we propose that the benthic flux is the main contributor to the release of ^{9}Be at mid-salinity and into bottom waters of the stratified zone. Possible processes include porewater diffusion/expulsion and submarine groundwater discharge. The enhanced benthic flux of ^{9}Be seems to occur in the hypoxic zone. In contrast, the removal of ^{9}Be from surface waters of the stratified zone is likely a result of biological scavenging facilitated by phytoplankton blooms.

3.4.4 Implications for ^{9}Be pathways into oceans

The complex behaviour of dissolved ^{9}Be along the Changjiang-Estuary-Shelf Transect implies the co-existence of different pathways of terrigenous ^{9}Be input into the ocean. In addition to the two major pathways proposed by von Blanckenburg and Bouchez (2014) and (von Blanckenburg et al., 2015; von Blanckenburg et al., 2022), i.e., dissolved riverine ^{9}Be fluxes escape coastal scavenging (path 1) and reactive riverine particulate-bound ^{9}Be is released from bottom sediment into seawater (path 2), our exchangeable ^{9}Be data suggest a rapid desorption of ^{9}Be from SPM through cation exchange at the onset of estuarine mixing (Fig. 3.8). However, the ^{9}Be input through this path is negligible relative to the overall ocean Be budget, as the exchangeable ^{9}Be carried by riverine SPM is two orders of magnitude lower than that in the dissolved phase (Fig. 3.6, S=0). With respect to path 1, we suggest that colloidal flocculation occurring at low-salinity and biological scavenging resulting from seasonal phytoplankton blooms may modify the ^{9}Be input through this pathway, whereas increases in SPM concentrations do not necessarily promote ^{9}Be scavenging in contrast to the hypothesis of Li et al., (2021). With respect to path 2, our data offer additional support for the benthic contribution of ^{9}Be into coastal seawater. This benthic ^{9}Be flux is likely associated with the reduction of Fe-Mn (oxy)hydroxides during early diagenesis, in alignment with findings derived from pore water ^{9}Be profiles (Deng et al., 2023), but could potentially involve a contribution from submarine groundwater discharge. Moreover, the hypoxia-anoxia conditions in bottom waters may enhance the diagenetic release of ^{9}Be.

Quantifying the relative contributions of the above-mentioned two major pathways to the oceanic ^{9}Be budget is key to establishing ^{10}Be/^{9}Be as a quantitative paleo-weathering proxy. Our data shows that the reactive particulate ^{9}Be pool (i.e., $^{9}Be_{reac}$) transported into coastal ocean is more than 100 times higher than the riverine dissolved pool (Fig. 3.6, S=0). This means that even if only 1% of ^{9}Be is released from the sediment during early diagenesis, this flux will be comparable to or even exceed the dissolved flux (prior to the coastal trap). Using compiled riverine dissolved ^{9}Be fluxes (Deng et al., 2023) and the average estuarine removal rate (56%) (Suhrhoff et al., 2019), Deng et al., (2023) calculated that about $1.8 \pm 0.4 \times 10^{7}$ mol/year of ^{9}Be is delivered to the ocean via path 1,accounting for less than 30% of the total oceanic Be input. In this calculation, the average estuarine removal (56%) is estimated from previously published ^{9}Be data in surface waters of six estuaries and their removal/release behaviour compared to conservative mixing (Suhrhoff et al., 2019). However, our data shows that the surface water-derived ^{9}Be signal could be altered by benthic contribution in a vertically well-mixed estuary, such as the mid-salinity range in the Changjiang Estuary. This would lead to an underestimation of the estuarine removal extent, suggesting that the actual input of riverine dissolved ^{9}Be into the ocean (path 1) may be even lower than currently estimated. In turn, this suggests that benthic fluxes (path 2) could play an even more important role. If paleo-marine ^{10}Be/^{9}Be records are primarily controlled by changes in benthic ^{9}Be fluxes, ultimately changes in sediment and organic carbon delivery, as well as sea-level fluctuations that regulate the extent of diagenesis might be first-order controlling mechanisms (Deng et al., 2023). Given that the reduction of Fe-Mn-oxy-hydroxides during diagenesis is likely linked to oxygen levels in the benthic realm, changes in paleoredox could also be a key factor. On the other hand, a contribution of submarine groundwater discharge as part of the benthic flux cannot be ruled out in regulating dissolved ^{9}Be concentrations. submarine groundwater discharge may constitute another significant, yet unexplored, source to the marine ^{9}Be budget. Therefore, identifying the various factors that govern benthic ^{9}Be flux and assessing their relative significance will be critical for firmly deciphering paleo-oceanic ^{10}Be/^{9}Be records.

3.5 Summary and outlook

We identify three different pathways and the underlying mechanisms for the transport of terrigenous ^{9}Be into the ocean through the Changjiang Estuary, based on systematic data for particulate and dissolved ^{9}Be along the entire salinity transect. These pathways include: 1) riverine dissolved input, 2) ^{9}Be desorption from the suspended particulate matter (SPM), and 3) coastal benthic inputs which involve porewater diffusion and/or submarine groundwater discharge. Regarding these pathways, we show that

1) The riverine dissolved ^{9}Be flux is reduced during estuarine mixing due to colloidal flocculation and biological scavenging resulting from seasonal phytoplankton blooms. To derive the actual riverine dissolved ^{9}Be flux to the ocean that survives the coastal trap, surface

dissolved ^{9}Be data along the salinity gradient is unlikely to provide a complete quantification, because the ^{9}Be in surface waters can be altered by benthic contributions in vertically well-mixed zones.

2) The ^{9}Be flux derived from desorption from SPM through rapid cation exchange is negligible, as the exchangeable ^{9}Be pool on riverine SPM is two orders of magnitude lower than the dissolved ^{9}Be pool.

3) Benthic ^{9}Be fluxes play a crucial role in controlling the paleo-marine ^{10}Be/^{9}Be record. For a robust interpretation of oceanic ^{10}Be/^{9}Be records, a more extensive investigation of the magnitude of the benthic ^{9}Be flux in diverse environments, as well as the role of submarine groundwater discharge are now required.

3.6 Supplementary material

Three-endmember mixing model

Using a three-endmember mixing model assuming conservation of potential temperature and salinity, the fractional water contributions from each of the three endmembers are calculated following:

$$f_{CDW} + f_{TWCSW} + f_{TWCDW} = 1 \quad (S3.1)$$

$$f_{CDW}\theta_{CDW} + f_{TWCSW}\theta_{TWCSW} + f_{TWCDW}\theta_{TWCDW} = \theta_{sample} \quad (S3.2)$$

$$f_{CDW}S_{CDW} + f_{TWCSW}S_{TWCSW} + f_{TWCDW}S_{TWCDW} = S_{sample} \quad (S3.3)$$

where f_{CDW}, f_{TWCSW}, and f_{TWCDW} denote the fractional water contribution from the Changjiang Diluted Water (CDW), the Taiwan Warm Current Surface Water (TWCSW) and Taiwan Warm Current Deep Water (TWCDW), respectively. The symbols θ and S represent potential temperature and salinity for each endmember and sample. The θ and S for each endmember are listed in Table S3.1. The theoretical conservative concentration of dissolved ^{9}Be (i.e. $[^9Be]_{conservative}$, in nM) is given by the following equation:

$$[\,^9Be]_{conservative} = [\,^9Be]_{CDW}f_{CDW} + [\,^9Be]_{TWCSW}f_{TWCSW} + [\,^9Be]_{TWCDW}f_{TWCDW} \quad (S3.4)$$

where $[\,^9Be]_{CDW}$, $[\,^9Be]_{TWCSW}$ and $[\,^9Be]_{TWCDW}$ represent the dissolved ^{9}Be concentration in the CDW, TWCSW and TWCDW, respectively. From knowing $[^9Be]_{conservative}$, the difference to $[^9Be]_{measured}$ value is the so-called $[^9Be]_{diff}$ (in nM), i.e., the difference between field values ($[^9Be]_{measured}$) and model-predicted values. $[^9Be]_{diff}$ can be calculated as follow:

$$\Delta[\,^9Be] = [\,^9Be]_{measured} - [\,^9Be]_{conservative} \quad (S3.5)$$

We employed the same set of equations to calculate the $[DIP]_{diff}$ (bio-chemically altered fraction of dissolved inorganic phosphorus, DIP, section 3.4.3.3 in main text), by substituting $[^9Be]$ for [DIP] in equations S3.1-S3.5. Uncertainties on $\Delta[^9Be]$ and Δ[DIP] were estimated by propagating uncertainties of the measured sample and the three endmembers.

Table S3.1 Potential temperature, salinity, and dissolved ^{9}Be and inorganic phosphorus concentrations of the different endmembers.

	Potential temperature (°C)	Salinity (PSU)	[^{9}Be] (nM)	[DIP] (μM)
Changjiang Diluted Water (CDW)	28.9	0	0.14±0.01	0.60±0.14
Taiwan Warm Current Surface Water (TWCSW)	29.4	32.0	0.03±0.003	0.03
Taiwan Warm Current Deep Water (TWCDW)	20.1	34.6	0.05±0.005	0.71

The CDW endmember values are derived from average values of fresh water samples (C1-C5, N=6) with an uncertainties of 1 SD. The values for TWCSW and TWSDW are derived from measured values of surface water at station C18, and bottom water at station C16, respectively. The analytical uncertainty for [^{9}Be] is 10%, while the analytical uncertainties for [DIP], potential temperature and salinity are negligible (<1%).

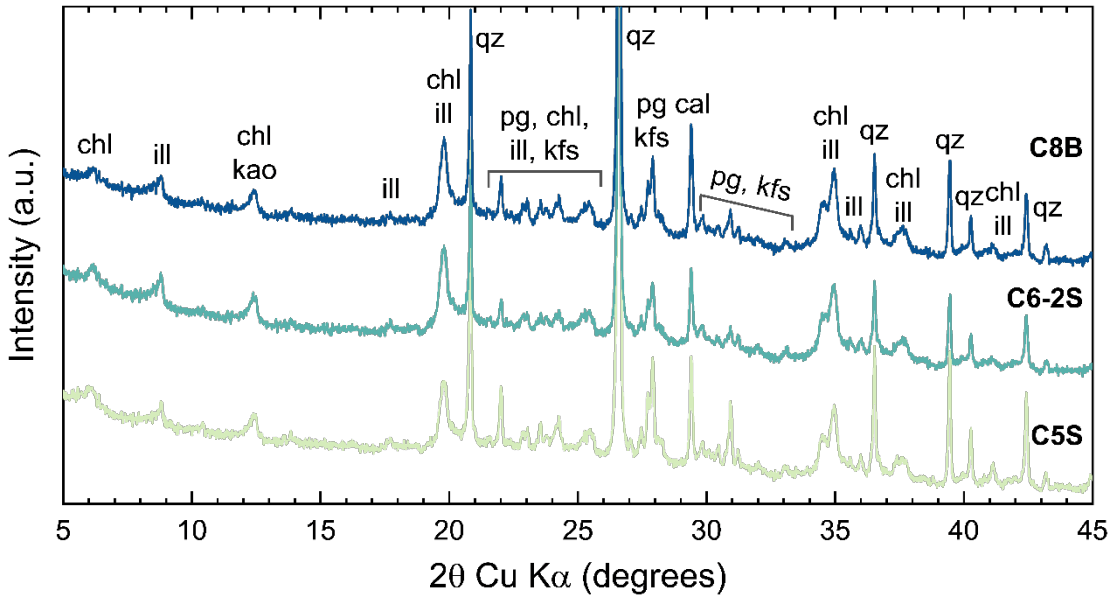

Fig. S3.1 Powder X-ray diffraction (XRD) pattern of selected SPM samples with representative salinity: C5S (S=0 PSU), C6-2S (S= 4.1 PSU), C8B (S= 14.9 PSU). Phases identified include quartz (qz), plagioclase (albite-rich, pg), k-feldspar (microcline-rich, kfs), sheet silicates (chlorite – chl, illite – ill, kaolinite – kao) and calcite (cal).

Table S3.2 ^{9}Be concentrations (compared to bulk samples (in µg/g) and per volume of seawater (in nM), respectively) and major elemental concentrations (compared to bulk samples) in sequentially extracted fractions of suspended particulate matter in the Changjiang Estuary.

Sample ID	Extracted fraction	^{9}Be (µg/g)	^{9}Be (nM)	Al (µg/g)	Ca (µg/g)	K (µg/g)	Mg (µg/g)	Na (µg/g)	Mn (µg/g)	Fe (µg/g)
C5S_SPM	Ex	0.12	0.002	1.23	4700	130	350	26	81	b.d.
	Reac	0.64	13.98	3800	21000	330	8300	52	820	11000
	Org	0.04	0.82	330	180	37	190	b.d.	b.d.	135
	Min	1.38	30.17	68000	2400	20000	9900	6800	150	29000
C5B_SPM	Ex	0.12	0.003	1.47	5100	110	310	26	56	b.d.
	Reac	0.60	18.53	3600	21000	320	8100	51	780	11000
	Org	0.03	1.01	280	170	34	170	b.d.	b.d.	120
	Min	1.41	43.33	68000	2800	20000	9800	8000	160	29000
C6-1S_SPM	Ex	0.08	n.d.	1.18	4900	240	830	85	41	b.d.
	Reac	0.73	n.d.	4400	16000	590	8700	91	770	12000
	Org	0.02	n.d.	n.d.	n.d.	n.d.	n.d.	n.d.	n.d.	n.d.
	Min	n.d.	n.d.	n.d.	n.d.	n.d.	n.d.	n.d.	n.d.	n.d.
C6-2S_SPM	Ex	0.08	0.003	1.59	6500	350	1300	340	60	b.d.
	Reac	0.84	35.17	4600	16000	710	10000	200	840	13000
	Org	0.04	1.79	350	160	61	230	b.d.	b.d.	110
	Min	1.63	68.78	82000	1500	23000	12000	5100	160	35000

Continued

Sample ID	Extracted fraction	^{9}Be (µg/g)	^{9}Be (nM)	Al (µg/g)	Ca (µg/g)	K (µg/g)	Mg (µg/g)	Na (µg/g)	Mn (µg/g)	Fe (µg/g)
C6-2B_SPM	Ex	0.08	0.019	1.55	5900	340	1200	300	64	b.d.
	Reac	0.77	175.89	4300	18000	650	8500	170	830	13000
	Org	0.04	9.06	320	170	56	210	b.d.	b.d.	108
	Min	1.49	340.17	77000	1900	22000	11000	5900	170	32000
C6-3S_SPM	Ex	0.08	0.004	1.38	5500	300	1100	350	61	b.d.
	Reac	0.70	36.54	4100	20000	630	9000	180	840	12000
	Org	0.04	1.98	290	150	54	200	b.d.	b.d.	99
	Min	1.50	78.89	75000	2200	21000	11000	7200	160	32000
C6-3B_SPM	Ex	n.d.	n.d.	n.d.	n.d.	n.d.	n.d.	n.d.	n.d.	n.d.
	Reac	0.65	109.40	3700	20000	560	8000	160	780	11000
	Org	0.03	5.62	280	120	47	170	b.d.	b.d.	110
	Min	1.47	248.22	72000	3600	21000	11000	7400	160	31000
C8S_SPM	Ex	0.04	n.d.	1.06	3800	360	1300	650	89	b.d.
	Reac	0.64	n.d.	3500	20000	620	7700	110	770	11000
	Org	n.d.	n.d.	n.d.	n.d.	n.d.	n.d.	n.d.	n.d.	n.d.
	Min	1.34	n.d.	68000	2100	18000	9100	6000	170	25000

Continued

Sample ID	Extracted fraction	^{9}Be (µg/g)	^{9}Be (nM)	Al (µg/g)	Ca (µg/g)	K (µg/g)	Mg (µg/g)	Na (µg/g)	Mn (µg/g)	Fe (µg/g)
C8B_SPM	Ex	n.d.	n.d.	n.d.	n.d.	n.d.	n.d.	n.d.	n.d.	n.d.
	Reac	0.65	n.d.	3700	19000	640	7700	110	780	11000
	Org	n.d.	n.d.	n.d.	n.d.	n.d.	n.d.	n.d.	n.d.	n.d.
	Min	1.22	n.d.	61000	1800	16000	8100	5200	150	23000
C9B_SPM	Ex	n.d.	n.d.	n.d.	n.d.	n.d.	n.d.	n.d.	n.d.	n.d.
	Reac	0.66	60.51	3700	18000	720	7600	130	750	11000
	Org	n.d.	n.d.	n.d.	n.d.	n.d.	n.d.	n.d.	n.d.	n.d.
	Min	1.45	133.23	75000	1500	21000	10000	5000	190	29000
C10B_SPM	Ex	n.d.	n.d.	n.d.	n.d.	n.d.	n.d.	n.d.	n.d.	n.d.
	Reac	0.66	2.55	3700	20000	770	8000	120	690	11000
	Org	n.d.	n.d.	n.d.	n.d.	n.d.	n.d.	n.d.	n.d.	n.d.
	Min	1.40	5.42	72000	1800	20000	9700	9700	180	28000

The unit for ^{9}Be concentration in the "Ex" fraction, calculated relative to initial the mass of the initial bulk sample) is ng/g.

^{9}Be concentration in per volume of seawater (in nM) is calculated by forming the product of [^{9}Be] in each fraction (ng/g or µg/g) times the SPM concentration (in g/L).

n.d. = not determined, b.d. = below detection limit.

A 10% uncertainty is given for ^{9}Be concentration in the "Ex" fraction that represents the long-term recovery for iron co-precipitation method and a relative uncertainty of 5% is applied for all the other element measurements that represents the long-term repeatability for ICP-OES measurements.

Table S3.3 Specific surface area of the suspended particulate matter in the Changjiang Estuary and the surface area normalized ^{9}Be concentration ($[^{9}Be]_{ex_normalized}$) in the exchangeable fraction. The uncertainty of $[^{9}Be]_{ex\_normalized}$ is propagated from the analytical uncertainties for $[^{9}Be]_{ex}$ and specific surface area.

Sample ID	Surface area (m^2/g)	Surface area normalized $[^{9}Be]_{ex}$ ($pmol/m^2$)
C5S_SPM	17.94	0.71 ± 0.07
C5B_SPM	16.14	0.82 ± 0.08
C6-1S_SPM	27.52	0.30 ± 0.03
C6-2S_SPM	27.26	0.31 ± 0.03
C6-2B_SPM	22.27	0.41 ± 0.04
C6-3S_SPM	21.94	0.40 ± 0.04
C6-3B_SPM	20.61	n.d.
C8S_SPM	22.83	0.22 ± 0.02
C8B_SPM	23.37	n.d.
C9B_SPM	27.92	n.d.
C10B_SPM	n.d.	n.d.

n.d. = not determined

Table S3.4 The difference of measured dissolved ^{9}Be and dissolved inorganic phosphorus (DIP) concentrations relative to conservative-mixing values, termed (Δ[^{9}Be]). Uncertainties for Δ[^{9}Be] and Δ[DIP] are propagated from the uncertainties for three endmembers and the analytical uncertainty for each sample.

Sample ID	Salinity (PSU)	Δ[^{9}Be] (nM)	Δ[DIP] (μM)
C1S	0.0	0	0
C1B	0.0	0	0
C3S	0.0	0	0
C3B	0.0	0	0
C5S	0.0	0	0
C5B	0.0	0	0
C6-1S	1.0	-0.011 ± 0.016	0.64 ± 0.14
C6-2S	4.1	-0.029 ± 0.014	0.62 ± 0.13
C6-2B	6.2	-0.008 ± 0.015	0.61 ± 0.13
C6-3S	9.4	-0.006 ± 0.014	0.60 ± 0.12
C6-3B	9.1	-0.001 ± 0.015	0.60 ± 0.12
C7S	12.5	0.017 ± 0.015	0.52 ± 0.11
C8S	14.4	0.016 ± 0.014	0.47 ± 0.11
C8B	14.9	0.026 ± 0.014	0.46 ± 0.10
C9S	16.9	-0.002 ± 0.013	0.84 ± 0.10
C9B	17.8	0.023 ± 0.013	0.47 ± 0.10
Boundary between well-mixed zone and stratified zone			
C10S	21.9	-0.023 ± 0.008	0.39 ± 0.08
C10B	26.7	0.038 ± 0.011	0.45 ± 0.06
C11S	24.2	0.017 ± 0.011	0.56 ± 0.08
C11B	30.0	0.044 ± 0.011	0.52 ± 0.05
C12S	22.3	-0.038 ± 0.008	0.41 ± 0.08
C12B	31.0	0.047 ± 0.011	0.47 ± 0.04
C13S	26.0	-0.019 ± 0.007	0.37 ± 0.06
C13B	33.6	0.037 ± 0.009	0.57 ± 0.02
C16S	25.5	-0.036 ± 0.006	0.30 ± 0.07
C16B	34.6	0	0
C18S	32.0	0	0
C18B	34.4	0.002 ±	0.41 ±0.00

Chapter 4 ^{10}Be(meteoric)/^{9}Be at the land-ocean interface: implications for boundary exchange processes and paleo-denudation rate reconstruction

Abstract

Beryllium isotopes at the land-ocean interface are tracers for input of trace metals into seawater and exchange processes at continental margins. To explore the mechanisms (or chemical behaviour) of these isotopes at this boundary we systematically measured meteoric cosmogenic ^{10}Be and stable ^{9}Be concentrations in water, suspended particles, and bottom sediments from the mouths of the Changjiang and Amazon rivers to the outer continental shelves across the entire salinity gradients. We found that both dissolved ^{9}Be and ^{10}Be behave non-conservatively during estuarine mixing. In contrast, the ^{10}Be/^{9}Be ratios of dissolved Be generally follow the conservative mixing line, except where hypoxic bottom waters are affected by submarine groundwater discharge. For the ^{10}Be/^{9}Be measured in authigenic (reactive) suspended and bottom sediment phases relative to those from riverine freshwater, no significant change in the ^{10}Be/^{9}Be is observed within 150 km from both coasts, indicating that the continental ^{10}Be/^{9}Be signature is preserved in this zone. Beyond this zone where boundary currents prevail, authigenic ^{10}Be/^{9}Be of outer-shelf/slope sediments markedly increase by a factor of 3 to 30 along with ^{10}Be/^{9}Be in bottom seawater. We attribute the shift in ^{10}Be/^{9}Be in outer-shelf/slope sediments to water-sediment interactions through “boundary exchange” processes. From the reactive ^{10}Be/^{9}Be of inner-shelf sediments preserving the continental signal, we calculate the denudation rates for the entire Changjiang and Amazon catchments and compare them with *in situ* beryllium isotope-estimates from each catchment. Our results verify that in large river-dominated shelves characterized by high sedimentation rates and weakened shoreward diffusion of seawater, the ^{10}Be/^{9}Be ratio in reactive phases of coast-proximal sediments can be a direct recorder of terrigenous denudation of the adjacent river catchments.

4.1 Introduction

The marine authigenic $^{10}Be/^{9}Be$ ratio has been applied as a tracer for deep marine circulation (von Blanckenburg et al., 1996), sea ice dynamics (e.g., Rhee et al., 2022; Sproson et al., 2022; White et al., 2019) and past continental weathering fluxes (e.g., Caves Rugenstein et al., 2019; von Blanckenburg and Bouchez, 2014; von Blanckenburg et al., 2015; Willenbring and von Blanckenburg, 2010a). It has also been used to constrain chronologies of marine sediments and ^{10}Be production changes resulting from variations of Earth's magnetic field (e.g., Carcaillet et al., 2004; Christl et al., 2003; Knudsen et al., 2008; Ménabréaz et al., 2014; Simon et al., 2018; Simon et al., 2020). The meteoric radioactive ^{10}Be is produced in the upper atmosphere via spallogenic reactions between secondary cosmic radiation and target nuclei in the atmosphere and is delivered to the Earth's surface and oceans by wet and dry deposition (Lal and Peters, 1967). Its stable counterpart ^{9}Be is released from rocks by chemical weathering and is transferred to the oceans mainly by rivers in both dissolved and particulate phases, while aeolian input only plays a minor role for the modern oceanic ^{9}Be budget (von Blanckenburg et al., 1996). Due to the particle-reactive nature of Be, more than 90% of riverine Be (^{9}Be and ^{10}Be) are trapped in the coastal area when transported to the oceans via rivers (von Blanckenburg and Bouchez, 2014). In the oceans, riverine input is the dominant source for ^{9}Be, while almost all meteoric ^{10}Be is sourced from atmospheric precipitation. The distinct sources of these two isotopes lead to an increase in the $^{10}Be(meteoric)/^{9}Be$ ratio from $\sim 1\times10^{-9}$ to 1×10^{-8} in rivers to $>4\times10^{-8}$ in oceans (Bourlès et al., 1989a; Brown et al., 1992b; Frank et al., 2009; Kong et al., 2021b; Ku et al., 1990; Kusakabe et al., 1987; Measures et al., 1996; von Blanckenburg and Igel, 1999).

Continental margins, where the significant increase in $^{10}Be/^{9}Be$ ratio from rivers to oceans occurs, are regions characterized by efficient exchange of water, chemical species and particulate matter (Chen et al., 2003; Walsh, 1991). Intensified scavenging of particle-reactive isotopes such as ^{10}Be, ^{210}Pb, ^{231}Pa and ^{230}Th has been widely observed at ocean margins, in a process known as "boundary scavenging". Other than "boundary scavenging", these marginal regions also act as an important source of many elements to the oceans, the net land–ocean inputs of these elements thus result from both removal and release processes occurring at the land-ocean interface, named "boundary exchange" (Jeandel et al., 2007; Lacan and Jeandel, 2005). Conceptually, "boundary exchange" comprises all processes occurring at land–ocean interface that lead to the removal/release of elements from/into seawater (Jeandel, 2016). In addition to modifying the marine elemental budget, it can also alter the isotopic composition in ocean bottom waters as well as that recorded in the authigenic fraction of sediments, thus complicating the application of these isotope tracers in palaeoceanographic and paleoenvironmental reconstructions. For these reasons, "boundary exchange" processes have received increasing attention in recent years, in particularly for radiogenic isotopes, such as neodymium (Nd) and lead (Pb) (e.g., Adebayo et al., 2022; Chen et al., 2023; Jang et al., 2017;

Jeandel and Oelkers, 2015; Molina-Kescher et al., 2014; Wang et al., 2022; Wilson et al., 2015). Among the many isotope ratio proxies in use to investigate "boundary exchange", the much overlooked $^{10}Be/^{9}Be$ ratio offers particular advantages: Its nature is particle-reactive, it is strongly cycled within pore-waters on shelves (Bourlès et al., 1989b; Deng et al., 2023) and has a significant difference (i.e., about one to two orders of magnitude) between riverine and marine $^{10}Be/^{9}Be$ signatures.

Previous studies on the distribution of $^{10}Be/^{9}Be$ at the land-ocean interface mainly focus either on dissolved $^{10}Be/^{9}Be$ or particulate $^{10}Be/^{9}Be$ in ocean bottom sediments (Brown et al., 1992b; Kong et al., 2021b; Kusakabe et al., 1991; Sarathi Jena et al., 2022; Simon et al., 2016; Wittmann et al., 2017). These studies have shown that $^{10}Be/^{9}Be$ ratios at marginal sites, whether in dissolved or sedimentary authigenic phases, are noticeably lower than that in the adjacent open ocean (Kong et al., 2021b; Sarathi Jena et al., 2022; Simon et al., 2016) but higher than that in adjacent rivers (Wittmann et al., 2017). However, variations in dissolved and particulate $^{10}Be/^{9}Be$ along the entire salinity gradient at continental margins and the underlying control mechanisms still remain unexplored. Addressing these questions is not only beneficial for our understanding of "boundary exchange" processes, but also holds significant importance for identifying the oceanic environment in which authigenic $^{10}Be/^{9}Be$ ratios can be used to faithfully reconstruct continental weathering fluxes on regional and global ocean-basin scales (von Blanckenburg and Bouchez, 2014), or the ^{10}Be - production changes resulting from changes Earth's magnetic field strength (Savranskaia et al., 2021; Simon et al., 2016).

In this study, we systematically examine $^{10}Be/^{9}Be$ ratios in both surface and bottom coastal waters, as well as in chemically extracted authigenic fractions of suspended sediments and ocean bottom sediments from two of the world's largest river estuaries, the Changjiang and Amazon estuaries. We provide the first complete dissolved and particulate $^{10}Be/^{9}Be$ profiles along the entire salinity gradient, from the river mouth to the outer shelf/slope. The paired water and sediment samples allow us to investigate "boundary exchange" processes and their potential effects on $^{10}Be/^{9}Be$ ratios recorded in coastal seawater and authigenic phases of bottom sediments. Finally, we investigate the possibility of using coast-proximal sites sediments to trace present and past denudation rates of the adjacent river catchments.

4.2 Study area, materials and methods

4.2.1 Study area

The Changjiang (Yangtze) River, ranked among the world's largest rivers, flows 6300 km eastwards from Tibetan Plateau into the East China Sea (ECS). The catchment covers an area of ~1.8×10^{6} km^2 and supports a population of ca. 450 million people (Yang et al., 2005). It historically delivered ~900 km^3/yr of water and ~470 Mt/yr of sediment into the East China Sea (Milliman and Farnsworth, 2011). Due to dam construction, reforestation and decreased

precipitation, the sediment load of the Changjiang had decreased by >60% since the 1970s (Dai and Lu, 2014; Xu and Milliman, 2009). The Changjiang Estuary is a mesotidal, partially mixed estuary, with a tide of regular semidiurnal type. Circulation in the Changjiang Estuary and the adjacent region is mainly governed by the Changjiang Diluted Water (CDW), Zhe-Min Coastal Current (ZMCC), and Taiwan Warm Current (TWC) (Su, 2001) (Fig. 4.1). The southward ZMCC is most active during winter, carrying water and sediments from the Changjiang River southward along the inner shelf (Beardsley et al., 1985; Lee and Chao, 2003). In summer, the northward TWC intensifies due to the prevailing southeast monsoon and largely weakens the southward transport of sediments along the coast (Beardsley et al., 1985; Lee and Chao, 2003). It is estimated that ~40% of the fluvial sediment is trapped in the estuary, and the remaining 60% is transported to the neighbouring continental shelf of the ECS by coastal currents (Liu et al., 2006; Milliman et al., 1985). Near the Changjiang mouth, the inner shelf (landward of the ~50 m isobath) is mainly composed of silts, clayey silts and silty clays (Liu et al., 2006; Luo et al., 2012). Towards the outer continental shelf, the modern riverine muds are replaced seawards by relict sands which are thought to have been deposited prior to the post-glacial sea-level rise that began 18 kyr BP (Luo et al., 2012; Wang et al., 1986).

The Amazon River is the world's largest fluvial system in terms of annual water discharge (~6600 km^3/yr, Callède et al. (2010)) and drainage area (~6.1×10^6 km^2), and presently exports a total sediment load of ~550-1500 Mt/yr to the Atlantic Ocean (Armijos et al., 2016; Dunne et al., 1998; Martinez et al., 2009; Meade et al., 1985). Its estuary is classified as macrotidal (Gallo and Vinzon, 2017) and semidiurnal (Kosuth et al., 2009) with a tidal range between 4 and 6 m at the mouth. The Amazon continental shelf is more than 300 km wide off the river mouth. The inner shelf is relatively flat and smooth to about the 40 m isobath (ca. 150 km seaward of the river mouth), where modern sediment (mainly compose of silt and clay) primarily accumulate (Kuehl et al., 1986; Kuehl et al., 1982; Nittrouer et al., 1983). The seabed abruptly steepens between the 40 m and 60 m isobaths, where the inner-shelf mud thins (Kuehl et al., 1986; Kuehl et al., 1982; Nittrouer et al., 1983). On the outer shelf (60-100 m water depth), a relict transgressive sand layer formed during low stands of sea level is exposed (Kuehl et al., 1986; Nittrouer et al., 1983). Further offshore, on the continental slope, sediments are again dominated by silty clay sourced from the Amazon River and contain a significant fraction of pelagic material (Spiegel et al., 2021). Circulation on the Amazon shelf is influenced by the interaction of the freshwater plume (Amazon outflow, AO) with strong tidal currents and the north-westward flowing North Brazilian Current (NBC) (Kineke et al., 1996; Rockwell Geyer et al., 1996) (Fig. 4.1). The NBC flows along the Amazon outer shelf and slope as a western boundary current 100-200 km wide and 500 m deep (Flagg et al., 1986). The highly dynamic current system on the Amazon shelf results in strong turbulence on the shelf sediments and frequent resuspension, which continuously rework up to 150 cm of the upper sediment package (Kuehl et al., 1986).

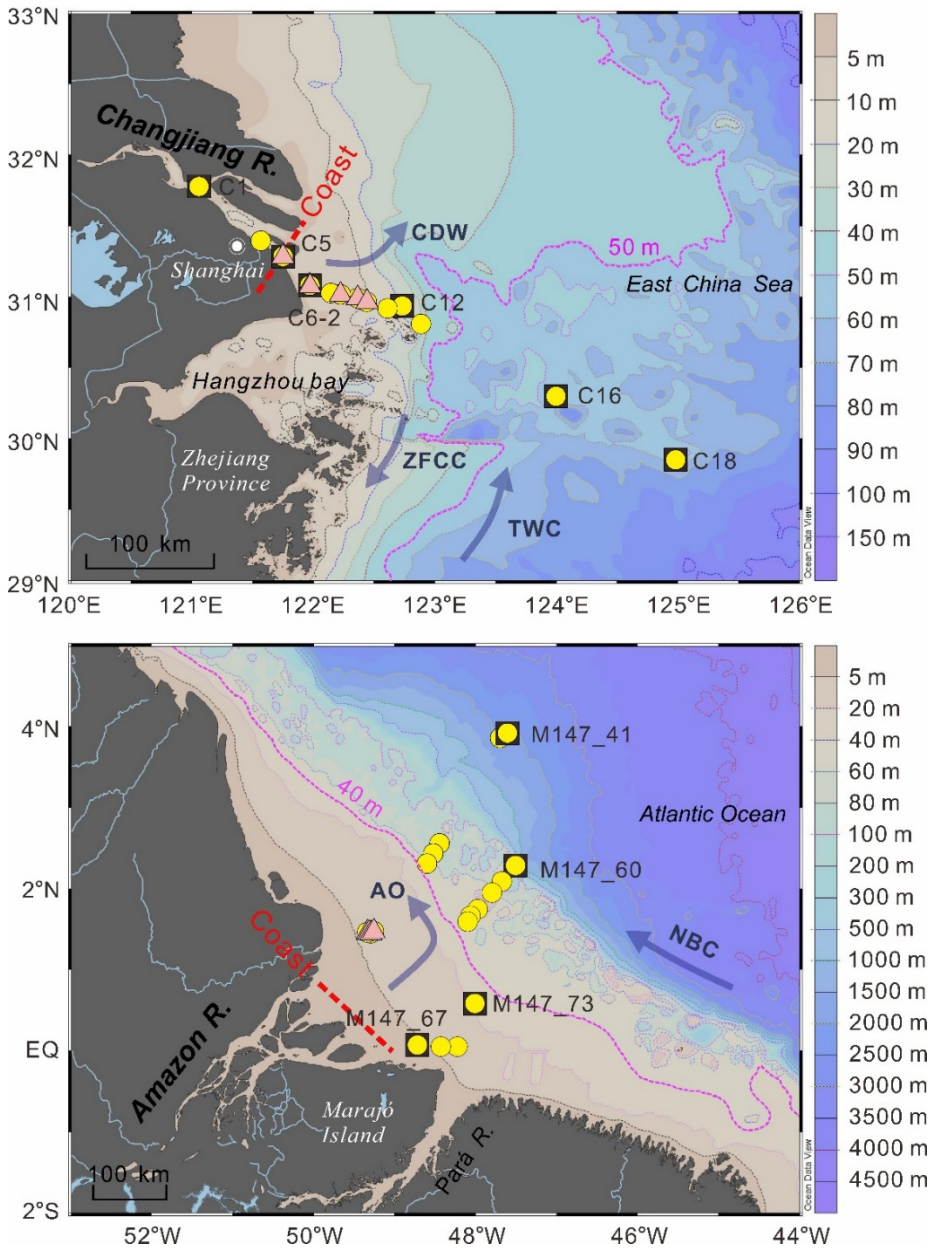

Figure 4.1 Bathymetric maps of the study area showing the locations of water samples (yellow circles), suspended particulate matter (pink triangles) and bottom sediments (black squares) offshore of the Changjiang (above) and Amazon estuaries (below). Major water masses in the study areas are indicated: CDW, Changjiang Diluted Water; TWC, Taiwan Warm Current; ZFCC, Zhe-Min Coastal Current; AO, Amazon Outflow; NBC, North Brazil Current. In this study, we take the 50 m and 40 m isobaths (marked in magenta dashed line) as the boundaries of inner and outer shelves offshore of the Changjiang and Amazon estuaries, respectively. All maps in this article were created using "Ocean Data View" (https://odv.awi.de, 2022.)

4.2.2 Materials

Sampling in the Changjiang Estuary was conducted between 27 August and 4 September 2019 during the cruise of the *Key Elements Cycling in the Changjiang-Estuary-Shelf Transect* (KECES 2019) organized by the State Key Laboratory of Marine Geology, Tongji University. A total of 15 stations (locating between 120°-126°E and 29°-32°N, Fig. 4.1) were sampled along the Changjiang-Estuary-Shelf Transect from the river mouth of Changjiang (sampling station C1, 121.06°E, 31.78°N) to the East China Sea continental shelf (station C18, 124.99°E, 29.86°N). Surface seawater samples were collected approximately 3-4 m upstream from the ship's bow via a pre-cleaned Masterflex I/P® Precision Pump tubing (C-Flex®) attached to the front end of a carbon fibre pole sampler, and water was pumped by a peristaltic pump. Near-bottom (~2 m above the seafloor) water samples were collected using a 5 L Teflon-coated Niskin-X bottle attached to a nylon rope. After collection, samples were immediately filtered onboard through an acid-cleaned 0.45 μm filter (Supor® PES, Pall). The filtrates were stored in pre-cleaned LDPE bottles (Nalgene), acidified to pH < 2 with trace metal grade HCl, and stored at 4°C until analysis. After filtering, the membranes (trapping SPM) were also stored refrigerated at 4°C. The bottom sediments (0-2 cm) were collected by a stainless-steel grab sampler from 6 stations from river channel to outer shelf (Fig. 4.1). Stations C1 and C5 are located in river channel where sediments are dominated by sand (Luo et al., 2012). Stations C6-2 and C12 are situated on the inner shelf down to about 50 m water depth where sediments are mainly composed of silty clay (Liu et al., 2006; Luo et al., 2012). Station C16 and C18 are located further offshore on the outer shelf where sediments are characterized by legacy sand (Shen, 1985). After collecting, samples were preserved in clean polyethylene zipper bags at 4°C. Upon arrival in the laboratory, the SPM and shelf bottom sediment samples were dried to constant weight at 40°C in a hot-air convection oven over several days.

Sampling in the Amazon Estuary was conducted between 29 April and 20 May 2018 during research cruise M147 RV Meteor (Koschinsky et al., 2018). Water samples were collected along a salinity transect from 0 to 35.5 PSU either with a towed-fish or a Conductivity-Temperature-Depth (CTD) rosette equipped with 24-Niskin bottles. After collection, 20 to 40 L of samples were transferred into acid-cleaned 20 L plastic cubic containers and filtered through 0.45 μm filters (Nucleopore) within a few hours and acidified to pH ~2 with concentrated ultrapure HCl. All water samples were stored at room temperature prior to analysis. Five low-salinity SPM samples were collected from the substantial amount of settled particulate matters in the 20 L CTD sample plastic cubic containers. Thus, the finest fraction retained on the 0.45 μm Nucleopore filters, accounting for 3.1 ± 1.0% (1 SD, n = 5) of the bulk SPM sample mass calculated based on the filter weights and SPM content of SPM samples, has not been captured. The SPM was rinsed into smaller acid-cleaned containers using MQ water and the supernatant was removed by siphoning after the SPM had visibly settled. Four bottom sediments (6-8 cm) were collected from inner shelf to continental slope using a multiple corer

(MUC). Stations 67 and 73 are located on the inner shelf where sediments are dominated by silty clay. Station 60 is located on the outer shelf where is considered as an outcrop of a relict transgressive sand layer (Nittrouer et al., 1983). Station 41 is situated further offshore on the continental slope, where sediments are again dominated by silty clay and contain a substantial amount of pelagic material. In the laboratory, the SPM and shelf bottom sediments were freeze dried at –52 °C and then homogenized for further treatment.

4.2.3 Methods

4.2.3.1 Pretreatment

Water samples of 0.6-1.5 L were pre-concentrated for ^{9}Be and ^{10}Be analysis following a simplified procedure based on the iron co-precipitation method (see details in Chapter 2). The Fe was separated from Be using Bio-Rad AG® 1-X8 (100-200 mesh) anion exchange resin following the established routine of Wittmann et al. (2015). About 1/6-1/10 of the collected solution after column was gravimetrically separated and evaporated, then re-dissolved in 1 mL 3% HNO_3, and spiked with 1 ng/g rhodium (Rh) as internal standard for ^{9}Be analysis. The remaining solutions were spiked with 0.15 mg ^{9}Be carrier and further purified by alkaline precipitation following the procedure described in Chapter 2 for ^{10}Be determination.

We applied a sequential leaching procedure to SPM and bottom sediments to determine ^{9}Be and ^{10}Be in the operationally defined "reactive" fraction (Wittmann et al., 2012), which includes the reactive amorphous oxy-hydroxide fraction (am-ox) and the crystalline oxides fraction (x-ox). Prior to chemical extraction, bottom sediments were dry-sieved into a fraction of <63 μm. In brief, approximately 0.5 to 1 g of SPM and sieved bottom sediments were first washed using pH 8-adjusted MQ water for three times to remove the remaining sea salt. The weakly adsorbed Be retained on the mineral surface was also removed by 1M ammonium acetate (pH = 7) following the procedure described in Chapter 3. The am-ox and x-ox fractions were then extracted using a 24-h treatment of 0.5 M HCl and a 4-h treatment at 80 °C of 1 M hydroxylamine hydrochloride, respectively (Wittmann et al., 2012). The leaching solutions were evaporated and re-dissolved in 3M HNO_3. One aliquot was taken for natural ^{9}Be and major element concentration measurements with an optical emission, inductively-coupled plasma spectrometer (ICP-OES, model Varian 720-ES with axial optics). The rest solution was spiked with 0.15 mg ^{9}Be carrier and left to equilibrate for several hours. After drying down, it was taken up for anion and cation column separation, and followed by an alkaline precipitation step to further purify ^{10}Be following the procedure described in Wittmann et al. (2015). The remaining silicate residue (min fraction) was decomposed using a mixture of concentrated HNO_3 and HF, as well as aqua regia (Wittmann et al., 2012) for ^{9}Be determination.

4.2.3.2 Analysis

The ^{9}Be concentrations for water samples were measured on a sector-field high-resolution inductively coupled plasma-mass spectrometer (HR-ICP-MS, Element2, Thermo Fisher Scientific) operated in low-resolution mode. The doubly charged ion rate was less than 3% and the oxide rate was less than 5%. ^{9}Be was quantified by an external calibration with standards prepared gravimetrically from our in-house ^{9}Be carrier solution. Procedure blanks were always below the detection limit (average instrument blank plus 3 times standard deviation (SD); as low as 4.0 pg Be, at most 15.0 pg Be), which accounts for 3-21% of ^{9}Be in our samples. The long-term external repeatability was 5% (1SD, n=14), monitored by processing an in-house artificial seawater standard (prepared by synthetic salt, Dupla Marin Premium Reef Salt Natural Balance, product code DM81432_MA) from January 2021 to January 2022. Recovery tests for iron co-precipitation procedure using a known amount of ^{9}Be-spiked artificial seawater resulted in a long-term recovery within ±10% (Chapter 2). Hence, we propagated a relative uncertainty of 10% to all seawater ^{9}Be measurements as a conservative estimate.

The ^{9}Be and other elemental analyses for SPM and bottom sediments were performed using ICP-OES. The long-term external uncertainty for OES measurement is 5% (1SD)(Wittmann et al., 2012). All the measurements were carried out in the Helmholtz Laboratory for the Geochemistry of the Earth Surface at GFZ Potsdam, Germany (von Blanckenburg et al., 2016).

The ^{10}Be concentrations for both water and sediments samples were obtained from accelerator mass spectrometry (AMS) measurements of $(^{10}Be/^{9}Be)_{carrier}$ ratios at University of Cologne, relative to the standards KN01-6-2 and KN01-5-3 with a ^{10}Be/^{9}Be ratio of 5.35×10^{-13} and 6.32×10^{-12}, respectively (Dewald et al., 2013). Long-term procedure blanks yielded an average ^{10}Be/^{9}Be ratio of $3.6 \pm 3.3\times10^{-15}$ (n=22).

4.2.3.3 Denudation rate calculation

Based on a steady-state mass balance framework for the ^{10}Be(meteoric)/^{9}Be system developed by von Blanckenburg et al. (2012), the denudation rate, comprising the sum of erosion and weathering, can be calculated as:

$$D_{met} = \frac{F_{met}^{^{10}Be}}{(\frac{^{10}Be}{^{9}Be})_{reac} \times [\ ^{9}Be]_{parent}} \times \left(\frac{[\ ^{9}Be]_{min}}{[\ ^{9}Be]_{reac}} + 1\right) \quad (4.1)$$

where D_{met} is the meteoric ^{10}Be/^{9}Be derived denudation rate, $F_{met}^{^{10}Be}$ (in atoms/cm^2/yr) is the depositional flux of ^{10}Be, $(^{10}Be/\ ^{9}Be)_{reac}$ is the ratio of ^{10}Be and ^{9}Be in chemically extracted reactive phase, including the amorphous oxy-hydroxide fraction (am-ox) and crystalline oxides

fraction (x-ox). $[\,^{9}Be]_{parent}$ (mg/kg) is the ^{9}Be present in the parent bedrock prior to weathering. The average $[\,^{9}Be]_{parent}$ is close to 2.5 μg/g for most felsic crustal rocks (von Blanckenburg et al., 2012).

Thus, it is likely that at large spatial scales such as the Changjiang and Amazon basin, the bedrock ^{9}Be concentration is close to this mean. $[\,^{9}Be]_{reac}$ (mg/kg) is the ^{9}Be concentration in extracted reactive phase, and $[\,^{9}Be]_{min}$ (mg/kg) is the ^{9}Be concentrations in the silicate residual phase. The detailed derivation of this equation can be found in von Blanckenburg et al. (2012). Note that this equation is a simplified equation that assumes the dissolved Be flux is negligible and the majority of Be flux is carried in the reactive particulate phase. In this case, the right hand of equation (4.1) can accurately reflect the fraction of ^{9}Be that was released from primary minerals into dissolved and reactive phases. This assumption can be fulfilled in our study areas, given the high pH value (>7) in the Changjiang and Amazon River (samples with salinity of 0 PSU in Table 4.1). Wittmann et al. (2015) have assessed the potential bias caused by neglecting the dissolved Be flux and found that it is negligible at pH values around 7 or higher.

A requirement for using the framework presented above is that the inputs of meteoric ^{10}Be ($J_{atm}^{^{10}Be}$, atoms/yr) into a drainage basin balance the outputs ($J_{riv}^{^{10}Be}$, atoms/yr) (von Blanckenburg et al., 2012). The $J_{atm}^{^{10}Be}$ is given by the depositional flux of meteoric ^{10}Be to the Earth's surface ($F_{met}^{^{10}Be}$, in atoms/cm^2/yr) that reaches the catchment's surface area A_{riv} (in m^2) (after Wittmann et al. (2015)):

$$J_{atm}^{^{10}Be} = F_{met}^{^{10}Be} \times A_{riv} \tag{4.2}$$

When neglecting the radioactive decay of ^{10}Be during sediment transfer and storage, the total meteoric flux of ^{10}Be exported by the river ($J_{riv}^{^{10}Be}$) can be given by (after Wittmann et al. (2015)):

$$J_{riv}^{^{10}Be} = J_{riv-reac}^{^{10}Be} + J_{riv-diss}^{^{10}Be} = A_{riv} \times E \times \left[^{10}Be\right]_{reac} + Q \times \left[^{10}Be\right]_{diss} \tag{4.3}$$

Where $J_{riv-reac}^{^{10}Be}$ and $J_{riv-diss}^{^{10}Be}$ are the ^{10}Be fluxes in the reactive (adsorbed and co-precipitated into secondary phases) and dissolved fractions (in atoms/yr) exported by rivers, respectively. The $J_{riv-reac}^{^{10}Be}$ can be calculated as the product of the catchments area A_{riv}, an independently-derived long-term erosion rate (E, in kg/m^2/yr), and ^{10}Be concentrations in the reactive fraction ($\left[^{10}Be\right]_{reac}$, in atoms/kg$_{solid}$). The $J_{riv-diss}^{^{10}Be}$ can be calculated from the dissolved ^{10}Be concentrations ($\left[^{10}Be\right]_{diss}$, in atoms/L$_{water}$), multiplied by river discharge (Q, in L/yr).

4.3 Results

4.3.1 Water samples

The dissolved ^{9}Be concentrations ($[^{9}Be]_{diss}$, square brackets denote concentrations) in the Changjiang and Amazon estuaries are comparable to previously published data (Fig. 4.2a and d, Brown et al., 1992b; Measures and Edmond, 1983). The $[^{9}Be]_{diss}$ of the river water endmember (salinity = 0 PSU) in the Amazon Estuary (1.22 nM) is nearly ten times higher than that in the Changjiang Estuary (0.14 ± 0.01 nM, n=6) (Table 4.1). The change of $[^{9}Be]_{diss}$ with salinity in the Changjiang Estuary has been discussed in detail in Chapter 3. In the Amazon estuary, $[^{9}Be]_{diss}$ in surface waters show an exponential decrease with salinity. For the three bottom water samples collected in the outer shelf area (salinity around 35 PSU), $[^{9}Be]_{diss}$ remain nearly constant with an average value of 0.02 nM, similar to the surface waters of the same salinity range.

The $[^{10}Be]_{diss}$ of the river water endmember in the Amazon Estuary (801 ± 66 atoms/g) is approximately five-fold higher than that of the Changjiang Estuary (168 ± 24 atom/g, n=3). In the Changjiang Estuary, dissolved ^{10}Be show similar behaviour as ^{9}Be: below salinity of 20 PSU, $[^{10}Be]_{diss}$ is similar in both surface and bottom waters, except for station C6-2 where $[^{10}Be]_{diss}$ in the bottom water is significantly higher than that in the surface water (Fig. 4.2b). Above 20 PSU, $[^{10}Be]_{diss}$ in surface waters show a significant decrease, whereas in bottom waters the decrease is less significant. The $[^{10}Be]_{diss}$ of our highest-salinity surface and bottom seawater samples are comparable to the previously published $[^{10}Be]_{diss}$ data in the East China Sea (Fig. 4.2b) (Yang et al., 2003). In the Amazon Estuary, the $[^{10}Be]_{diss}$ in surface waters initially exhibits a decrease to approximately 180 atoms/g, followed by an increase to about 710 atoms/g upon reaching a salinity of 35.5 PSU, falling within the range observed for $[^{10}Be]_{diss}$ in South Atlantic surface waters (Fig. 4.2e) (Measures et al., 1996). The three bottom waters show an average value of 686 ± 79 atoms/g, which is comparable to the surface waters at similar salinity range, but slightly lower than the bottom waters in the South Atlantic (Fig. 4.2e) (Measures et al., 1996).

The $(^{10}Be/^{9}Be)_{diss}$ of the river water endmember in the Changjiang Estuary ($2.04 \pm 0.17 \times 10^{-9}$, n=3) is slightly higher than that in the Amazon Estuary ($1.09 \pm 0.09 \times 10^{-9}$). Along the salinity gradient, $(^{10}Be/^{9}Be)_{diss}$ shows nearly exponential increase (Fig. 4.2c and f) in both estuaries. The increase is about a factor of 3 in the Changjiang estuary, but a factor of 70 in the Amazon estuary. The river water and seawater endmembers in the Amazon Estuary are slightly higher than the reported $(^{10}Be/^{9}Be)_{diss}$ data at Óbidos station ($0.75 \pm 0.11 \times 10^{-9}$) in the lowland Amazon River (Wittmann et al., 2015) and the South Atlantic (Measures et al., 1996) (Fig. 4.2f), respectively. Notably, while the $(^{10}Be/^{9}Be)_{diss}$ are nearly identical in surface and bottom waters below 20 PSU in the Changjiang Estuary, at high salinities (> 20 PSU), the hypoxic bottom

water show lower $(^{10}Be/^{9}Be)_{diss}$ signature compared to the surface water of similar salinity (Fig. 4.2c).

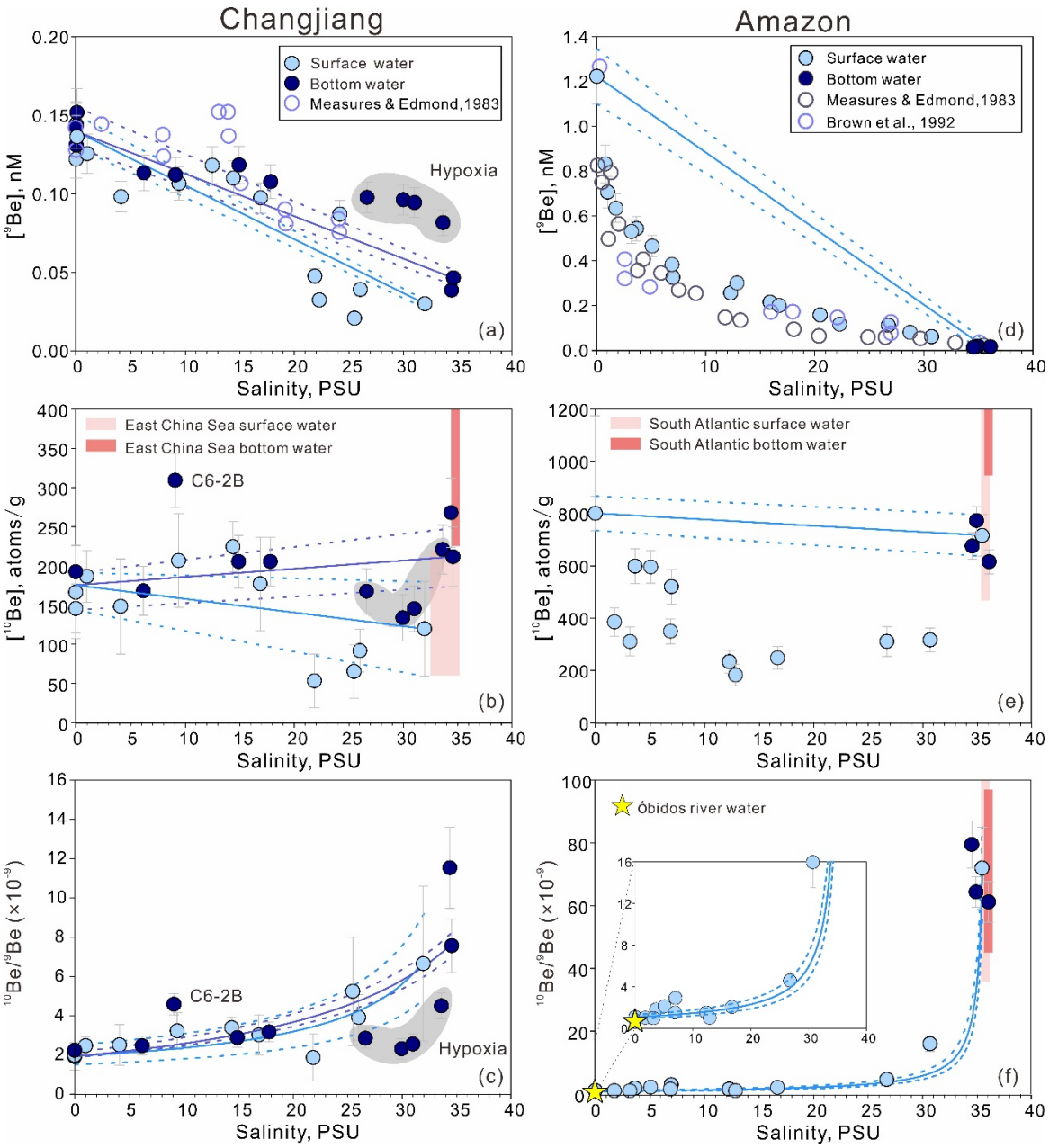

Figure 4.2 [^{9}Be], [^{10}Be] and ^{10}Be/^{9}Be in surface and bottom waters in the Changjiang (left column) and Amazon (right column) estuaries. Data for the East China Sea and the South Atlantic is derived from Yang et al. (2003) and Measures et al. (1996), respectively. The ^{10}Be/^{9}Be data in Óbidos river water is from Wittmann et al. (2015). The solid lines represent the predicted conservative mixing lines between the river water and seawater endmembers for concentrations and isotopic compositions. Two conservative mixing lines are given for the Changjiang estuary: the light blue line represents the conservative mixing of river water with surface seawater endmember (C18S), and the dark blue line represents the conservative mixing with bottom seawater endmember (C16B). The dashed lines above and below the corresponding solid lines reflect the uncertainties of the estimations of the [^{9}Be], [^{10}Be] and ^{10}Be/^{9}Be endmember values.

Table 4.1 Sampling location, hydrological parameters and ^{9}Be, ^{10}Be, and $^{10}Be/^{9}Be$ for water samples

Sample ID	Longitude (°E)	Latitude (°N)	Water depth (m)	Salinity (PSU)	pH	$[^{9}Be]_{diss}$[a] (nM)	$[^{10}Be]_{diss}$[b] (atoms/g)	$(^{10}Be/^{9}Be)_{diss}$[c] ($\times10^{-9}$)
				Changjiang Estuary				
w-C1S	121.06	31.78	1	0.0	7.80	0.144	166 ± 59	1.9 ± 0.7
w-C1B	121.06	31.78	11	0.0	7.83	0.152	--	--
w-C3S	121.57	31.40	1	0.0	7.90	0.122	145 ± 31	2.0 ± 0.4
w-C3B	121.57	31.40	12	0.0	7.87	0.131	--	--
w-C5S	121.75	31.29	1	0.0	7.84	0.136	--	--
w-C5B	121.75	31.29	16	0.0	7.78	0.143	192 ± 34	2.2 ± 0.4
w-C6-1S	121.97	31.09	1	1.0	7.84	0.126	187 ± 33	2.5 ± 0.5
w-C6-2S	121.98	31.09	1	4.1	7.83	0.098	148 ± 61	2.5 ± 1.0
w-C6-2B	121.98	31.09	7	6.2	7.79	0.113	168 ± 31	2.5 ± 0.5
w-C6-3S	121.99	31.08	1	9.4	7.83	0.107	207 ± 60	3.2 ± 0.9
w-C6-3B	121.99	31.08	7	9.1	7.84	0.112	309 ± 34	4.6 ± 0.5
w-C7S	122.15	31.03	1	12.5	7.81	0.118	--	--
w-C8S	122.24	31.02	1	14.4	7.84	0.110	224 ± 32	3.4 ± 0.5
w-C8B	122.24	31.02	6	14.9	7.83	0.118	205 ± 34	2.9 ± 0.5
w-C9S	122.36	31.00	1	16.9	7.84	0.097	177 ± 60	3.0 ± 1.0
w-C9B	122.36	31.00	10	17.8	7.80	0.108	206 ± 31	3.2 ± 0.5
w-C10S	122.45	30.97	1	21.9	8.08	0.048	53 ± 34	1.9 ± 1.2
w-C10B	122.45	30.97	12	26.7	7.82	0.098	167 ± 29	2.8 ± 0.5
w-C11S	122.62	30.92	1	24.2	8.06	0.087	--	--

Continued

Sample ID	Longitude (°E)	Latitude (°N)	Water depth (m)	Salinity (PSU)	pH	$[^{9}Be]_{diss}$ [a] (nM)	$[^{10}Be]_{diss}$ [b] (atoms/g)	$(^{10}Be/^{9}Be)_{diss}$ [c] ($\times 10^{-9}$)
				Changjiang Estuary				
w-C11B	122.62	30.92	20	30.0	7.78	0.096	134 ± 30	2.3 ± 0.5
w-C12S	122.74	30.94	1	22.3	8.11	0.032	--	--
w-C12B	122.74	30.94	21	31.0	7.78	0.094	145 ± 29	2.6 ± 0.5
w-C13S	122.89	30.81	1	26.0	8.16	0.039	92 ± 27	3.9 ± 1.2
w-C13B	122.89	30.81	30	33.6	7.76	0.082	221 ± 31	4.5 ± 0.7
w-C16S	124.00	30.30	1	25.5	8.24	0.021	65 ± 34	5.2 ± 2.8
w-C16B	124.00	30.30	46	34.6	7.87	0.046	212 ± 38	7.6 ± 1.4
w-C18S	124.99	29.87	1	32.0	8.17	0.030	120 ± 60	6.6 ± 3.9
w-C18B	124.99	29.87	62	34.4	7.93	0.039	268 ± 44	11.5 ± 2.1
				Amazon Estuary				
w-M147_26S	-49.33	1.45	1	0.8	7.88	0.833	--	--
w-M147_27S	-49.32	1.45	3	1.8	8.32	0.635	385 ± 54	1.0 ± 0.1
w-M147_28S	-49.28	1.44	1	3.2	8.18	0.531	311 ± 55	1.0 ± 0.2
w-M147_29S	-49.29	1.44	1	5.1	7.89	0.466	596 ± 62	2.1 ± 0.2
w-M147_30S	-49.30	1.44	1	6.9	7.98	0.383	350 ± 48	1.5 ± 0.2
w-M147_31S	-49.25	1.46	1	12.9	--	0.301	182 ± 41	1.0 ± 0.2
w-M147_32S	-48.59	2.30	1	16.7	8.37	0.201	248 ± 43	2.0 ± 0.4
w-M147_33S	-48.50	2.43	1	22.3	8.22	0.117	--	--
w-M147_34S	-48.44	2.55	1	28.8	8.12	0.081	--	--
w-M147_fish25S	-47.60	3.91	1	35.5	--	0.023	--	--

Continued

Sample ID	Longitude (°E)	Latitude (°N)	Water depth (m)	Salinity (PSU)	pH	$[^{9}Be]_{diss}$ [a] (nM)	$[^{10}Be]_{diss}$ [b] (atoms/g)	$(^{10}Be/^{9}Be)_{diss}$ [c] ($\times10^{-9}$)
				Amazon Estuary				
w-M147_64S	-47.79	1.94	1	26.8	8.06	0.112	311 ± 57	4.6 ± 0.9
w-M147_66S	-48.71	0.05	1	0.0	7.23	1.223	801 ± 66	1.1 ± 0.1
w-M147_70S	-48.42	0.02	1	1.0	--	0.707	--	--
w-M147_71S	-48.22	0.03	1	3.7	8.20	0.544	599 ± 67	1.8 ± 0.2
w-M147_72S	-48.00	0.57	1	7.0	8.53	0.327	521 ± 66	2.9 ± 0.4
w-M147_74S	-47.97	1.74	1	20.5	8.29	0.158	--	--
w-M147_75S	-48.04	1.65	1	15.9	6.69	0.215	--	--
w-M147_78S	-48.08	1.58	1	12.3	8.47	0.256	233 ± 44	1.5 ± 0.3
w-M147_fish55S	-47.50	2.27	1	35.5	--	0.017	716 ± 80	71.9 ± 13.0
w-M147_fish56S	-47.68	2.08	1	30.7	--	0.062	316 ± 46	16.0 ± 2.5
w-M147_40B	-47.602	3.953	1968	35.0	--	0.020	771 ± 69	64.1 ± 6.1
w-M147_58B	-47.456	2.320	944	34.6	--	0.014	674 ± 66	79.2 ± 9.0
w-M147_61B	-47.661	2.085	83	36.1	--	0.017	614 ± 63	60.9 ± 7.7

[a] The uncertainty for ^{9}Be concentration is 10% (see section 4.2.3.2).

[b] The ^{10}Be value is blank-corrected, using a long-term $^{10}Be/^{9}Be$ blank ratio of $3.6 \pm 3.3\times10^{-15}$ (n=22). uncertainty for ^{10}Be is derived from 1σ analytical uncertainty from AMS measurement and 1σ uncertainty of blank ratio.

[c] Uncertainty (1SD) is propagated from ^{9}Be and ^{10}Be.

4.3.2 SPM samples

The [^{9}Be] and [^{10}Be] in the am-ox and x-ox fractions of SPM remain nearly constant with salinity in both the Changjiang and Amazon estuaries (Fig. 4.3, Table 4.2). Only a small hump is observed for [^{9}Be] and [^{10}Be] in the am-ox fraction of the Changjiang Estuary SPM at salinities around 1 to 6 PSU. Concentrations in the am-ox fraction are always higher than in the x-ox fraction. While [^{9}Be] are comparable between two estuaries for both the am-ox (around 0.6 μg/g) and x-ox fractions (around 0.1 μg/g), [^{10}Be] is higher in the Changjiang Estuary SPM, especially in the am-ox fraction, which are ~3-fold higher than that in the Amazon SPM. As a consequence, the (^{10}Be/^{9}Be) is higher in the Changjiang Estuary SPM than in the Amazon Estuary. For the Changjiang Estuary SPM, $(^{10}Be/^{9}Be)_{am\text{-}ox}$ increases from ~3.24×10^{-9} to ~4×10^{-9} from fresh to saline water-SPM, whereas $(^{10}Be/^{9}Be)_{x\text{-}ox}$ increases from ~2.38×10^{-9} to ~3.22×10^{-9}, respectively. The $(^{10}Be/^{9}Be)_{am\text{-}ox}$ and $(^{10}Be/^{9}Be)_{x\text{-}ox}$ in the Amazon estuary SPM show insignificant changes along salinity, with an average of 1.26×10^{-9} and 9.48×10^{-10}, respectively.

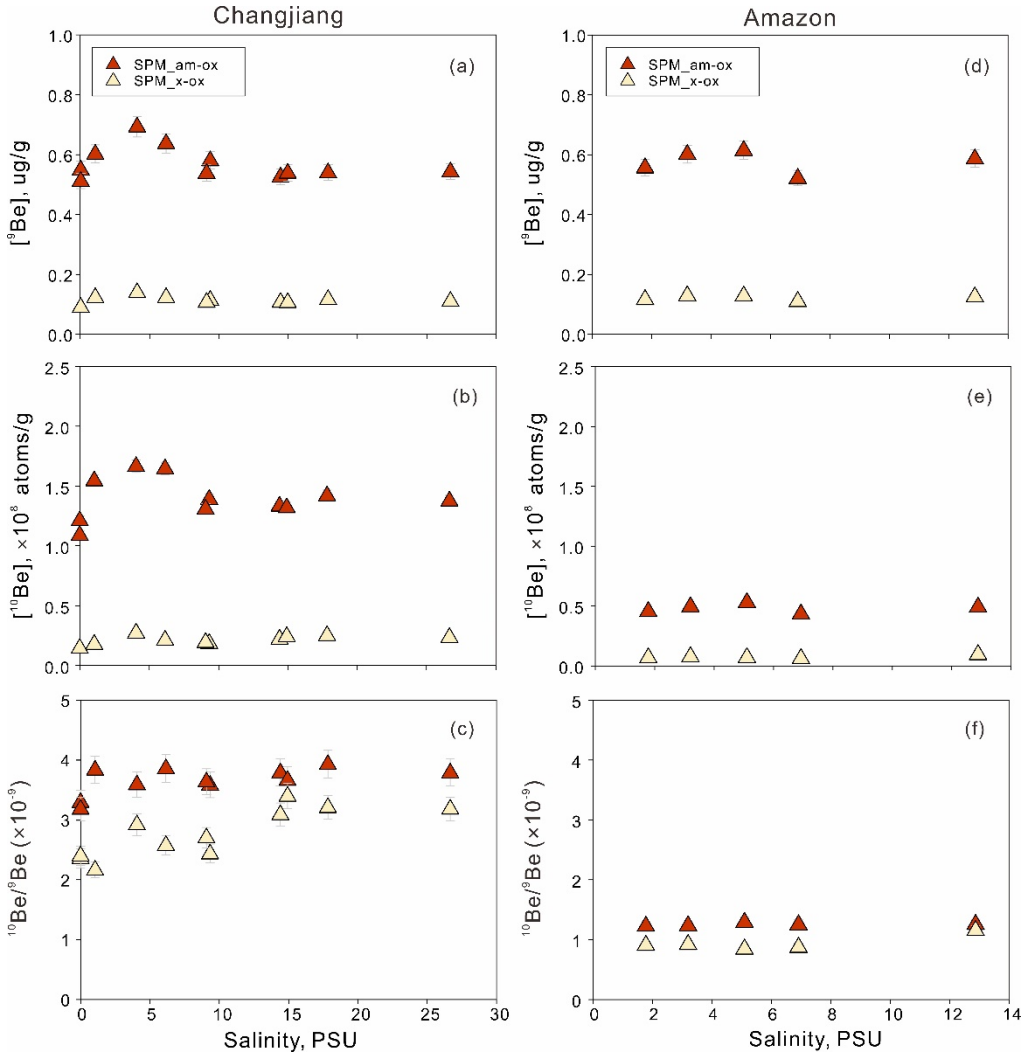

Figure 4.3 [^{9}Be], [^{10}Be] and ^{10}Be/^{9}Be ratio in the amorphous fraction (am-ox) and crystalline fraction (x-ox) of suspended sediments in the Changjiang (left column) and Amazon (right column) estuaries.

Table 4.2 The ^{9}Be, ^{10}Be, and $^{10}Be/^{9}Be$ data for suspended particulate matter (SPM) [a]

Sample ID	$[^{10}Be]_{am\text{-}ox}$ ($\times10^{8}$ at/g)	$[^{10}Be]_{x\text{-}ox}$ ($\times10^{8}$ at/g)	$[^{10}Be]_{reac}$ ($\times10^{8}$ at/g)	$[^{9}Be]_{am\text{-}ox}$ (μg/g)	$[^{9}Be]_{x\text{-}ox}$ (μg/g)	$[^{9}Be]_{reac}$ (μg/g)	$[^{9}Be]_{min}$ (μg/g)	$(^{10}Be/^{9}Be)_{am\text{-}ox}$ ($\times10^{-9}$)	$(^{10}Be/^{9}Be)_{x\text{-}ox}$ ($\times10^{-9}$)	$(^{10}Be/^{9}Be)_{reac}$ ($\times10^{-9}$)
Changjiang Estuary										
s-C5S	1.21 ± 0.04	0.14 ± 0.01	1.36 ± 0.04	0.55	0.09	0.64 ± 0.03	1.38	3.30 ± 0.19	2.36 ± 0.16	3.16 ± 0.48
s-C5B	1.09 ± 0.04	0.15 ± 0.01	1.24 ± 0.04	0.51	0.09	0.60 ± 0.03	1.41	3.18 ± 0.19	2.41 ± 0.16	3.06 ± 0.49
s-C6-1S	1.55 ± 0.05	0.18 ± 0.01	1.73 ± 0.05	0.60	0.12	0.73 ± 0.03	1.68	3.84 ± 0.23	2.17 ± 0.13	3.55 ± 0.18
s-C6-2S	1.67 ± 0.05	0.27 ± 0.01	1.94 ± 0.05	0.69	0.14	0.84 ± 0.04	1.63	3.59 ± 0.21	2.92 ± 0.18	3.48 ± 0.61
s-C6-2B	1.65 ± 0.05	0.21 ± 0.01	1.86 ± 0.05	0.65	0.13	0.77 ± 0.03	1.49	3.86 ± 0.23	2.58 ± 0.16	3.65 ± 0.62
s-C6-3S	1.39 ± 0.04	0.19 ± 0.01	1.58 ± 0.05	0.58	0.11	0.70 ± 0.03	1.50	3.58 ± 0.21	2.44 ± 0.16	3.39 ± 0.59
s-C6-3B	1.31 ± 0.04	0.20 ± 0.01	1.51 ± 0.04	0.54	0.11	0.65 ± 0.03	1.47	3.64 ± 0.22	2.71 ± 0.17	3.48 ± 0.61
s-C8S	1.34 ± 0.04	0.22 ± 0.01	1.56 ± 0.04	0.53	0.11	0.64 ± 0.03	1.34	3.79 ± 0.23	3.10 ± 0.19	3.67 ± 0.19
s-C8B	1.32 ± 0.04	0.25 ± 0.01	1.57 ± 0.04	0.54	0.11	0.65 ± 0.03	1.22	3.66 ± 0.22	3.40 ± 0.21	3.62 ± 0.18
s-C9B	1.42 ± 0.05	0.25 ± 0.01	1.67 ± 0.05	0.54	0.12	0.66 ± 0.03	1.45	3.93 ± 0.23	3.21 ± 0.20	3.80 ± 0.19
s-C10B	1.38 ± 0.04	0.24 ± 0.01	1.62 ± 0.05	0.54	0.11	0.66 ± 0.03	1.40	3.79 ± 0.23	3.19 ± 0.20	3.69 ± 0.19
Amazon Estuary										
s-M147_27S	0.46 ± 0.02	0.071 ± 0.003	0.53 ± 0.02	0.56	0.12	0.67 ± 0.03	1.64	1.23 ± 0.07	0.92 ± 0.06	1.18 ± 0.06
s-M147_28S	0.50 ± 0.02	0.080 ± 0.003	0.58 ± 0.02	0.60	0.13	0.73 ± 0.03	1.59	1.24 ± 0.07	0.93 ± 0.06	1.18 ± 0.06
s-M147_29S	0.53 ± 0.02	0.073 ± 0.003	0.61 ± 0.02	0.62	0.13	0.74 ± 0.03	1.64	1.30 ± 0.08	0.85 ± 0.06	1.22 ± 0.06
s-M147_30S	0.44 ± 0.01	0.065 ± 0.003	0.50 ± 0.02	0.52	0.11	0.63 ± 0.03	1.37	1.26 ± 0.08	0.88 ± 0.06	1.19 ± 0.06
s-M147_31S	0.49 ± 0.02	0.098 ± 0.004	0.59 ± 0.02	0.59	0.13	0.71 ± 0.03	1.55	1.26 ± 0.08	1.16 ± 0.07	1.24 ± 0.06

[a] A 5% uncertainty is applied for $[^{9}Be]_{am\text{-}ox}$, $[^{9}Be]_{x\text{-}ox}$ and $[^{9}Be]_{min}$ that represents the long-term repeatability for ICP-OES measurements. Uncertainties for $[^{10}Be]_{am\text{-}ox}$, $[^{10}Be]_{x\text{-}ox}$, $(^{10}Be/^{9}Be)_{am\text{-}ox}$ and $(^{10}Be/^{9}Be)_{x\text{-}ox}$ are calculated as for water samples (Table 4.1). For $[^{9}Be]_{reac}$, $[^{10}Be]_{reac}$, and $(^{10}Be/^{9}Be)_{reac}$, uncertainties are propagated from am-ox and x-ox.

4.3.3 Bottom sediment

In contrast to SPM, the [^{9}Be], [^{10}Be] and ^{10}Be/^{9}Be in bottom sediments exhibit significant variability offshore from the coast (Fig. 4.4, Table 4.3). In the Changjiang Estuary, [^{9}Be] in both am-ox and x-ox fractions increase up to nearly two-fold from river channel sediments (salinity = 0) to shelf sediments (salinity > 0). While $[^{10}Be]_{x\text{-}ox}$ only display a slight increase, $[^{10}Be]_{am\text{-}ox}$ show a significant increase from 3.69×10^{7} to 1.78×10^{8} atoms/g further offshore. Consequently, the $(^{10}Be/^{9}Be)_{am\text{-}ox}$ in outer-shelf sediments (~8.45×10^{-9}) is higher by a factor of three than that in river channel sediments (~3.13×10^{-9}), and the $(^{10}Be/^{9}Be)_{x\text{-}ox}$ doubles from ~2.26×10^{-9} to 4.03×10^{-9}. In the Amazon Estuary, $[^{9}Be]_{am\text{-}ox}$ in outer-shelf and continental slope sediments are significantly lower than that in inner-shelf sediments, while no apparent change can be observed for $[^{9}Be]_{x\text{-}ox}$. In contrast, $[^{10}Be]_{am\text{-}ox}$ increases 5-10 fold from inner-shelf sediments (~5.08×10^{7} atoms/g) to outer-shelf /slope sediments (2.53-4.87 $\times 10^{8}$ atoms/g), whereas $[^{10}Be]_{x\text{-}ox}$ only show a slight increase. Correspondingly, the $(^{10}Be/^{9}Be)_{am\text{-}ox}$ increases from ~1.50×10^{-9} to 2.01-3.57$\times10^{-8}$ away from the coast, and the $(^{10}Be/^{9}Be)_{x\text{-}ox}$ increases from ~1.20×10^{-9} to 0.63-1.36$\times10^{-8}$.

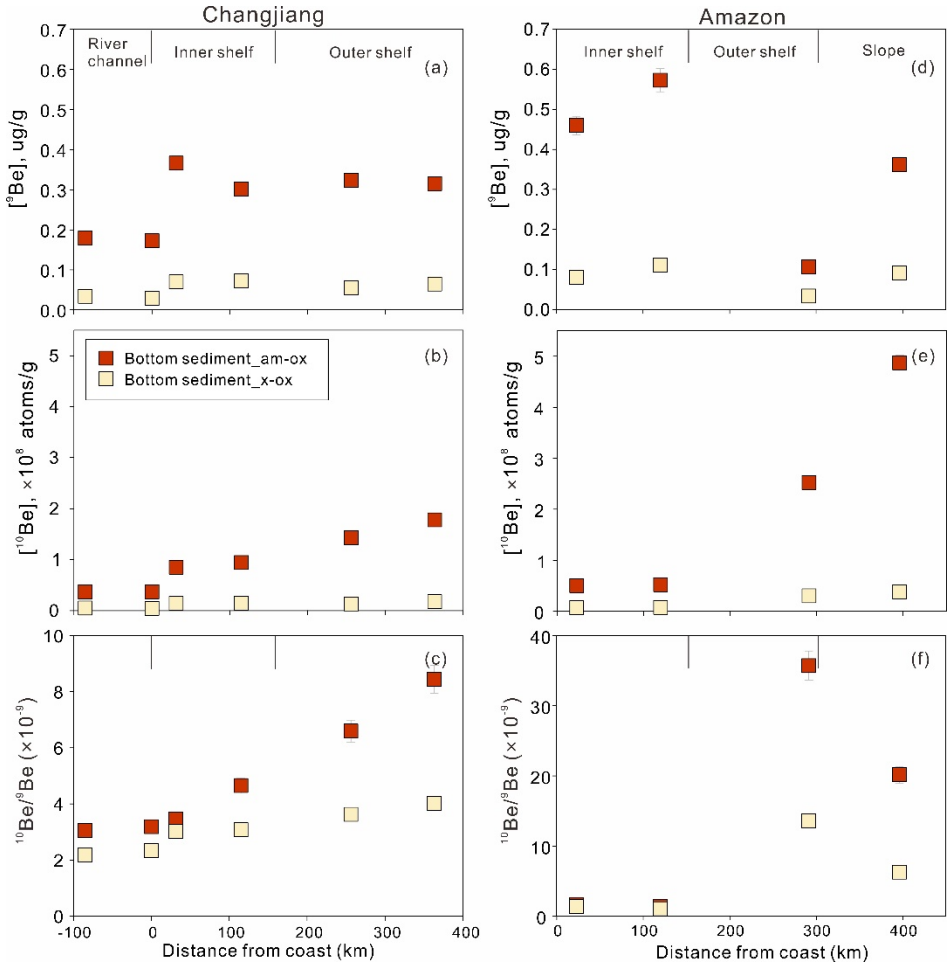

Figure 4.4 [^{9}Be], [^{10}Be] and ^{10}Be/^{9}Be in the amorphous fraction (am-ox) and crystalline fraction (x-ox) of bottom sediments away from the Changjiang (left column) and Amazon (right column) coasts.

Table 4.3 The ^{9}Be, ^{10}Be, and $^{10}Be/^{9}Be$ data for bottom sediments[a]

Sample ID	$[^{10}Be]_{am\text{-}ox}$ ($\times10^{8}$ at/g)	$[^{10}Be]_{x\text{-}ox}$ ($\times10^{8}$ at/g)	$[^{10}Be]_{reac}$ ($\times10^{8}$ at/g)	$[^{9}Be]_{am\text{-}ox}$ (μg/g)	$[^{9}Be]_{x\text{-}ox}$ (μg/g)	$[^{9}Be]_{reac}$ (μg/g)	$[^{9}Be]_{min}$ (μg/g)	$(^{10}Be/^{9}Be)_{am\text{-}ox}$ ($\times10^{-9}$)	$(^{10}Be/^{9}Be)_{x\text{-}ox}$ ($\times10^{-9}$)	$(^{10}Be/^{9}Be)_{reac}$ ($\times10^{-9}$)
Changjiang Estuary										
C1	0.37 ± 0.01	0.050 ± 0.003	0.42 ± 0.01	0.18	0.03	0.21 ± 0.01	1.19	3.08 ± 0.19	2.20 ± 0.17	2.93 ± 0.16
C5	0.37 ± 0.01	0.046 ± 0.003	0.42 ± 0.01	0.17	0.03	0.20 ± 0.01	1.40	3.21 ± 0.20	2.35 ± 0.18	3.08 ± 0.17
C6-2	0.85 ± 0.03	0.142 ± 0.006	0.99 ± 0.03	0.37	0.07	0.44 ± 0.02	1.25	3.48 ± 0.21	3.04 ± 0.20	3.41 ± 0.18
C12	0.94 ± 0.03	0.149 ± 0.005	1.09 ± 0.03	0.30	0.07	0.37 ± 0.02	1.37	4.67 ± 0.28	3.09 ± 0.19	4.37 ± 0.22
C16	1.43 ± 0.04	0.133 ± 0.005	1.56 ± 0.05	0.32	0.05	0.38 ± 0.02	1.18	6.62 ± 0.39	3.65 ± 0.23	6.19 ± 0.32
C18	1.78 ± 0.06	0.174 ± 0.007	1.95 ± 0.06	0.32	0.06	0.38 ± 0.02	1.21	8.45 ± 0.50	4.04 ± 0.25	7.70 ± 0.22
Amazon Estuary										
M147_41	4.87 ± 0.15	0.381 ± 0.013	5.25 ± 0.15	0.36	0.09	0.45 ± 0.02	1.06	20.15 ± 1.18	6.25 ± 0.37	17.35 ± 0.87
M147_60	2.53 ± 0.08	0.304 ± 0.010	2.83 ± 0.08	0.11	0.03	0.14 ± 0.01	0.39	35.70 ± 2.1	13.58 ± 0.81	30.38 ± 1.47
M147_67	0.50 ± 0.02	0.072 ± 0.003	0.58 ± 0.02	0.46	0.08	0.54 ± 0.02	1.27	1.64 ± 0.10	1.35 ± 0.09	1.60 ± 0.08
M147_73	0.52 ± 0.02	0.076 ± 0.003	0.60 ± 0.02	0.57	0.11	0.68 ± 0.03	1.45	1.37 ± 0.08	1.03 ± 0.07	1.31 ± 0.07

[a] Refer to Table 4.2 for uncertainties.

4.3.4 Comparison of $^{10}Be/^{9}Be$ ratio in seawater, suspended sediments and bottom sediments

We can now compare the $^{10}Be/^{9}Be$ ratios of different phases (i.e., am-ox and x-ox fractions) of SPM and bottom sediments with the dissolved $^{10}Be/^{9}Be$ ratios. Good agreements (within a factor of 2) are observed between $^{10}Be/^{9}Be$ ratios from suspended and bottom sediments either in the am-ox or x-ox fraction versus dissolved $^{10}Be/^{9}Be$ ratios within a certain salinity range or distance off the coast in both estuaries (Fig. 4.5). In the Changjiang Estuary, this agreement persists up to a salinity of about 30 PSU (~150 km away from the coast). For fresh water samples, the $^{10}Be/^{9}Be$ ratios in the x-ox fraction of both SPM and bottom sediments agree even better with dissolved $^{10}Be/^{9}Be$ ratios (Fig. 4.5). In the Amazon Estuary, due to the relatively low-resolution sampling, we can only assure that the agreement exists over a salinity range of at least 15 PSU (~150 km off the coast). At high salinities (>30 PSU), approximately >150 km away from the Changjiang coast and >150 km from the Amazon coast, we observe significant differences between $^{10}Be/^{9}Be$ ratios in the am-ox or x-ox fractions of bottom sediments and in bottom waters, respectively. Except for station C12 located at the centre of the Changjiang hypoxic zone where the $^{10}Be/^{9}Be$ ratios in bottom sediment (either in am-ox or x-ox fractions) are higher than that in bottom seawater, all other outer shelf/slope sediments show lower $^{10}Be/^{9}Be$ ratios when compared to bottom seawaters. The $(^{10}Be/^{9}Be)_{am\text{-}ox}$ of outer shelf/slope bottom sediments are much closer to the $(^{10}Be/^{9}Be)_{diss}$ in bottom waters than the $(^{10}Be/^{9}Be)_{x\text{-}ox}$.

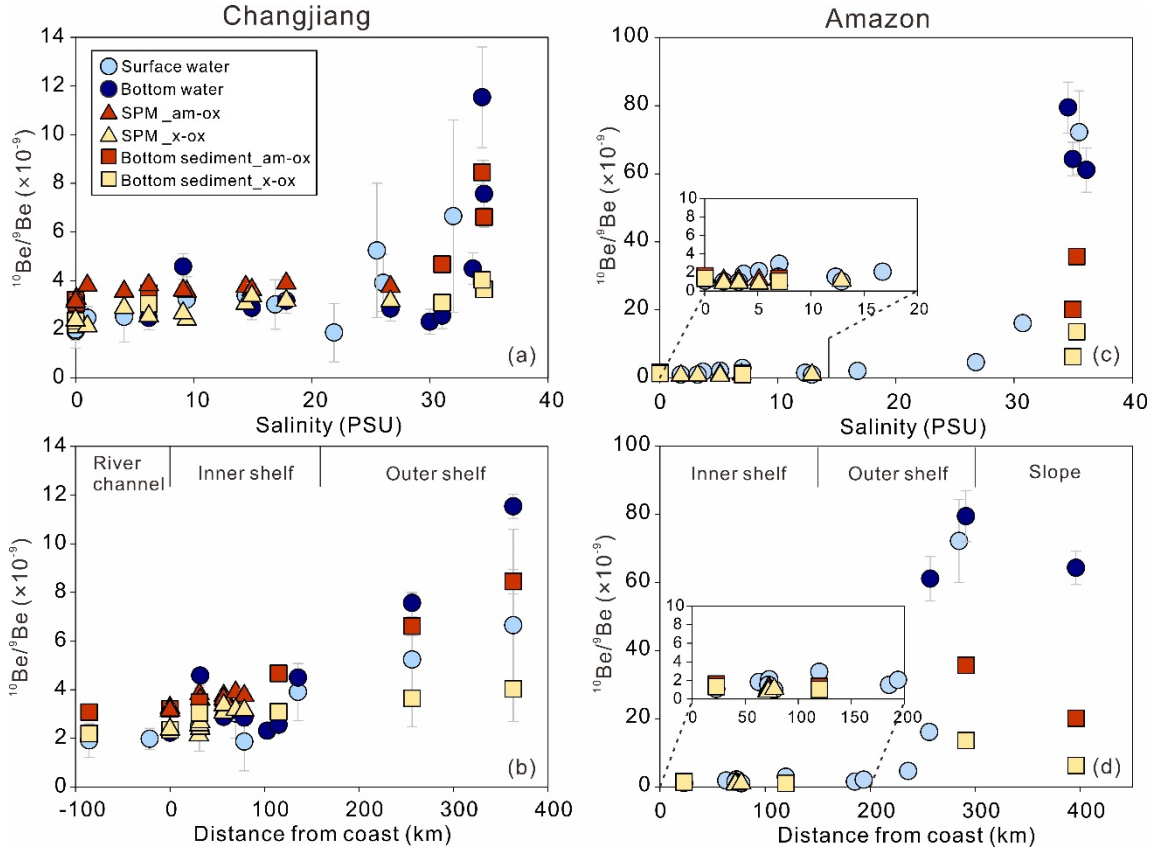

Figure 4.5 Comparison of $^{10}Be/^{9}Be$ in the amorphous fraction (am-ox) and crystalline fraction (x-ox) of suspended and bottom sediments in the Changjiang (left column) and

Amazon (right column) estuaries with the dissolved $^{10}Be/^{9}Be$ along the salinity gradient and distance from the coast.

4.4 Discussion

4.4.1 Boundary exchange processes and their influence on coastal dissolved and sedimentary $^{10}Be/^{9}Be$ ratio

The dissolved ^{9}Be and ^{10}Be display non-conservative behaviour in both estuaries (Fig. 4.2). The removal of dissolved ^{9}Be at low salinity (S<5 PSU) and in the surface waters at high salinity (S>20 PSU) in the Changjiang Estuary are attributed to colloidal flocculation and biological scavenging, respectively, while the release at mid-salinity and high-salinity bottom waters is considered to result from diagenetic release and/or submarine groundwater discharge (see Chapter 3). Due to the large analytical uncertainties, it is difficult to characterize the removal/release behaviour of ^{10}Be at low-mid salinity. However, given the similar geochemical behaviour of ^{9}Be and ^{10}Be, it is expected that the distribution of ^{10}Be is controlled by the same mechanisms. In the Amazon Estuary, the significant removal of dissolved ^{9}Be and ^{10}Be was attributed to colloidal flocculation, similar as other particle-reactive elements (Gledhill et al., 2022; Xu et al., 2023). Despite the non-conservative behaviour of dissolved ^{9}Be and ^{10}Be, the $(^{10}Be/^{9}Be)_{diss}$ generally follow the theoretical conservative mixing lines (Fig. 4.2c and f) in both estuaries, except for the bottom waters in the hypoxic zone of the Changjiang Estuary (Fig. 4.2c) which show remarkably lower $(^{10}Be/^{9}Be)_{diss}$ compared to the conservative mixing lines. This suggests that colloidal flocculation and adsorption-desorption processes during estuarine mixing will only affect the concentrations of dissolved ^{9}Be and ^{10}Be, but not alter the $(^{10}Be/^{9}Be)_{diss}$. Instead, the lower $(^{10}Be/^{9}Be)_{diss}$ in the hypoxic bottom waters in the Changjiang Estuary may indicate a benthic Be source characterized by a lower $^{10}Be/^{9}Be$ ratio than that of the bottom waters. Although the diagenetic release of Be from sediments during Fe-Mn cycling into overlying seawater has been observed on the East China Sea shelf, we argue that it may not be the primary contributor to the lower $^{10}Be/^{9}Be$ in the hypoxic bottom waters, because the mean $(^{10}Be/^{9}Be)_{reac}$ value for the Changjiang SPM (n=8, 1SD) of $3.51\pm0.23 \times10^{-9}$ is slightly higher than the mean $(^{10}Be/^{9}Be)_{diss}$ value of $3.05\pm0.10 \times10^{-9}$ for the hypoxic bottom seawaters (n=4, 1SD). Although no $^{10}Be/^{9}Be$ data for submarine groundwater is available within the Changjiang Estuary, previously reported $(^{10}Be/^{9}Be)$ for groundwater in other regions appear to be an order of magnitude lower than for stream water, at approximately 10^{-10} level (Dannhaus et al., 2018). Therefore, the submarine groundwater discharge is more likely to be the responsible cause for the altered $^{10}Be/^{9}Be$ signal in the hypoxic bottom waters. In the Amazon outer shelf where no significant groundwater discharge has been observed, the $(^{10}Be/^{9}Be)_{diss}$ in bottom waters show no significant change compared to surface waters (Fig. 4.2f). This may suggest that the diagenetic release of Be solely is less likely to modify the $^{10}Be/^{9}Be$ signal in ocean bottom waters.

In addition to the changes in dissolved $^{10}Be/^{9}Be$ ratios, we note that the reactive $^{10}Be/^{9}Be$ ratios in both Changjiang and Amazon outer shelf/slope sediments significantly increases as $(^{10}Be/^{9}Be)_{diss}$ increases in bottom waters (Fig. 4.5). Although all outer-shelf sediments in this study are characterized by carbonate and relict sands formed from the last sea-level lowstand (Nittrouer et al., 1983; Shen, 1985), the source of the relict sands are still dominated by paleo-Changjiang (Huang et al., 2020; Zhongbo et al., 2012) and paleo-Amazon sediments (Milliman et al., 1975). Since carbonate is not a strong scavenger for Be (Bourlès et al., 1989a; Luo and Ku, 2004; Sarathi Jena et al., 2022), we infer that the increase in $(^{10}Be/^{9}Be)_{reac}$ along the continental shelf is not a result of sediment provenance change, i.e., mixing between river- and marine-sourced materials, but rather reflects seawater alteration on riverine $^{10}Be/^{9}Be$ signature through "boundary exchange". While Be is released from seafloor via submarine groundwater discharge and porewater diffusion, sediments may scavenge Be from overlying seawater either through adsorption or precipitation. We discount reversible adsorption as a significant process because the exchangeable fraction was leached before extracting the reactive fractions. Moreover, the more pronounced increase in $(^{10}Be/^{9}Be)_{am\text{-}ox}$ than $(^{10}Be/^{9}Be)_{x\text{-}ox}$ with increased $(^{10}Be/^{9}Be)_{diss}$ (Fig. 4.5) indicates that bottom sediments uptake Be from seawater most likely via precipitation of amorphous (hydr)oxides. This is consistent with the view of Wittmann et al. (2017) that the sedimentary $^{10}Be/^{9}Be$ ratios at a continental margin offshore Chile are altered by seawater through co-precipitation or irreversible adsorption, rather than reversible adsorption.

Overall, we provide evidence that "boundary exchange" processes are prevailing at the East China Sea and the Amazon continental shelves, and capable of modifying $^{10}Be/^{9}Be$ ratios in bottom seawater and sediments. For coastal bottom seawater, alterations in its $^{10}Be/^{9}Be$ ratio may be more susceptible to submarine groundwater discharge rather than porewater diffusion. For coastal bottom sediment, the inherited terrigenous $^{10}Be/^{9}Be$ signature is significantly altered on outer shelves where boundary currents prevail and the dissolved $^{10}Be/^{9}Be$ ratio exponentially increases. However, in inner shelf areas where the dissolved $^{10}Be/^{9}Be$ ratio only slightly increases, the alteration of $^{10}Be/^{9}Be$ signature in both SPM and bottom sediments by "boundary exchange" is unremarkable. The small variation (within a factor of 2) of $^{10}Be/^{9}Be$ in both am-ox and x-ox fractions from inner-shelf sediments compared to river sediments (Fig. 4.5) possibly indicate a "safe zone" (i.e., within ~150 km from the coast) where sediments may faithfully record a continental denudation signal of the adjacent river catchments with minor alteration by seawater.

4.4.2 Catchment-wide denudation rates derived from meteoric $^{10}Be/^{9}Be$ ratio of inner-shelf sediments

Prior to calculating the denudation rates for the Changjiang and Amazon catchments using inner-shelf sediments, we first explore whether the ^{10}Be fluxes exported by rivers into the ocean

from the entire Changjiang and Amazon catchments are at steady state with respect to the atmospheric ^{10}Be fluxes.

4.4.2.1 Balance of meteoric ^{10}Be input and output flux

We have calculated a flux balance for ^{10}Be that is based on equations (4.2) and (4.3). Two different estimates of this flux balance are shown in Table 4.4. The erosion rate E (in equation (4.3)) is either derived from modern sediment loads (Table 4.4) or from a longer-term *in situ* ^{10}Be -derived source area denudation rate which is calculated under the assumption that all sediment is eroded from the mountains and that production of further *in situ* cosmogenic nuclides is negligible in the floodplain (Wittmann et al., 2020).

For the Changjiang catchment, despite the large uncertainty of the GCM-derived meteoric ^{10}Be depositional flux, the meteoric ^{10}Be output quantified using *in situ*-derived denudation rate as an independent estimate of erosion rate agrees well with its input, indicating a steady state regarding the ^{10}Be flux over millennial-scale and that the GCM-derived meteoric ^{10}Be depositional flux provides a valid estimate. When compared to ^{10}Be input derived from modern, gauging sediment load, $\frac{J_{riv}^{^{10}Be}}{J_{atm}^{^{10}Be}}$ is higher than 1 (Table 4.4) before the impoundment of the Three Gorges Dam (TGD), suggesting accelerated erosion caused by intensified anthropogenic activities, such as deforestation in the Changjiang catchment since last century (e.g., Zhang and Zhu (2001)). After the impoundment of the TGD, the $\frac{J_{riv}^{^{10}Be}}{J_{atm}^{^{10}Be}}$ is much lower than 1 due to the sediment trapping in the Three Gorges Reservoir (e.g., Xu and Milliman (2009)).

For the Amazon catchment, the $\frac{J_{riv}^{^{10}Be}}{J_{atm}^{^{10}Be}}$ derived from two estimates (i.e., modern gauging and *in situ* ^{10}Be) are both lower than 1 (Table 4.4), which is in good agreement with previous results obtained by Wittmann et al. (2015) at Óbidos station close to the river mouth. Possible causes could be an overestimation of the Holocene-averaged atmospheric ^{10}Be flux, or the radioactive decay of meteoric ^{10}Be during retention in floodplain and inactive areas as discussed in Wittmann et al. (2015).

Table 4.4 Meteoric ^{10}Be flux balance in the Changjiang and Amazon catchments

Catchment	Drainage area[a]	Source area[a]	Runoff[a]	Modern river sediment load	*In situ*-Derived source area denudation rate[a]	$F_{met}^{^{10}Be}$ [d]	$J_{atm}^{^{10}Be}$ [e]	$J_{riv}^{^{10}Be}$ (Gauging)[f]	$J_{riv}^{^{10}Be}$ (*In situ*)[f]	$\frac{J_{riv}^{^{10}Be}}{J_{atm}^{^{10}Be}}$ (Gauging)[g]	$\frac{J_{riv}^{^{10}Be}}{J_{atm}^{^{10}Be}}$ (*In situ*)[g]
	($\times10^3$ km^2)	($\times10^3$ km^2)	(mm/yr)	(Mt/yr)	(mm/kyr)	($\times10^6$ at/cm^2/yr)	($\times10^{20}$ at/yr)	($\times10^{20}$ at/yr)	($\times10^{20}$ at/yr)		
Changjiang	2298.5	1756.6	500	423.6[b] (pre-TGD) /147.5[b] (post TGD)	70.2±25.7	1.86±1.50	427±342	553 ± 65 (pre-TGD) /194 ± 23 (post TGD)	419 ± 155	1.29 ± 1.04 (pre-TGD) /0.45 ± 0.36 (post TGD)	0.98 ± 0.86
Amazon	4806.1	1375.8	1000	748.6[c]	109.9±23.4	1.40±0.28	673±134	428±42	243 ± 45	0.65 ± 0.14	0.36 ± 0.10

[a] For original data sources, we refer to Wittmann et al. (2020).

[b] Gauging sediment load at Datong station (Dai and Lu, 2014), TGD: Three Gorges Dam.

[c] Average sediment load gauging at Óbidos station from 1996 to 2018 (Li et al., 2020).

[d] Basin-wide meteoric ^{10}Be flux calculated on SRTM-pixel basis using the average from an industrial (modem) and a pre-industrial (Holocene) model run (Heikkilä and von Blanckenburg, 2015). Dataset is available online (http://dx.doi.org/10.5880/GFZ.3.4.2015.001). Uncertainty is difference between two model runs.

[e] Meteoric ^{10}Be input to a basin, calculated using equation (4.2), error is derived from the uncertainty of $F_{met}^{^{10}Be}$.

[f] Meteoric ^{10}Be flux exported by the river, calculated using equation (4.3) and $[^{10}Be]_{diss}$ and $[^{10}Be]_{reac}$ data from fresh water and fresh-water SPM samples in two estuaries. For the Changjiang catchment, $[^{10}Be]_{diss}$ is taken from the mean value of w-C1S, w-C3S and w-C5B, and $[^{10}Be]_{reac}$ is from s-C5S and s-C5B (Table 4.1 and 4.2). For Amazon, $[^{10}Be]_{diss}$ is taken from w-M147_66S and $[^{10}Be]_{reac}$ is from s-M147_27S since no fresh-water SPM available (Table 4.1 and 4.2). Error calculated by propagating all 1σ uncertainties for $[^{10}Be]$, a 10% uncertainty on water discharge, and a 10% uncertainty on sediment gauging data or 1σ uncertainty for *in situ*-derived denudation rate.

[g] Error calculated by propagating the uncertainties given for $F_{met}^{^{10}Be}$ and $J_{riv}^{^{10}Be}$ (gauging) or $J_{riv}^{^{10}Be}$ (*in situ*).

4.4.2.2 Denudation rates derived from inner-shelf suspended and surficial sediments

We can now calculate the denudation rates (D_{met}) for the entire Changjiang and Amazon catchments using inner-shelf suspended and bottom sediments, and compare them with the published estimates derived from *in situ* cosmogenic ^{10}Be (D_{InSitu}). Given the well-known production rates and scaling for *in situ* cosmogenic ^{10}Be in quartz (Balco et al., 2008), D_{InSitu} serves as a benchmark to validate the reliability of D_{met}.

For the Changjiang catchment, except for a bedload sample collected from the river channel, all inner-shelf SPM and bottom sediments yield comparable D_{met}, which are slightly lower than D_{InSitu} (Fig. 4.6a and b). Note that another bedload sample C5 is excluded from the denudation rate calculation, given its distinct elemental composition (higher Fe, Mn and lower K, Al) in the "min" fraction from the rest of the Changjiang samples (Table A4.2). This sample could be contaminated due to the intense human activity in the sampling region. The D_{met} derived from freshwater SPM is lower than D_{InSitu} (Fig. 4.6a), suggesting the discrepancy between D_{InSitu} and inner-shelf sediment-derived D_{met} is not a result of "boundary exchange" altering the terrigenous $^{10}Be/^{9}Be$ signal. We speculate that the lower D_{met} may reflect the changes in erosion patterns in the Changjiang catchment caused by intense human activities since the last century (e.g., Zhang and Zhu (2001)). Numerous studies have shown that after the Three Gorges Dam in the upper reaches of the Changjiang River came into operation in 2003, suspended sediment loads from upstream watersheds have largely been reduced due to trapping in the reservoir (e.g., Xu and Milliman (2009)). Consequently, downstream-linked river channels and freshwater lakes have experienced intensified erosion (Yang et al., 2014; Zhou et al., 2016). The downstream sediments tend to exhibit higher $(^{10}Be/^{9}Be)_{am\text{-}ox}$ due to the ^{10}Be accumulation during floodplain and lake storage, and thereby higher $(^{10}Be/^{9}Be)_{reac}$ compared to upstream sediments (Wittmann et al., 2015), resulting in lower D_{met}. However, $(^{10}Be/^{9}Be)_{x\text{-}ox}$ of downstream sediment may remain unchanged compared to $(^{10}Be/^{9}Be)_{am\text{-}ox}$ due to the smaller reactive surface area of crystalline oxides than amorphous oxides (Wittmann et al., 2015). This could also explain the phenomenon that $(^{10}Be/^{9}Be)_{am\text{-}ox}$ in the Changjiang freshwater sediments is higher than $(^{10}Be/^{9}Be)_{x\text{-}ox}$ and $(^{10}Be/^{9}Be)_{diss}$ that mainly record upstream signal.

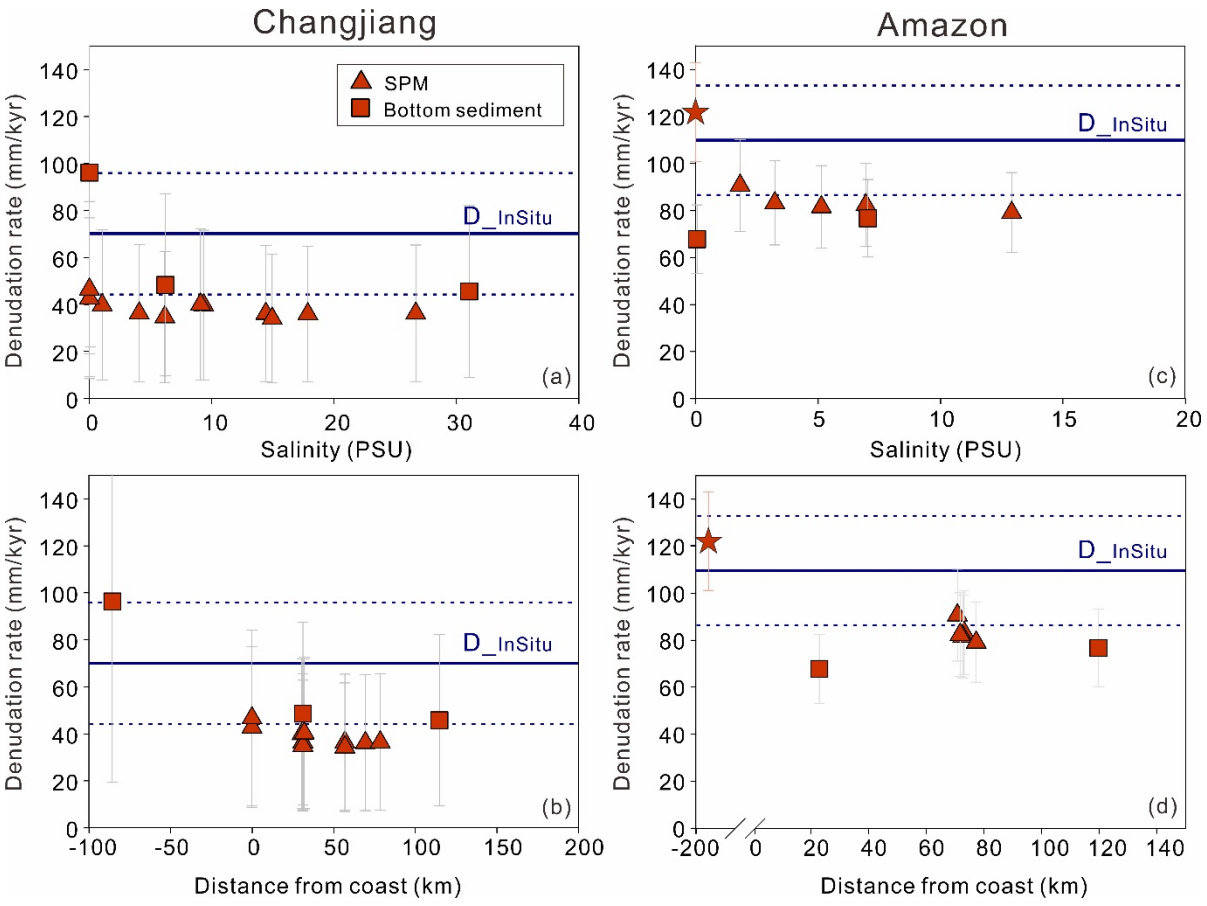

Figure 4.6 Denudation rates (D_{met}) for the Changjiang (a, b) and Amazon (c, d) catchments derived from meteoric ($^{10}Be/^{9}Be)_{reac}$ of inner-shelf (i.e., "safe zone") suspended and bottom sediments along with salinity and distance, respectively, and their comparisons with *in situ* ^{10}Be-derived denudation rates (D_{InSitu}, solid blue line, Wittmann et al. (2020)). The dashed lines represent two standard deviations (2 SD). The stars in figure (c) and (d) represent D_{met} derived from river depth-integrated SPM collected in June at Macapa station near the Amazon River mouth (Wittmann et al., 2018).

It is worth noting that the D_{met} derived from the fluvial bedload sample (C1) is nearly 2.5 times higher (~100 mm/kyr) than that derived from inner-shelf sediments (~40 mm/kyr; Fig. 4.6). Given the nearly identical $(^{10}Be/^{9}Be)_{reac}$ in bedload sample C1 and freshwater SPM (Table 4.2 and 4.3), this discrepancy is more likely a consequence of grain size bias that affects the $[^{9}Be]_{min}/[^{9}Be]_{reac}$ ratio. In short, the river bedload sample consist primarily of sand, whereas the inner-shelf SPM and bottom sediments are dominated by silty clay (section 4.2.2). $[^{9}Be]_{reac}$ is potentially enriched over $[^{9}Be]_{min}$ in fine sediments of higher adsorption capability (von Blanckenburg et al., 2012; Wittmann et al., 2012), thus resulting in a lower $[^{9}Be]_{min}/[^{9}Be]_{reac}$ in equation (4.1). To circumvent this grain size-induced bias, the recommended approach is to use river depth-integrated ^{9}Be and ^{10}Be to capture the signal of total river flux (Wittmann et al., 2018; Wittmann et al., 2015). However, this strategy can only be applied to modern sediments. For paleo-denudation rates reconstruction from coastal sediment cores, using a narrow grain-size that is most representative for bulk sediment load would be favoured.

The D_{met} for the Amazon catchment derived from inner-shelf SPM and bottom sediments are also slightly lower (~20%; ~90 mm/kyr) than D_{InSitu} (~110 mm/kyr) and lower (by a factor of about 1.5) than the D_{met} derived from river depth-integrated $(^{10}Be/^{9}Be)_{reac}$ from lower Amazon reach (~120 mm/kyr; Macapa station, near the river mouth, Wittmann et al. (2018)) (Fig. 4.6c and d). Technically, potential overestimate of $F_{met}^{^{10}Be}$ or a deficit in ^{10}Be from radioactive decay during floodplain storage in the Amazon catchment (as mentioned in section 4.4.2.1) would result in a higher D_{met} over D_{InSitu}. On the other hand, considering a potential lithologic control on denudation rate, the sand-sized quartz (lower erodibility) would also result in lower D_{InSitu} in comparison to D_{met} which is derived from fine-grained sediments generated from more rapidly eroding lithologies (e.g., shales). Therefore, if this ~20% difference is real (i.e., beyond uncertainties), it could possibly reflect the slight modification of sediment $(^{10}Be/^{9}Be)_{reac}$ ratio by "boundary exchange". Although $(^{10}Be/^{9}Be)_{reac}$ recorded in SPM is unlikely affected by exchange process via dissolution-precipitation during the short contact period between SPM and seawater, it could potentially be altered by the intense sediment resuspension on the Amazon shelf (Kuehl et al., 1986). Nevertheless, the potential "boundary exchange"-induced bias can be regarded as insignificant (within a factor of 2) within the large uncertainties typically associated with any denudation rate estimation.

To summarize, despite the potential bias resulting from grain size and seawater alteration, D_{met} derived from inner-shelf SPM and bottom sediments agree reasonably well with D_{InSitu} (within a factor of 2). This opens up the possibility of reconstructing paleo-denudation rate histories using core sediments on inner-shelf that are not subject to coastal currents.

4.5 Summary and conclusions

We provide the first systematic data for $^{10}Be/^{9}Be$ in paired coastal seawater and suspended particulate matter (SPM) samples, supplemented by bottom sediments along two coast-perpendicular transects in the Changjiang and Amazon estuaries. The dissolved $^{10}Be/^{9}Be$ shows exponential increase along the salinity gradient in both estuaries. Correspondingly, the reactive $^{10}Be/^{9}Be$ determined from SPM and bottom sediments only exhibits a slight increase (within a factor of 2) in inner-shelf areas, but increase substantially further offshore where boundary currents prevail. Our finding of a lower dissolved $^{10}Be/^{9}Be$ in hypoxic bottom Changjiang seawater compared to conservative mixing, as well as the increased reactive $^{10}Be/^{9}Be$ in outer shelf/slope bottom sediments emphasize the capacity of "boundary exchange" to modify $^{10}Be/^{9}Be$ ratios in bottom seawaters and sediments.

Locating the land-ocean transition zone where "boundary exchange" takes place is crucial to the application of $^{10}Be/^{9}Be$ in marine sedimentary records (Wittmann et al., 2017). Only in open ocean sites beyond the transition zone, the authigenic $^{10}Be/^{9}Be$ can be applied as a faithful silicate weathering proxy on a global ocean-basin scale (von Blanckenburg et al., 2015;

Willenbring and von Blanckenburg, 2010a) or as proxy for reconstructing magnetic field strength from ^{10}Be production changes (Carcaillet et al., 2004; Christl et al., 2003; Knudsen et al., 2008). On the contrary, coast-proximal sites located on the continental side of the transition zone could be considered a "safe zone" less affected by boundary currents and deeper seawater. Here, the authigenic $^{10}Be/^{9}Be$ can be applied to trace present and paleo-regional denudation rates of the adjacent river catchments. We show that in large rivers like the Changjiang and the Amazon River, this "safe zone" can extend to nearly 150 km away from the coast. However, the extent of this "safe zone" may differ between coastal environments. For example, it would be within less than 30 km from the Chile coast (Wittmann et al., 2017). Such difference is possibly determined by the water and sediment discharge from the adjacent rivers, and the distance of boundary currents from the coast. The greater freshwater discharge from the Changjiang and the Amazon River may mitigate the shoreward diffusion of seawater, which, combined with the high sedimentation in inner-shelf area, may mitigate the seawater alteration on bottom sediments. A more extensive investigation of the distribution of $^{10}Be/^{9}Be$ in various land-ocean transition environments would help us to better understand the controlling factors for the delineation of this "safe zone".

4.6 Appendix

Table A4.1 Major elemental data for suspended particulate matter (SPM) [a]

	Am-ox						X-ox						Min					
Sample ID	**Al**	**Ca**	**Fe**	**K**	**Mn**	**Na**	**Al**	**Ca**	**Fe**	**K**	**Mn**	**Na**	**Al**	**Ca**	**Fe**	**K**	**Mn**	**Na**
	all concentrations in μg/g																	
Changjiang Estuary																		
s-C5S	3431	20695	9041	218	780	52	387	353	2424	110	43	--	68338	2383	28906	19887	154	6838
s-C5B	3206	21142	8740	210	743	51	390	355	2407	111	39	--	68371	2836	28600	20111	157	8022
s-C6-1S	3797	15294	9433	365	717	91	588	328	3049	223	53	--	85017	2231	34925	24574	229	6433
s-C6-2S	4044	15432	9953	470	790	194	551	382	3221	236	54	--	81577	1461	34839	23391	160	5102
s-C6-2B	3839	17584	9658	440	783	166	485	416	2891	211	49	--	76815	1872	32034	21846	170	5942
s-C6-3S	3656	20233	9391	439	791	183	442	408	2620	200	44	--	74649	2172	31659	21486	163	7185
s-C6-3B	3312	20058	8709	380	735	160	397	419	2535	182	44	--	72087	2400	30624	20769	160	7410
s-C8S	3000	18512	7851	405	716	112	512	290	2889	211	47	--	67693	2060	25349	18327	174	5968
s-C8B	3161	18127	8154	425	737	113	531	301	2955	219	47	--	61108	1780	22622	16323	152	5199
s-C9B	3163	17606	7522	466	699	133	537	323	3154	253	53	--	75335	1544	29081	20963	185	5003
s-C10B	3196	18986	7699	513	643	121	545	274	2948	257	45	--	71960	1761	27821	20035	179	5736

Continued

	Am-ox						X-ox						Min					
Sample ID	**Al**	**Ca**	**Fe**	**K**	**Mn**	**Na**	**Al**	**Ca**	**Fe**	**K**	**Mn**	**Na**	**Al**	**Ca**	**Fe**	**K**	**Mn**	**Na**
	all concentrations in µg/g																	
Amazon Estuary																		
s-M147_27S	2655	591	9402	223	410	98	599	59	3875	155	57	--	88557	2840	27972	21183	185	6317
s-M147_28S	2765	580	9881	250	438	112	414	1	2721	114	40	--	86807	1741	27914	20486	178	5651
s-M147_29S	2677	578	9624	249	449	102	630	61	4398	178	68	--	88379	1770	28600	20527	182	5579
s-M147_30S	2449	485	8791	322	352		537	47	3556	202	50	--	74500	1765	30344	21254	187	5533
s-M147_31S	2611	505	9404	313	420	102	586	44	4101	202	63	--	85647	1504	30409	20355	184	4759

[a] A 5% uncertainty is applied for all elements that represents the long-term repeatability for ICP-OES measurements.

Table A4.2 Major elemental data for bottom sediments [a]

	Am-ox						X-ox						Min					
Sample ID	**Al**	**Ca**	**Fe**	**K**	**Mn**	**Na**	**Al**	**Ca**	**Fe**	**K**	**Mn**	**Na**	**Al**	**Ca**	**Fe**	**K**	**Mn**	**Na**
	all concentrations in μg/g																	
Changjiang Estuary																		
C1	1455	23878	4445	100	293	--	238	119	1251	46	16	238	49677	6745	23437	15498	276	13092
C5	1402	23554	4439	100	271	--	211	98	1194	40	15	211	41798	8762	76564	12274	810	10830
C6-2	2370	20794	6932	245	533	--	392	185	2029	118	30	392	58943	3977	22622	17037	191	9922
C12	2481	22362	6204	393	387	111	340	303	1790	218	26	340	65509	4026	26583	19756	220	10017
C16	2439	35594	5694	430	357	194	313	349	1811	227	22	313	61376	4540	25417	18797	247	9419
C18	2248	45346	5083	414	273	273	328	358	2062	174	23	328	53241	3346	19253	15657	167	8313
Amazon Estuary																		
M147_41	2185	111729	5477	411	411	531	233	1460	3107	269	50	--	59899	1485	33613	19409	168	4249
M147_60	685	210350	1654	156	126	1333	485	16	3472	222	42	--	22478	1137	34240	13700	134	3081
M147_67	2004	588	8319	192	239	--	59	665	2199	91	18	--	70214	2870	23260	16465	173	6725
M147_73	2468	712	9300	333	237	97	540	39	4014	194	49	--	81247	2440	27895	19121	182	6269

[a] A 5% uncertainty is applied for all elements that represents the long-term repeatability for ICP-OES measurements.

Chapter 5 Conclusions and outlook

This dissertation aims to address three main objectives: to establish an efficient procedure for seawater ^{10}Be (meteorite)/^{9}Be analysis (Chapter 2), to investigate the pathways of terrestrial ^{9}Be into the ocean and their implications for the interpretation of oceanic ^{10}Be/^{9}Be ratios (Chapter 3), and to extend the application of ^{10}Be/^{9}Be ratios at the land-ocean interface (Chapter 4). The major outcomes of the research on the three objectives in this dissertation and future directions are summarized below.

5.1 Conclusions

1. Analysis of ^{10}Be (meteoric)/^{9}Be in seawater

(1) This thesis presents the successful development of a simplified procedure to preconcentrate ^{9}Be and ^{10}Be simultaneously from seawater based on the iron co-precipitation method. In comparison to the conventional procedure which requires separate preconcentration for ^{9}Be and ^{10}Be, this new procedure is time-efficient and produces more accurate ^{10}Be/^{9}Be results.

(2) The iron co-precipitation method is capable of extracting pg/g-levels Be from seawater in the absence and presence of organic matter (<160 μM) with a recovery of 100±10%.

(3) For the determination of ^{9}Be and ^{10}Be in open ocean waters, a precision in the ^{10}Be/^{9}Be ratio (<5%) can be achieved using less than 3 L of seawater compared to more than 20 L routinely used previously. Even for coastal seawater with extremely low ^{10}Be concentrations (e.g., 100 atoms/g), an amount of 10 L seawater is sufficient.

2. Pathways of terrigenous ^{9}Be into the ocean

(4) Three land-to-ocean pathways of ^{9}Be are identified for the Changjiang Estuary: i) riverine dissolved ^{9}Be that escaped coastal scavenging, ii) ^{9}Be desorption from suspended particulate matter, and iii) coastal benthic input that involves diffusion of ^{9}Be through porewater or submarine groundwater discharge.

(5) During estuarine mixing the riverine dissolved ^{9}Be flux is potentially reduced by colloidal flocculation and biological scavenging resulting from seasonal phytoplankton blooms.

(6) The ^{9}Be flux derived by desorption from suspended particulate matter through rapid cation exchange is negligible.

(7) The benthic input potentially represents the most important contributor to the marine ^{9}Be budget and is thus crucial to the interpretation of the paleo-marine ^{10}Be/^{9}Be record. Dissolved oxygen concentration in coastal bottom water is suggested be a key factor in controlling the benthic ^{9}Be flux.

3. Setting the ^{10}Be/^{9}Be ratio at the land-ocean interface

(8) In the Changjiang and Amazon River estuaries and their adjacent coastal areas the $^{10}Be/^{9}Be$ ratios of the reactive (authigenic) phase increase by a factor of 3 to 30 in outer shelf or slope sediments relative to the original fluvial sediments. "Boundary exchange" is the process that modifies terrigenous isotopic signatures recorded in continental margin sediments. This in turn suggests that the reactive $^{10}Be/^{9}Be$ ratio in outer shelf or slope sediments can be a sensitive tracer to quantify "boundary exchange" processes.

(9) In large river-dominated shelves characterized by high sedimentation rates and less efficient shoreward seawater diffusion, a continent-derived $^{10}Be/^{9}Be$ ratio can be preserved in the reactive phase of the inner shelf sediment. Therefore, the reactive $^{10}Be/^{9}Be$ ratio in inner-shelf sediments can be a direct recorder of continental denudation in the adjacent river catchments.

5.2 Outlook

1. Contribution of submarine groundwater discharge to the marine ^{9}Be budget

Submarine groundwater discharge has been recognized as an important source of many trace elements (e.g., Fe, Sr and Nd) to the ocean (Dowling et al., 2003; Kim and Kim, 2014; Windom et al., 2006). My results show that groundwater may also contribute ^{9}Be to the ocean in an important way. Yet a framework of oceanic ^{9}Be cycling taking submarine groundwater discharge into account has still to be established. To this end, quantification of the ^{9}Be flux from this pathway is necessary to gain a full picture of the oceanic ^{9}Be cycle. This complete picture is of great importance for robust interpretations of the marine $^{10}Be/^{9}Be$ record.

2. Further investigations of the $^{10}Be/^{9}Be$ distribution at the land-ocean interface

Determining the $^{10}Be/^{9}Be$ ratio in time-series of the reactive phase of terrestrial sediment deposited on the continental shelf offers significant advantages in paleo-denudation reconstructions as this archive is independent of the less well constrained pathways affecting dissolved Be. A prerequisite is the absence of modification of the ratio in seawater. As discussed in Chapter 4, the terrestrial $^{10}Be/^{9}Be$ signature is only slightly altered by seawater (within a factor of 2) in coast-proximal sediments up to about 150 km from the Changjiang and Amazon coasts. Therefore, these inner-shelf regions can be regarded as "safe zones" where sedimentary $^{10}Be/^{9}Be$ ratios can faithfully record the denudation rates of the adjacent river catchments. However, such a "safe zone" is not observed at an ocean margin site only 30 km from the Chile coast. The extent of this "safe zone" may be controlled by a combination of many factors, such as the magnitude of the fresh water plume and boundary currents, the sedimentation rate and so on. Identifying the key controlling factors will aid us in delineating the "safe zone", thereby facilitating the reconstruction of past catchment-wide denudation history using reactive

$^{10}Be/^{9}Be$ ratio from inner-shelf sediments. To this end, broader investigations of $^{10}Be/^{9}Be$ distributions at various land-ocean transition settings are required.

Bibliography

Adebayo, S.B., Cui, M., Williams, T.J., Martin, E., Johannesson, K.H., 2022. Evolution of rare earth element and εNd compositions of Gulf of Mexico seawater during interaction with Mississippi River sediment. Geochimica et Cosmochimica Acta, 335, 231-242.

Afkhami, A., Madrakian, T., Bozorgzadeh, E., Bahram, M., 2007. Spectrophotometric determination of beryllium in water samples after micelle-mediated extraction preconcentration. Talanta, 71(3): 1103-9.

Aldahan, A., Haiping, Y., Possnert, G., 1999. Distribution of beryllium between solution and minerals (biotite and albite) under atmospheric conditions and variable pH. Chemical Geology, 156(1): 209-229.

Alderighi, L., Gans, P., Midollini, S., Vacca, A., 2000. Aqueous solution chemistry of beryllium. Advances in Inorganic Chemistry. Academic Press, pp. 109-172.

Aller, R.C. et al., 1985. Early chemical diagenesis, sediment-water solute exchange, and storage of reactive organic matter near the mouth of the Changjiang, East China Sea. Continental Shelf Research, 4(1): 227-251.

Amin, A.S., 2001. Utilization of solid phase spectrophotometry for determination of trace amounts of beryllium in natural water. Analytica Chimica Acta, 437(2): 265-272.

Anderson, R.F., 2020. GEOTRACES: Accelerating research on the marine biogeochemical cycles of trace elements and their isotopes. Annual Review of Marine Science, 12: 49-85.

Anderson, R.F. et al., 1990. Boundary scavenging in the Pacific Ocean: a comparison of ^{10}Be and ^{231}Pa. Earth and Planetary Science Letters, 96(3): 287-304.

Andersson, P.S., Porcelli, D., Gustafsson, Ö., Ingri, J., Wasserburg, G.J., 2001. The importance of colloids for the behavior of uranium isotopes in the low-salinity zone of a stable estuary. Geochimica et Cosmochimica Acta, 65(1): 13-25.

Archuleta, M.M., Duran, B., 2009. Chapter 6. Beryllium analysis by inductively coupled plasma atomic emission spectrometry and inductively coupled plasma mass spectrometry: Applications in Occupational and Environmental Hygiene, Beryllium, pp. 113-130.

Armiento, G. et al., 2013. Beryllium natural background concentration and mobility: a reappraisal examining the case of high Be-bearing pyroclastic rocks. Environmental monitoring and assessment, 185: 559-572.

Armijos, E. et al., 2016. Measuring and modeling vertical gradients in suspended sediments in the Solimões/Amazon River. Hydrological Processes, 31(3): 654-667.

Audry, S., Blanc, G., Schäfer, J., Chaillou, G., Robert, S., 2006. Early diagenesis of trace metals (Cd, Cu, Co, Ni, U, Mo, and V) in the freshwater reaches of a macrotidal estuary. Geochimica et Cosmochimica Acta, 70(9): 2264-2282.

Baes Jr, C.F., Mesmer, R.J.A.J.S., 1981. Thermodynamics of cation hydrolysis. American Journal of Science, 281(7): 935-962.

Balco, G., Stone, J.O., Lifton, N.A., Dunai, T.J., 2008. A complete and easily accessible means of calculating surface exposure ages or erosion rates from ^{10}Be and ^{26}Al measurements. Quaternary Geochronology, 3(3): 174-195.

Barrón, C., Duarte, C.M., 2015. Dissolved organic carbon pools and export from the coastal ocean. Global Biogeochemical Cycles, 29(10): 1725-1738.

Bashir, W., Paull, B., 2001. Sensitive and selective ion chromatographic method for the

determination of trace beryllium in water samples. Journal of Chromatography A, 910(2): 301-309.

Beardsley, R.C., Limeburner, R., Yu, H., Cannon, G.A., 1985. Discharge of the Changjiang (Yangtze River) into the East China Sea. Continental Shelf Research, 4(1): 57-76.

Beiraghi, A., Babaee, S., 2008. Separation and preconcentration of ultra trace amounts of beryllium in water samples using mixed micelle-mediated extraction and determination by inductively coupled plasma-atomic emission spectrometry. Analytical Chimica Acta, 607(2): 183-90.

Bernhardt, A. et al., 2020. $^{10}Be/^{9}Be$ ratios reveal marine authigenic clay formation. Geophysical Research Letters, 47(4): e2019GL086061.

Boschi, V., Willenbring, J.K., 2016. The effect of pH, organic ligand chemistry and mineralogy on the sorption of beryllium over time. Environmental Chemistry, 13(4): 711-722.

Bourlès, D., Raisbeck, G.M., Yiou, F., 1989a. ^{10}Be and ^{9}Be in marine sediments and their potential for dating. Geochimica et Cosmochimica Acta, 53(2): 443-452.

Bourlès, D. et al., 1989b. Beryllium in marine pore waters: geochemical and geochronological implications. Nature, 341(6244): 731-733.

Bourlès, D. et al., 1994. Examination of hydrothermal influences on oceanic beryllium using fluids, plume particles and sediments from the TAG hydrothermal field. Earth and Planetary Science Letters 122.1-2 (1994): 143-157.

Boyle, E.A., Edmond, J.M., Sholkovitz, E.R., 1977. The mechanism of iron removal in estuaries. Geochimica et Cosmochimica Acta, 41(9): 1313-1324.

Brown, E.T. et al., 1992a. Beryllium isotope geochemistry in tropical river basins. Geochimica et Cosmochimica Acta, 56(4): 1607-1624.

Brown, E.T. et al., 1992b. Continental inputs of beryllium to the oceans. Earth and Planetary Science Letters, 114(1): 101-111.

Brunauer, S., Emmett, P.H., Teller, E.J.J.o.t.A.c.s., 1938. Adsorption of gases in multimolecular layers. Journal of the American chemical society, 60(2): 309-319

Burnett, W.C., Taniguchi, M., Oberdorfer, J., 2001. Measurement and significance of the direct discharge of groundwater into the coastal zone. Journal of Sea Research, 46(2): 109-116.

Callède, J. et al., 2010. Les apports en eau de l'Amazone à l'Océan Atlantique. Revue des sciences de l'eau, 23(3): 247-273.

Cao, Z. et al., 2021. Stable barium isotope dynamics during estuarine mixing. Geophysical Research Letters, 48(19): e2021GL095680.

Carcaillet, J., Bourlès, D.L., Thouveny, N., Arnold, M., 2004. A high resolution authigenic $^{10}Be/^{9}Be$ record of geomagnetic moment variations over the last 300 ka from sedimentary cores of the Portuguese margin. Earth and Planetary Science Letters, 219(3-4): 397-412.

Carpenter, J.H., 1965. The Chesapeake Bay institute technique for the Winkler dissolved oxygen method. Limnology and Oceanography, 10(1): 141-143.

Carroll, J., Falkner, k.K., Brown, E.T., Moore, W.S., 1993. The role of the Ganges-Brahmaputra mixing zone in supplying barium and ^{226}Ra to the Bay of Bengal. Geochimica et Cosmochimica Acta, 57(13): 2981-2990.

Caves Rugenstein, J.K., Ibarra, D.E., von Blanckenburg, F., 2019. Neogene cooling driven by land surface reactivity rather than increased weathering fluxes. Nature, 571(7763): 99-

102.

Charette, M.A. et al., 2016. Coastal ocean and shelf-sea biogeochemical cycling of trace elements and isotopes: lessons learned from GEOTRACES. Philosophical Transactions of the Royal Society A: Mathematical, Physical and Engineering Sciences, 374(2081): 20160076.

Chen, C.-T.A., Liu, K.-K., Macdonald, R., 2003. Continental Margin Exchanges. In: Fasham, M.J.R. (Ed.), Ocean Biogeochemistry: The Role of the Ocean Carbon Cycle in Global Change. Springer Berlin Heidelberg, Berlin, Heidelberg, pp. 53-97.

Chen, M. et al., 2023. Boundary exchange completes the marine Pb cycle jigsaw. Proceedings of the National Academy of Sciences, 120(6): e2213163120.

Christl, M., Strobl, C., Mangini, A., 2003. Beryllium-10 in deep-sea sediments: a tracer for the Earth's magnetic field intensity during the last 200,000 years. Quaternary Science Reviews, 22(5-7): 725-739.

Coffey, M. et al., 1997. The behaviour of dissolved barium in estuaries. Estuarine, Coastal and Shelf Science, 45(1): 113-121.

Colbert, D., McManus, J., 2005. Importance of seasonal variability and coastal processes on estuarine manganese and barium cycling in a Pacific Northwest estuary. Continental Shelf Research, 25(11): 1395-1414.

Dai, S.B., Lu, X.X., 2014. Sediment load change in the Yangtze River (Changjiang): A review. Geomorphology, 215: 60-73.

Dannhaus, N., Wittmann, H., Krám, P., Christl, M., von Blanckenburg, F., 2018. Catchment-wide weathering and erosion rates of mafic, ultramafic, and granitic rock from cosmogenic meteoric $^{10}Be/^{9}Be$ ratios. Geochimica et Cosmochimica Acta, 222: 618-641.

de Bruin, H., Fardy, J., Temple, R., 1963. The ion-exchange behaviour of beryllium salicylate complexes. Australian Journal of Chemistry. 16(3): 376-391.

Deng, K. et al., 2023. Dominance of benthic fluxes in the oceanic beryllium budget and implications for paleo-denudation records. Science Advances, 9(23): eadg3702.

Deng, K., Wittmann, H., Hsieh, M.-L., Yang, S., von Blanckenburg, F., 2021. Deposition and retention of meteoric ^{10}Be in Holocene Taiwan river terraces. Quaternary Science Reviews, 265: 107048.

Deng, K., Wittmann, H., von Blanckenburg, F., 2020. The depositional flux of meteoric cosmogenic ^{10}Be from modeling and observation. Earth and Planetary Science Letters, 550: 116530.

Deng, K., Yang, S., Du, J., Lian, E., Vance, D., 2022. Dominance of benthic flux of REEs on continental shelves: implications for oceanic budgets. Geochemical Perspectives Letters, 22: 26-30.

Dewald, A. et al., 2013. CologneAMS, a dedicated center for accelerator mass spectrometry in Germany. Nuclear Instruments and Methods in Physics Research Section B: Beam Interactions with Materials and Atoms, 294: 18-23.

Dixon, J.L., Chadwick, O.A., Pavich, M.J., 2018. Climatically controlled delivery and retention of meteoric ^{10}Be in soils. Geology, 46(10): 899-902.

Dowling, C.B., Poreda, R.J., Basu, A.R., 2003. The groundwater geochemistry of the Bengal Basin: Weathering, chemsorption, and trace metal flux to the oceans. Geochimica et Cosmochimica Acta, 67(12): 2117-2136.

Dunne, T., Mertes, L.A.K., Meade, R.H., Richey, J.E., Forsberg, B.R., 1998. Exchanges of sediment between the flood plain and channel of the Amazon River in Brazil. GSA

Bulletin, 110(4): 450-467.

Elrod, V.A., Berelson, W.M., Coale, K.H., Johnson, K.S., 2004. The flux of iron from continental shelf sediments: A missing source for global budgets. Geophysical Research Letters, 31(12): L12307.

Everest, D.A.J., 1964. The chemistry of beryllium. Elsevier Pub. Co.

Field, C.V., Schmidt, G.A., Koch, D., Salyk, C., 2006. Modeling production and climate-related impacts on ^{10}Be concentration in ice cores. Journal of Geophysical Research, 111: D15107.

Flagg, C.N., Gordon, R.L., McDowell, S., 1986. Hydrographic and current observations on the continental slope and shelf of the western equatorial atlantic. Journal of Physical Oceanography. 16(8): 1412-1429

Frank, M. et al., 2009. The dissolved Beryllium isotope composition of the Arctic Ocean. Geochimica et Cosmochimica Acta, 73(20): 6114-6133.

Frank, M., Rutgers van der Loeff, M.M., Kubik, P.W., Mangini, A., 2002. Quasi-conservative behaviour of ^{10}Be in deep waters of the Weddell Sea and the Atlantic sector of the Antarctic Circumpolar Current. Earth and Planetary Science Letters, 201(1): 171-186.

Froelich, P.N. et al., 1979. Early oxidation of organic matter in pelagic sediments of the eastern equatorial Atlantic: suboxic diagenesis. Geochimica et Cosmochimica Acta, 43(7): 1075-1090.

Gallo, M.N., Vinzon, S.B., 2017. Estudo numérico do escoamento em planícies de marés do canal Norte (estuário do rio Amazonas). Ribagua, 2(1): 38-50.

Gledhill, M. et al., 2022. Trace metal stoichiometry of dissolved organic matter in the Amazon plume. 8(31): eabm2249.

Graham, I., Ditchburn, R., Barry, B., 2003. Atmospheric deposition of ^{7}Be and ^{10}Be in New Zealand rain (1996-98). Geochimica et Cosmochimica Acta, 67(3): 361-373.

Graly, J.A., Reusser, L.J., Bierman, P.R., 2011. Short and long-term delivery rates of meteoric ^{10}Be to terrestrial soils. Earth and Planetary Science Letters, 302(3-4): 329-336.

Guo, X. et al., 2020. Does submarine groundwater discharge contribute to summer hypoxia in the Changjiang (Yangtze) River Estuary? Science of the Total Environment, 719: 137450.

Hancock, G.J., Murray, A.S., 1996. Source and distribution of dissolved radium in the Bega River estuary, Southeastern Australia. Earth and Planetary Science Letters, 138(1): 145-155.

Hansell, D.A., Carlson, C.A., Repeta, D.J., Schlitzer, R., 2009. Dissolved organic matter in the ocean: A controversy stimulates new insights. Oceanography, 22(4): 202-211.

Hayes, C.T. et al., 2013. Quantifying lithogenic inputs to the North Pacific Ocean using the long-lived thorium isotopes. Earth and Planetary Science Letters, 383: 16-25.

Heikkilä, U., Beer, J., Alfimov, V., 2008. Beryllium-10 and beryllium-7 in precipitation in Dü bendorf (440 m) and at Jungfraujoch (3580 m), Switzerland (1998–2005). Journal of Geophysical Research: Atmospheres, 113: 1-10.

Heikkilä, U., Phipps, S.J., Smith, A.M., 2013. ^{10}Be in late deglacial climate simulated by ECHAM5-HAM – Part 1: Climatological influences on ^{10}Be deposition. Climate of the Past, 9(6): 2641-2649.

Heikkilä, U., Smith, A.M., 2013. Production rate and climate influences on the variability of ^{10}Be deposition simulated by ECHAM5-HAM: Globally, in Greenland, and in

Antarctica. Journal of Geophysical Research: Atmospheres, 118(6): 2506-2520.

Heikkilä, U., von Blanckenburg, F., 2015. The global distribution of Holocene meteoric ^{10}Be fluxes from atmospheric models: Distribution maps for terrestrial Earth's surface applications. GFZ Data Services, 10.

Hiraide, M., Ishikawa, K., Chen, Z.S., Kawaguchi, H., 1994. Coprecipitation with metal hydroxides for the determination of beryllium in seawater by graphite furnace atomic absorption spectrometry. Microchimica Acta, 117(1): 7-13.

Homoky, W.B. et al., 2016. Quantifying trace element and isotope fluxes at the ocean–sediment boundary: a review. Philosophical Transactions of the Royal Society A: Mathematical, Physical and Engineering Sciences, 374(2081): 20161246.

Horlick, S.H.T.a.G., 1987. Matrix-effect observations in inductively coupled plasma mass spectrometry. Journal of Analytical Atomic Spectrometry, 2(8): 745-763.

Huang, X. et al., 2020. Detrital zircon U-Pb ages in the East China Seas: implications for provenance analysis and sediment budgeting. Minerals, 10(5), 398.

Hunter, K.A., Leonard, M.W., 1988. Colloid stability and aggregation in estuaries: 1. Aggregation kinetics of riverine dissolved iron after mixing with seawater. Geochimica et Cosmochimica Acta, 52(5): 1123-1130.

Jang, K., Huh, Y., Han, Y., 2017. Authigenic Nd isotope record of North Pacific Intermediate Water formation and boundary exchange on the Bering Slope. Quaternary Science Reviews, 156: 150-163.

Jeandel, C., 2016. Overview of the mechanisms that could explain the 'Boundary Exchange' at the land-ocean contact. Philosophical Transactions of the Royal Society A: Mathematical, Physical and Engineering Sciences, 374(2081), 20150287.

Jeandel, C., Arsouze, T., Lacan, F., Téchiné, P., Dutay, J.C., 2007. Isotopic Nd compositions and concentrations of the lithogenic inputs into the ocean: A compilation, with an emphasis on the margins. Chemical Geology, 239(1-2): 156-164.

Jeandel, C., Oelkers, E.H., 2015. The influence of terrigenous particulate material dissolution on ocean chemistry and global element cycles. Chemical Geology, 395: 50-66.

Jiang, X., Lu, B., He, Y., 2013. Response of the turbidity maximum zone to fluctuations in sediment discharge from river to estuary in the Changjiang Estuary (China). Estuarine, Coastal and Shelf Science, 131: 24-30.

Kawaguchi, H., Tanaka, T., Nakamura, T., Morishita, M., Mizuike, A., 1987. Matrix effects in inductively coupled plasma mass spectrometry. Analytical Sciences, 3(4): 305-308.

Kim, I., Kim, G., 2014. Submarine groundwater discharge as a main source of rare earth elements in coastal waters. Marine Chemistry, 160: 11-17.

Kineke, G.C., Sternberg, R.W., Trowbridge, J.H., Geyer, W.R., 1996. Fluid-mud processes on the Amazon continental shelf. Continental Shelf Research, 16(5): 667-696.

Klein, M.G., Dewald, A., Gottdang, A., Heinze, S., Mous, D.J.W., 2011. A new HVE 6MVAMS system at the University of Cologne. Nuclear Instruments and Methods in Physics Research Section B: Beam Interactions with Materials and Atoms, 269(24): 3167-3170.

Knudsen, M.F., Henderson, G.M., Frank, M., Mac Niocaill, C., Kubik, P.W., 2008. In-phase anomalies in Beryllium-10 production and palaeomagnetic field behaviour during the Iceland Basin geomagnetic excursion. Earth and Planetary Science Letters, 265(3-4): 588-599.

Kong, W., Zhou, L., Aumaître, G., Bourlès, D., Keddadouche, K., 2021a. Dissolved and particulate beryllium isotopes in the Pearl River Estuary: Their Geochemical Behavior

in Estuarine Water and Potential Contributions From Anthropogenic Sources. Frontiers in Marine Science, 8: 689890.

Kong, W.Y., Zhou, L.P., AsterTeam, 2021b. Tracing water masses and assessing boundary scavenging intensity with beryllium isotopes in the Northern South China Sea. Journal of Geophysical Research: Oceans, 126(7): e2021JC017236.

Koschinsky, A. et al., 2018. Interactions of trace metals, DOM, and particles in the Amazon estuary and associated plume as key processes for trace metal and DOM fluxes into the Atlantic, Cruise No. M147, April 19 - May 21, 2018, Las Palmas (Gran Canaria) - Belém (Brazil). METEOR-Berichte, M147, Gutachterpanel Forschungsschiffe: 1-63.

Kosuth, P. et al., 2009. Sea-tide effects on flows in the lower reaches of the Amazon River. Hydrological Processes: An International Journal. 23(22): 3141-3150.

Ku, T.L. et al., 1990. Beryllium isotope distribution in the western North Atlantic: a comparison to the Pacific. Deep Sea Research Part A. Oceanographic Research Papers, 37(5): 795-808.

Kuehl, S.A., DeMaster, D.J., Nittrouer, C.A., 1986. Nature of sediment accumulation on the Amazon continental shelf. Continental Shelf Research, 6(1): 209-225.

Kuehl, S.A., Nittrouer, C.A., DeMaster, D.J., 1982. Modern sediment accumulation and strata formation on the Amazon continental shelf. Marine Geology, 49(3): 279-300.

Kusakabe, M., Ku, T.-L., Southon, J.R.J.G.J., 1990. Beryllium isotopes in the ocean. Geochemical Journal, 24(4), 263-272.

Kusakabe, M. et al., 1991. Be isotopes in rivers/estuaries and their oceanic budgets. Earth and Planetary Science Letters, 102(3–4): 265-276.

Kusakabe, M. et al., 1987. Distribution of ^{10}Be and ^{9}Be in the Pacific Ocean. Earth and Planetary Science Letters, 82(3): 231-240.

Lacan, F., Jeandel, C., 2005. Neodymium isotopes as a new tool for quantifying exchange fluxes at the continent–ocean interface. Earth and Planetary Science Letters, 232(3-4): 245-257.

Lal, D., Peters, B., 1967. Cosmic Ray Produced Radioactivity on the Earth. In: Sitte, K. (Ed.), Kosmische Strahlung II/Cosmic Rays II. Springer Berlin Heidelberg, Berlin, Heidelberg, pp. 551-612.

Lee, H.-J., Chao, S.-Y., 2003. A climatological description of circulation in and around the East China Sea. Deep Sea Research Part II: Topical Studies in Oceanography, 50(6-7): 1065-1084.

Li, J., Zhang, C., 1998. Sediment resuspension and implications for turbidity maximum in the Changjiang Estuary. Marine Geology, 148(3): 117-124.

Li, L., Zhong, Q., Du, J., 2021a. Radium desorption behavior of riverine suspended sediment: Theoretical and experimental. Journal of Environmental Radioactivity, 234: 106644.

Li, S., Goldstein, S.L., Raymo, M.E., 2021b. Neogene continental denudation and the beryllium conundrum. Proceedings of the National Academy of Sciences, 118(42): e2026456118.

Li, S., Goldstein, S.L., Raymo, M.E., 2022. Reply to von Blanckenburg et al.: We provide a solution to the Neogene beryllium conundrum. Proceedings of the National Academy of Sciences, 119(35): e2208945119.

Li, T., Wang, S., Liu, Y., Fu, B., Gao, D., 2020. Reversal of the sediment load increase in the Amazon basin influenced by divergent trends of sediment transport from the Solimões and Madeira Rivers. Catena, 195: 104804.

Li, Y.-H., Burkhardt, L., Buchholtz, M., O'Hara, P., Santschi, P.H., 1984a. Partition of radiotracers between suspended particles and seawater. Geochimica et Cosmochimica Acta, 48(10): 2011-2019.

Li, Y.-H., Burkhardt, L., Teraoka, H., 1984b. Desorption and coagulation of trace elements during estuarine mixing. Geochimica et Cosmochimica Acta, 48(10): 1879-1884.

Lian, E. et al., 2016. Kuroshio subsurface water feeds the wintertime Taiwan Warm Current on the inner East China Sea shelf. Journal of Geophysical Research: Oceans, 121(7): 4790-4803.

Lin, J., He, Q., Guo, L., van Prooijen, B.C., Wang, Z.B., 2020. An integrated optic and acoustic (IOA) approach for measuring suspended sediment concentration in highly turbid environments. Marine Geology, 421: 106062.

Liu, J. et al., 2020. Sedimentary phosphorus cycling and budget in the seasonally hypoxic coastal area of Changjiang Estuary. Science of the Total Environment, 713: 136389.

Liu, J.P. et al., 2006. Sedimentary features of the Yangtze River-derived along-shelf clinoform deposit in the East China Sea. Continental Shelf Research, 26(17-18): 2141-2156.

Liu, Q. et al., 2022. Significance of nutrients in oxygen-depleted bottom waters via various origins on the mid-outer shelf of the East China Sea during summer. Science of the Total Environment, 826: 154083.

Lohan, M.C., Bruland, K.W., 2008. Elevated Fe(II) and Dissolved Fe in Hypoxic Shelf Waters off Oregon and Washington: An Enhanced Source of Iron to Coastal Upwelling Regimes. Environmental Science & Technology, 42(17): 6462-6468.

Luo, S., Ku, T.-L., 2004. On the importance of opal, carbonate, and lithogenic clays in scavenging and fractionating ^{230}Th, ^{231}Pa and ^{10}Be in the ocean. Earth and Planetary Science Letters, 220(1-2): 201-211.

Luo, X.X., Yang, S.L., Zhang, J., 2012. The impact of the Three Gorges Dam on the downstream distribution and texture of sediments along the middle and lower Yangtze River (Changjiang) and its estuary, and subsequent sediment dispersal in the East China Sea. Geomorphology, 179: 126-140.

Mackenzie, F.T., De Carlo, E.H., Lerman, A., 2011. Coupled C, N, P, and O Biogeochemical Cycling at the Land–Ocean Interface, Treatise on Estuarine and Coastal Science, pp. 317-342.

Mallick, D., Wang, X., Beebe, D.A., 2022. Impact of estuaries on fluvial Cr input into the ocean: Perspectives from the Mobile Bay Estuary, Northern Gulf of Mexico. Geochimica et Cosmochimica Acta, 334: 187-200.

Martin, J.M., Guan, D.M., Elbaz-Poulichet, F., Thomas, A.J., Gordeev, V.V., 1993. Preliminary assessment of the distributions of some trace elements (As, Cd, Cu, Fe, Ni, Pb and Zn) in a pristine aquatic environment: The Lena River estuary (Russia). Marine Chemistry, 43(1): 185-199.

Martinez, J.M., Guyot, J.L., Filizola, N., Sondag, F., 2009. Increase in suspended sediment discharge of the Amazon River assessed by monitoring network and satellite data. Catena, 79(3): 257-264.

Masarik, J., Beer, J., 2009. An updated simulation of particle fluxes and cosmogenic nuclide production in the Earth's atmosphere. Journal of Geophysical Research, 114: D11103.

McHargue, L.R., Damon, P.E., 1991. The global beryllium-10 cycle. Reviews of Geophysics, 29(2): 141-158.

Meade, R.H., Dunne, T., Richey, J.E., Santos, U.d.M., Salati, E., 1985. Storage and

remobilization of suspended sediment in the lower Amazon River of Brazil. Science, 228(4698): 488-490.

Measures, C.I., Edmond, J.M., 1982. Beryllium in the water column of the central North Pacific. Nature, 297(5861): 51-53.

Measures, C.I., Edmond, J.M., 1983. The geochemical cycle of ^{9}Be: a reconnaissance. Earth and Planetary Science Letters, 66(66): 101-110.

Measures, C.I., Edmond, J.M., 1986. Determination of beryllium in natural waters in real time using electron capture detection gas chromatography. Analytical Chemistry, 58(9): 2065-2069.

Measures, C.I. et al., 1996. The distribution of ^{10}Be and ^{9}Be in the South Atlantic. Deep Sea Research Part I: Oceanographic Research Papers, 43(7): 987-1009.

Ménabréaz, L. et al., 2011. The Laschamp geomagnetic dipole low expressed as a cosmogenic ^{10}Be atmospheric overproduction at ~ 41 ka. Earth and Planetary Science Letters, 312(3-4): 305-317.

Ménabréaz, L., Thouveny, N., Bourlès, D.L., Vidal, L., 2014. The geomagnetic dipole moment variation between 250 and 800 ka BP reconstructed from the authigenic ^{10}Be/^{9}Be signature in West Equatorial Pacific sediments. Earth and Planetary Science Letters, 385: 190-205.

Merschel, G., Bau, M., Dantas, E.L., 2017. Contrasting impact of organic and inorganic nanoparticles and colloids on the behavior of particle-reactive elements in tropical estuaries: An experimental study. Geochimica et Cosmochimica Acta, 197: 1-13.

Millero, F.J., Sotolongo, S., Izaguirre, M., 1987. The oxidation kinetics of Fe(II) in seawater. Geochimica et Cosmochimica Acta, 51(4): 793-801.

Milliman, J.D., Farnsworth, K.L., 2011. River Discharge to the Coastal Ocean – A Global Synthesis. Cambridge University Press, 2013.

Milliman, J.D., Huang-ting, S., Zuo-sheng, Y., H. Mead, R., 1985. Transport and deposition of river sediment in the Changjiang estuary and adjacent continental shelf. Continental Shelf Research, 4(1): 37-45.

Milliman, J.D., Summerhayes, C.P., Barretto, H.T., 1975. Quaternary Sedimentation on the Amazon Continental Margin: A Model. GSA Bulletin, 86(5): 610-614.

Molina-Kescher, M., Frank, M., Hathorne, E.C., 2014. Nd and Sr isotope compositions of different phases of surface sediments in the South Pacific: Extraction of seawater signatures, boundary exchange, and detrital/dust provenance. Geochemistry, Geophysics, Geosystems, 15(9): 3502-3520.

Monaghan, M.C., Krishnaswami, S., Turekian, K.K., 1986. The global-average production rate of ^{10}Be. Earth and Planetary Science Letters, 76(3): 279-287.

Moore, W.S., 1996. Large groundwater inputs to coastal waters revealed by ^{226}Ra enrichments. Nature, 380(6575): 612-614.

Moore, W.S., 2010. The effect of submarine groundwater discharge on the ocean. Annual Review of Marine Science, 2: 59-88.

Mosley, L.M., Liss, P.S., 2020. Particle aggregation, pH changes and metal behaviour during estuarine mixing: review and integration. Marine and Freshwater Research, 71(3): 300-310.

Müller, A.M. et al., 2008. ^{10}Be AMS measurements at low energies (E<1MeV). Nuclear Instruments and Methods in Physics Research Section B: Beam Interactions with Materials and Atoms, 266(10): 2207-2212.

Nittrouer, C.A., Sharara, M.T., DeMaster, D.J., 1983. Variations of sediment texture on the Amazon continental shelf. Journal of Sedimentary Research, 53(1): 179-191.

Óvári, M., Csukás, M., Záray, G., 2001. Speciation of beryllium, nickel, and vanadium in soil samples from Csepel Island, Hungary. Fresenius' Journal of Analytical Chemistry, 370(6): 768-775.

Petit, J.C.J. et al., 2015. The estuarine geochemical reactivity of Zn isotopes and its relevance for the biomonitoring of anthropogenic Zn and Cd contaminations from metallurgical activities: Example of the Gironde fluvial-estuarine system, France. Geochimica et Cosmochimica Acta, 170: 108-125.

Pogge von Strandmann, P.A.E. et al., 2011. Transport and exchange of U-series nuclides between suspended material, dissolved load and colloids in rivers draining basaltic terrains. Earth and Planetary Science Letters, 301(1-2): 125-136.

Renner, R.M., 1989. On the resolution of compositional datasets into convex combinations of extreme vectors. Ph.D. thesis, Victoria University of Wellington, Wellington.

Rhee, H.H. et al., 2022. Spatial variations of authigenic beryllium isotopes in surface sediments of the Antarctic oceans: a proxy for sea ice dynamics and sedimentary environments. Geosciences Journal, 26(4), 455-467.

Rockwell Geyer, W. et al., 1996. Physical oceanography of the Amazon shelf. Continental Shelf Research, 16(5): 575-616.

Rousseau, T.C. et al., 2015. Rapid neodymium release to marine waters from lithogenic sediments in the Amazon estuary. Nature Communication, 6: 7592.

Ryan, J.G., 2002. Trace-element systematics of beryllium in terrestrial materials. Reviews in Mineralogy and Geochemistry, 50(1): 121-145.

Samanta, S., Dalai, T.K., 2016. Dissolved and particulate Barium in the Ganga (Hooghly) River estuary, India: Solute-particle interactions and the enhanced dissolved flux to the oceans. Geochimica et Cosmochimica Acta, 195: 1-28.

Sarathi Jena, P., Bhushan, R., Ajay, S., Sudheer, A.K., 2022. Spatial heterogeneity in beryllium isotopic distribution in the Indian Ocean. Geochimica et Cosmochimica Acta, 342: 128-136.

Savranskaia, T. et al., 2021. Disentangling magnetic and environmental signatures of sedimentary $^{10}Be/^{9}Be$ records. Quaternary Science Reviews, 257, 106809.

SCOR Group, 2007. GEOTRACES–An international study of the global marine biogeochemical cycles of trace elements and their isotopes. Geochemistry, 67(2): 85-131.

Severmann, S., McManus, J., Berelson, W.M., Hammond, D.E., 2010. The continental shelf benthic iron flux and its isotope composition. Geochimica et Cosmochimica Acta, 74(14): 3984-4004.

Shen, H., 1985. The time and genetic model of the relict sediment on the continental shelf of East China Sea. Acta Oceanologica Sinica, 7(1): 67-77.

Shi, X. et al., 2019. Large benthic fluxes of dissolved iron in China coastal seas revealed by $^{224}Ra/^{228}Th$ disequilibria. Geochimica et Cosmochimica Acta, 260: 49-61.

Sholkovitz, E., Szymczak, R., 2000. The estuarine chemistry of rare earth elements: comparison of the Amazon, Fly, Sepik and the Gulf of Papua systems. Earth and Planetary Science Letters, 179(2): 299-309.

Sholkovitz, E.R., Boyle, E.A., Price, N.B., 1978. The removal of dissolved humic acids and iron during estuarine mixing. Earth and Planetary Science Letters, 40(1): 130-136.

Shravanraj, K., Rejith, R.G., Sundararajan, M., 2021. Evaluation of heavy metals in coastal aquifers and seawater, Remote Sensing of Ocean and Coastal Environments, pp. 155-176.

Simon, Q. et al., 2018. Increased production of cosmogenic ^{10}Be recorded in oceanic sediment sequences: Information on the age, duration, and amplitude of the geomagnetic dipole moment minimum over the Matuyama–Brunhes transition. Earth and Planetary Science Letters, 489: 191-202.

Simon, Q. et al., 2016. Authigenic ^{10}Be/^{9}Be ratios and ^{10}Be-fluxes ($^{230}Th_{xs\text{-}normalized}$) in central Baffin Bay sediments during the last glacial cycle: Paleoenvironmental implications. Quaternary Science Reviews, 140: 142-162.

Simon, Q., Thouveny, N., Bourlès, D.L., Valet, J.-P., Bassinot, F., 2020. Cosmogenic ^{10}Be production records reveal dynamics of geomagnetic dipole moment (GDM) over the Laschamp excursion (20–60 ka). Earth and Planetary Science Letters, 550: 116547.

Spiegel, T. et al., 2021. Updated estimates of sedimentary potassium sequestration and phosphorus release on the Amazon shelf. Chemical Geology, 560: 120017.

Sproson, A.D., Yokoyama, Y., Miyairi, Y., Aze, T., Totten, R.L., 2022. Holocene melting of the West Antarctic Ice Sheet driven by tropical Pacific warming. Nature Communication, 13(1): 2434.

Stier, P. et al., 2005. The aerosol-climate model ECHAM5-HAM. Atmospheric Chemistry and Physics, 5(4): 1125-1156.

Su, J.L., 2001. A review of circulation dynamics of the coastal oceans near China. Acta Oceanologica Sinica, 23(3): 1-16.

Suhrhoff, T.J., Rickli, J., Crocket, K., Bura-Nakic, E., Vance, D., 2019. Behavior of beryllium in the weathering environment and its delivery to the ocean. Geochimica et Cosmochimica Acta, 265: 48-68.

Sunda, W.G., 2012. Feedback interactions between trace metal nutrients and phytoplankton in the ocean. Frontiers in Microbiology, 3: 204.

Sunda, W.G., Huntsman, S.A., 1987. Microbial oxidation of manganese in a North Carolina estuary 1. Limnology and Oceanography, 32(3): 552-564.

Suter, M. Accelerator mass spectrometry: State of the art in 1990. Nuclear Instruments and Methods in Physics Research Section B: Beam Interactions with Materials and Atoms, 52(3): 211-223.

Takahashi, Y., Minai, Y., Ambe, S., Makide, Y., Ambe, F., 1999. Comparison of adsorption behavior of multiple inorganic ions on kaolinite and silica in the presence of humic acid using the multitracer technique. Geochimica et Cosmochimica Acta, 63(6): 815-836.

Tazoe, H., Yamagata, T., Obata, H., Nagai, H., 2014. Determination of picomolar beryllium levels in seawater with inductively coupled plasma mass spectrometry following silica-gel preconcentration. Analytical Chimica Acta, 852: 74-81.

Tipper, E.T. et al., 2021. Global silicate weathering flux overestimated because of sediment-water cation exchange. Proceedings of the National Academy of Sciences, 118(1): e2016430118.

Tomczak, M., 1981. A multi-parameter extension of temperature/salinity diagram techniques for the analysis of non-isopycnal mixing. Progress in Oceanography, 10(3): 147-171.

Vaquer-Sunyer, R., Duarte, C.M., 2008. Thresholds of hypoxia for marine biodiversity. Proceedings of the National Academy of Sciences, 105(40): 15452-15457.

Vesely, J. et al., 2002. Environmental chemistry of beryllium. Reviews in Mineralogy and

Geochemistry, 50(1): 291-317.

Vogel, J.S., Turteltaub, K.W., Finkel, R., Nelson, D.E.J.A.c., 1995. Accelerator mass spectrometry. Analytical chemistry, 67(11): 353A-359A.

von Blanckenburg, F., Bouchez, J., 2014. River fluxes to the sea from the ocean's $^{10}Be/^{9}Be$ ratio. Earth and Planetary Science Letters, 387: 34-43.

von Blanckenburg, F., Bouchez, J., Ibarra, D.E., Maher, K., 2015. Stable runoff and weathering fluxes into the oceans over Quaternary climate cycles. Nature Geoscience, 8(7): 538-542.

von Blanckenburg, F., Bouchez, J., Willenbring, J.K., Ibarra, D.E., Rugenstein, J.K.C., 2022. There is no Neogene denudation conundrum. Proceedings of the National Academy of Sciences, 119(35): e2202387119.

von Blanckenburg, F., Bouchez, J., Wittmann, H., 2012. Earth surface erosion and weathering from the ^{10}Be (meteoric)/^{9}Be ratio. Earth and Planetary Science Letters, 351-352: 295-305.

von Blanckenburg, F., Igel, H., 1999. Lateral mixing and advection of reactive isotope tracers in ocean basins: observations and mechanisms. Earth and Planetary Science Letters, 169(1): 113-128.

von Blanckenburg, F., O'Nions, R.K., Belshaw, N.S., Gibb, A., Hein, J.R., 1996. Global distribution of beryllium isotopes in deep ocean water as derived from Fe-Mn crusts. Earth and Planetary Science Letters, 141(1): 213-226.

von Blanckenburg, F., Wittmann, H., Schuessler, J.A., 2016. HELGES: Helmholtz Laboratory for the Geochemistry of the Earth Surface. Journal of large-scale research facilities JLSRF, 2.

Walsh, J.J., 1991. Importance of continental margins in the marine biogeochemical cycling of carbon and nitrogen. Nature, 350(6313): 53-55.

Wang, R. et al., 2022. Boundary processes and neodymium cycling along the Pacific margin of West Antarctica. Geochimica et Cosmochimica Acta, 327: 1-20.

Wang, Z., Yang, S., Zhang, Z., He, Q., Lan, X., 2012. The heavy mineral assemblages of the surface sediments on the northeast shelf of the East China Sea and their environmental implication. Haiyang Xuebao. 34(6): 114.

Wang, X., Baskaran, M., Su, K., Du, J., 2018. The important role of submarine groundwater discharge (SGD) to derive nutrient fluxes into River dominated Ocean Margins – The East China Sea. Marine Chemistry, 204: 121-132.

Wang, X. et al., 2021. Organic carbon production and nutrients consumption revealed by mixing model in the energetic Changjiang Estuary. Estuarine, Coastal and Shelf Science, 260: 107491.

Wang, Y., Ren, M.-e., Zhu, D., 1986. Sediment supply to the continental shelf by the major rivers of China. Journal of the Geological Society, 143(6): 935-944.

Wang, Z.-L., Liu, C.-Q., 2003. Distribution and partition behavior of heavy metals between dissolved and acid-soluble fractions along a salinity gradient in the Changjiang Estuary, eastern China. Chemical Geology, 202(3-4): 383-396.

Wang, Z.-L., Liu, C.-Q., 2008. Geochemistry of rare earth elements in the dissolved, acid-soluble and residual phases in surface waters of the Changjiang Estuary. Journal of Oceanography, 64(3): 407-416.

White, D.A. et al., 2019. Beryllium isotope signatures of ice shelves and sub-ice shelf circulation. Earth and Planetary Science Letters, 505: 86-95.

Willenbring, J.K., von Blanckenburg, F., 2010a. Long-term stability of global erosion rates and weathering during late-Cenozoic cooling. Nature, 465(7295): 211-4.

Willenbring, J.K., von Blanckenburg, F., 2010b. Meteoric cosmogenic Beryllium-10 adsorbed to river sediment and soil: Applications for Earth-surface dynamics. Earth-Science Reviews, 98(1-2): 105-122.

Wilson, D.J., Galy, A., Piotrowski, A.M., Banakar, V.K., 2015. Quaternary climate modulation of Pb isotopes in the deep Indian Ocean linked to the Himalayan chemical weathering. Earth and Planetary Science Letters, 424: 256-268.

Windom, H.L., Moore, W.S., Niencheski, L.F.H., Jahnke, R.A., 2006. Submarine groundwater discharge: A large, previously unrecognized source of dissolved iron to the South Atlantic Ocean. Marine Chemistry, 102(3-4): 252-266.

Wittmann, H., Oelze, M., Gaillardet, J., Garzanti, E., von Blanckenburg, F., 2020. A global rate of denudation from cosmogenic nuclides in the Earth's largest rivers. Earth-Science Reviews, 204: 103147.

Wittmann, H., Oelze, M., Roig, H., von Blanckenburg, F., 2018. Are seasonal variations in river-floodplain sediment exchange in the lower Amazon River basin resolvable through meteoric cosmogenic ^{10}Be to stable ^{9}Be ratios? Geomorphology, 322: 148-158.

Wittmann, H. et al., 2012. The dependence of meteoric ^{10}Be concentrations on particle size in Amazon River bed sediment and the extraction of reactive ^{10}Be/^{9}Be ratios. Chemical Geology, 318-319: 126-138.

Wittmann, H. et al., 2015. A test of the cosmogenic^{10}Be(meteoric)/^{9}Be proxy for simultaneously determining basin-wide erosion rates, denudation rates, and the degree of weathering in the Amazon basin. Journal of Geophysical Research: Earth Surface, 120(12): 2498-2528.

Wittmann, H., von Blanckenburg, F., Mohtadi, M., Christl, M., Bernhardt, A., 2017. The competition between coastal trace metal fluxes and oceanic mixing from the ^{10}Be/^{9}Be ratio: Implications for sedimentary records. Geophysical Research Letters, 44(16): 8443-8452.

Wu, J., Liu, J.T., Wang, X., 2012. Sediment trapping of turbidity maxima in the Changjiang Estuary. Marine Geology, 303-306: 14-25.

Xu, A., Hathorne, E., Laukert, G., Frank, M., 2023. Overlooked riverine contributions of dissolved neodymium and hafnium to the Amazon estuary and oceans. Nature Communication, 14(1): 4156.

Xu, J., Zhou, P., Lian, E., Wu, H., Liu, D., 2021. Spatial distribution of chlorophyll a and its relationships with environmental factors influenced by front in the Changjiang River Estuary and its adjacent waters in summer 2019. Marine Science Bulletin, 40: 541-549.

Xu, K., Milliman, J.D., 2009. Seasonal variations of sediment discharge from the Yangtze River before and after impoundment of the Three Gorges Dam. Geomorphology, 104(3-4): 276-283.

Xu, X., 1994. Geochemical studies of beryllium isotopes in marine and continental natural systems, University of Southern California, Los Angeles, 335 pp.

Yang, C., Vigier, N., Lian, E., Lai, Z., Yang, S., 2021. Decoupling of dissolved and particulate Li isotopes during estuarine processes. Geochemical Perspectives Letters: 40-44.

Yang, S.L. et al., 2005. Trends in annual discharge from the Yangtze River to the sea (1865–2004) / Tendances et épisodes extrêmes dans les débits annuels du Fleuve Yangtze débouchant dans la mer (1865–2004). Hydrological Sciences Journal, 50(5): 825-836.

Yang, S.L. et al., 2014. Downstream sedimentary and geomorphic impacts of the Three Gorges

Dam on the Yangtze River. Earth-Science Reviews, 138: 469-486.

Yang, Y.-L., Kusakabe, M., Southon, J.R., 2003. ^{10}Be profiles in the East China Sea and the Okinawa Trough. Deep Sea Research Part II: Topical Studies in Oceanography, 50(2): 339-351.

You, C.F., Lee, T., Li, Y.H., 1989. The partition of Be between soil and water. Chemical Geology, 77(2): 105-118.

Yousefi, S.R., Shemirani, F., Jamali, M.R., Salavati-Niasari, M., 2010. Extraction and preconcentration of ultra trace amounts of beryllium from aqueous samples by nanometer mesoporous silica functionalized by 2,4-dihydroxybenzaldehyde prior to ICP-OES determination. Microchimica Acta, 169(3-4): 241-248.

Zhang, Q., Liu, H., Qin, S., Yang, D., Liu, Z., 2014. The study on seasonal characteristics of water masses in the western East China Sea shelf area. Acta Oceanologica Sinica, 33(11): 64-74.

Zhang, S., Zhu, C., 2001. Soil loss and its effect on flooding catastrophe in Yangtze drainage basin. Journal of soil water conservation, 15(6): 9-13.

Zhang, Z. et al., 2020. Dissolved silicon isotope dynamics in large river estuaries. Geochimica et Cosmochimica Acta, 273: 367-382.

Zhao, S., Feng, C., Wang, D., Liu, Y., Shen, Z., 2013. Salinity increases the mobility of Cd, Cu, Mn, and Pb in the sediments of Yangtze Estuary: relative role of sediments' properties and metal speciation. Chemosphere, 91(7): 977-84.

Zhao, X. et al., 2022. Adsorptive removal of beryllium by Fe-modified activated carbon prepared from lotus leaf. Environmental Science and Pollution Research, 30(7): 18340-18353.

Zhou, Y. et al., 2016. Impacts of Three Gorges Reservoir on the sedimentation regimes in the downstream-linked two largest Chinese freshwater lakes. Scientific Report, 6: 35396.

Zhu, J., Zhu, Z., Lin, J., Wu, H., Zhang, J., 2016. Distribution of hypoxia and pycnocline off the Changjiang Estuary, China. Journal of Marine Systems, 154: 28-40.